

South Dakota State University
**Open PRAIRIE: Open Public Research Access Institutional
Repository and Information Exchange**

Theses and Dissertations


2016

Fully Solution Processed PEDOT:PSS and Silver Nanowire Semi-Transparent Electrodes for Thin Film Solar Cells

Bjorn Vaagensmith

South Dakota State University, bjorn.vaagensmith@jacks.sdstate.edu

Follow this and additional works at: <http://openprairie.sdstate.edu/etd>

 Part of the [Chemical Engineering Commons](#), [Electrical and Computer Engineering Commons](#), and the [Materials Science and Engineering Commons](#)

Recommended Citation

Vaagensmith, Bjorn, "Fully Solution Processed PEDOT:PSS and Silver Nanowire Semi-Transparent Electrodes for Thin Film Solar Cells" (2016). *Theses and Dissertations*. Paper 1069.

This Dissertation - Open Access is brought to you for free and open access by Open PRAIRIE: Open Public Research Access Institutional Repository and Information Exchange. It has been accepted for inclusion in Theses and Dissertations by an authorized administrator of Open PRAIRIE: Open Public Research Access Institutional Repository and Information Exchange. For more information, please contact michael.biondo@sdstate.edu.

FULLY SOLUTION PROCESSED PEDOT:PSS AND SILVER NANOWIRE SEMI-
TRANSPARENT ELECTRODES FOR THIN FILM SOLAR CELLS

BY

BJORN VAAGENSMITH

A dissertation submitted in partial fulfillment of the requirements for the

Doctor of Philosophy

Electrical Engineering

South Dakota State University

2016

FULLY SOLUTION PROCESSED PEDOT:PSS AND SILVER NANOWIRE SEMI-
TRANSPARENT ELECTRODES FOR THIN FILM SOLAR CELLS

This dissertation is approved as a creditable and independent investigation by a candidate for the Doctor of Philosophy in Electrical Engineering degree and is acceptable for meeting the dissertation requirements for this degree. Acceptance of this dissertation does not imply that the conclusions reached by the candidate are necessarily the conclusions of the major department.

Qiquan Qiao, Ph.D.
Dissertation Advisor

Date

Steven Hietpas, Ph.D.
Head, Electrical Engineering and Computer Science

Date

Dean, Graduate School

Date

ACKNOWLEDGEMENTS

I would like to thank my wife Amanda, who continues to show me how to become a better man and think more critically. You have always been supportive and encouraged me to work hard towards my doctorate, yet help pull me away for fun vacation adventures; adventures I look back on with more fondness and memory than countless hours spent in research. You inspire and encourage me, and have stuck with me through hard and pleasant times. I love you Amanda, you have deepened my grasp on life.

I would like to thank my family and friends for all their support. To Sam Yang, thank you for all the laughs and encouraging phone calls. A special thanks to Kenny Olson, Patrick Kuhn, and Jacob Clark for the visits or phone calls, and all my other friends who have stayed in touch over the years; your friendships mean a lot to me. To my parents, for all the encouragement to finish my degree and my sisters expressing how proud they are of me.

My advisors Dr. Qiao, Dr. Galipequ, Dr. Cross, and Dr. Zhu for your advice, direction, patients, time spent, and helpful ideas. Your dedication has meant a lot to me and I will always be grateful. A special thanks to Reza, Dr. Zhenping Zhou, Dr. Qi, Segun, Swami, Nirmal, Ashish, Lal, Abu, Hytham and all my other lab group members. Thank you for all the advice, helping hand you offered, laughs, and encouragement.

I would also like to thank NSF IGERT (grant DGE-0903685) scholarship program. Without the IGERT scholarship, a doctoral degree would have not been possible for me.

I would also like to acknowledge my Lord and savior Jesus Christ, who has seen me through all the difficult times and good times. His love has been a constant anchor in my life, and His word continues to inspire and teach me. I want to use all of my abilities to glorify His name and to his cause I dedicate my life's work.

TABLE OF CONTENTS

ABBREVIATIONS	x
LIST OF FIGURES	xiii
LIST OF TABLES	xiii
ABSTRACT.....	xxii
CHAPTER 1	1
1.1 INTRODUCTION.....	1
1.2 PREVIOUS WORK.....	9
1.3 MOTIVATION	24
1.4 OBJECTIVES	24
CHAPTER 2 THEORY.....	25
2.1 OPERATING PRINCIPLES OF SOLAR CELLS	25
2.2 EQUIVALENT CIRCUIT OF SOLAR CELLS	27
2.3 SINGLE JUNCTION SOLAR CELL PHYSICS.....	31
2.3.1 SILICON SOLAR CELLS	33
2.3.2 POLYMER SOLAR CELLS	36
2.3.3 PEROVSKITE SOLAR CELLS.....	38
2.4 SEMITRANSSPARENT SOLAR CELLS	39
2.4.1 BANDGAP AND LIGHT ABSORPTION	40
2.4.2 PEDOT:PSS TRANSPARENT ELECTRODES.....	40

2.4.3 SILVER NANOWIRE TRANSPARENT ELECTRODES.....	46
2.5 SPRAY COATING	49
2.6 SPIN COATING	50
2.7 ULTRAVIOLET-VISIBLE SPECTROMETER	51
2.8 FOUR-POINT PROBE	53
2.9 TRANSFER LENGTH METHOD	55
2.10 SCANNING PROBE MICROSCOPY	57
2.10.1 ATOMIC FORCE MICROSCOPY.....	58
2.10.2 CURENT SENSING ATOMIC FORCE MICROSOCOPY.....	61
2.11 SCANNING ELECTRON MICROSCOPE.....	61
2.12 ENERGY DISPERSIVE X-RAY SPECTROSCOPY.....	63
2.13 X-RAY DIFFRACTION SPECTROSCOPY	64
2.14 RAMAN SPECTRSCOPY	66
CHAPER 3 EXPERIMENTAL PROCEDURES	68
3.1 FABRICATION AND CHARACTERIZATION OF PEDOT:PSS TRANSPARENT ELECTRODES.....	68
3.1.1 GLASS SLIDE CLEANING AND PREPARATION.....	68
3.1.2 FABRICATION OF PEDOT:PSS TRANSPARENT ELECTRODES.....	69
3.1.3 THICKNESS MEASURMENTS OF PEDOT:PSS TRANSPARENT ELECTRODES	70

3.1.4 SHEET RESISTANCE OF PEDOT:PSS TRANSPARENT ELECTRODES	71
3.1.5 OPTICAL PHOTOGRAPHS OF PEDOT:PSS ELECTRODES	74
3.1.6 TOPOGRAPHY OF PEDOT:PSS TRANSPARENT ELECTRODES.....	74
3.1.7 CURRENT SENSING ATOMIC FORCE MICROSCOPY OF PEDOT:PSS ELECTRODES	76
3.1.8 TRANSMITTANCE OF PEDOT:PSS TRANSPARENT ELECTRODES	76
3.1.9 RAMAN SPECTROSCOPY OF PEDOT:PSS ELECTRODES.....	77
3.1.10 FABRICATION OF ITO FREE PEROVSKITE SOLAR CELLS	78
3.1.11 X-RAY DIFFRACTION SPECTROMETER OF PEDOT:PSS ELECTRODES	81
3.1.12 I-V CHARACTERIZATION OF PEROVSKITE SOLAR CELLS	82
3.1.13 TRANSIENT PHOTOCURRENT MEASUREMENT OF PEDOT:PSS ELECTRODES	84
3.2 SILVER NANOWIRE TRANSPARENT ELECTRODES FABRICATION AND CHARACTERIZATION	85
3.2.1 SILVER NANOWIRE SYNTHESIS AND SOLUTION PREPARATION	85
3.2.2 SILVER NANOWIRE TRANSPARENT ELECTRODE FABRICATION.....	87

3.2.3 MEASURING SILVER NANOWIRE ELECTRODE TRANSMITTANCE AND SHEET RESISTANCE	89
3.3 LIFETIME TEST AND CHARACTERIZATION OF SILVER NANOWIRE ELECTRODES	90
3.3.1 LIFETIME TEST MEASUREMENT OF SILVER NANOWIRE ELECTRODES	90
3.3.2 SCANNING ELECTRON MICROSCOPE, OPTICAL PHOTOGRAPHY, X-RAY DIFFRACTION SPECTROMETER, AND ENERGY DISPERSIVE X-RAY SPECTROSCOPY OF SILVER NANOWIRE ELECTRODES	91
CHAPER 4 RESULTS AND ANALYSIS	94
4.1 DEVELOPMENT OF PEDOT:PSS TRANSPARENT ELECTRODES	94
4.1.1 SOLVENT ADDITIVES TO PEDOT:PSS ELECTRODES	94
4.1.2 PEROVSKITE SOLAR CELL FABRICATION USING PEDOT:PSS ELECTRODES	106
4.2 SILVER NANOWIRE TRANSPARENT ELECTRODES LIFETIME UNDER ELECTRICAL STRESS.....	111
4.2.1 EFFECT OF UV-OZONE ON SILVER NANOWIRE ELECTRODES ...	111
4.2.2 ELECTRODE FAILURE UNDER ELECTRICAL STRESS.....	114
CHAPER 5 CONCLUSIONS.....	129
5.1 SUMMARY	129

5.2 CONCLUSIONS	132
5.3 FUTURE WORK	133
REFERENCES	138

ABBREVIATIONS

Ag	Silver
Al	Aluminum
AZO	Aluminum doped zinc oxide
BIPV	Building integrated photovoltaics
BJH	Bulk heterojunction
CSG	Crystalline silicon on glass
CVD	Chemical vapor deposition
\vec{E}	Electric field
E_g	Energy gap
ETL	Electron transport layer
<i>EQE</i>	External Quantum Efficiency
<i>FF</i>	Fill factor
HIT	Heterojunction with intrinsic thin layer
HOMO	Highest occupied molecular orbital
HTL	Hole transport layer
<i>I</i>	Current
I_D	Dark Current
I_m	Current of the maximum power point
I_{ph}	Photocurrent
<i>IQE</i>	Internal Quantum Efficiency
IR	Infrared
I_{sc}	Short Circuit Current

ITO	Indium tin oxide
J	Current density
k_B	Boltzmann's Constant ($8.617 \times 10^{-5} \text{ eV/K}$)
LUMO	Lowest unoccupied molecular orbital
OECD	Organization for Economic Co-operation and Development
OSC	Organic solar cell
PCE	Power conversion efficiency
PERL	Passive emitter, rear locally-diffused
p-i-n	Positive-intrinsic-negative (p-type - intrinsic - n-type)
P_m	Maximum power point
PV	Photovoltaics
PWh	Peta (10^{15}) Watt-hours
q	elementary charge ($1.6 \times 10^{-19} \text{ C}$)
R_s	Series resistance
R_{sh}	Shunt resistance
S	Siemens
SNW	Silver nanowires
UV	Ultraviolet
V	Voltage
V_m	Voltage of the maximum power point
V_{oc}	Open circuit voltage
ZnO	Zinc Oxide
η	Efficiency

μ	Mobility
σ	Conductivity

LIST OF FIGURES

Figure 1.1.	Global energy consumption for OECD and non-OECD affiliated countries from 1990 to 2010 and predicted energy consumption from 2020 to 2040 [5].....	2
Figure 1.2.	Global installed capacity of alternative energy sources and their predicted growth from 2020 to 2040.	4
Figure 2.1.	I-V curve of a solar cell with short circuit current (I_{sc}), open circuit voltage (V_{oc}), maximum power point (P_m), voltage at maximum power point (V_m), and current at maximum power point (I_m) labeled.	26
Figure 2.2.	Single diode model of a solar cell under (a) dark and (b) illuminated conditions.....	27
Figure 2.3.	Single diode model of a solar cell for illuminated case with series (R_s) and shunt (R_{sh}) resistance depicted.	30
Figure 2.4.	Effect of (a) decreasing R_{sh} and (b) increasing R_s have on the I-V curve.....	31
Figure 2.5.	Energy band diagram of (a) insulator, (b) semiconductor, and (c) conductor.	32
Figure 2.6.	(a) intrinsic silicon crystal lattice, (b) silicon crystal lattice doped with boron, and (c) silicon crystal lattice doped with phosphorus.....	34
Figure 2.7.	P-n junction (a) before and (b) and after the free charge carriers reach equilibrium.....	35
Figure 2.8.	Light absorbed into a solar cell frees an electron-hole pair, which is used to power a lightbulb.....	36

Figure 2.9.	HJB structure for (a) regular and (b) inverted polymer solar cells.	38
Figure 2.10.	Perovskite crystal structure.	39
Figure 2.11.	PEDOT in its natural (a)(b) and oxidized (c)(d) form and benzoid (a)(c) and quinoid (b)(d) structures.	42
Figure 2.12.	(a) Doped PEDOT with positive charge coulombically bound to (b) PSS species.	43
Figure 2.13.	(a) ladder type structure and (b) scrambled egg type structure for a polycation and polyanion blend.	45
Figure 2.14.	Operating principles of silver nanowire electrodes.	47
Figure 2.15.	Setup of a gravity fed Spray coater with gas pressure to aerosolize solution and direct spray.	50
Figure 2.16.	Spin coating setup.	51
Figure 2.17.	Schematic of an ultraviolet-visible spectrometer.	53
Figure 2.18.	(a) Four-point probe set up and (b) electrical model for four-point probe setup.	54
Figure 2.19.	(a) Experimental setup for the transfer length method and (b) distance vs resistance plot used to calculate R_{\square}	56
Figure 2.20.	Modified version of the transfer length method where all the electrodes are evenly spaced apart.	57
Figure 2.21.	Experimental setup for scanning probe microscopy.	58
Figure 2.22.	Force distance curve for atomic force microscopy.	59
Figure 2.23.	Scanning electron microscope operating principles.	63

Figure 2.24.	(a) Ejection of a core shell electron due to collision with a high energy electron beam and (b) emission of X-ray due to outer shell electron relaxing to the core shell.	64
Figure 2.25.	Working principle of X-Ray diffraction spectroscopy.	65
Figure 2.26.	Vibrational modes for a water molecule.....	66
Figure 3.1.	Photograph of plasma cleaning set up with a BOC Edwards XDS5 vacuum pump on the right and a PDC-32G plasma cleaner on the left....	69
Figure 3.2.	Photograph of spin coater.	70
Figure 3.3.	Photograph of Veeco Dektak 150 used to measure film thickness.....	71
Figure 3.4.	Photographs of (a) mask using during the silver contact deposition and a sample with silver contacts and (b) the thermal evaporation system inside the glove used to deposit the silver contacts.	72
Figure 3.5.	Photograph of Keithley 2400 used to measure the resistance between the electrodes with an inset of a sample to be measurement.	73
Figure 3.6.	Photograph of Hitachi S-3400N system used for SEM imaging and EDX measurements.	74
Figure 3.7.	Photograph of Agilent 5500 scanning probe microscope (SPM) used to take topography and current sensing AFM (CS-AFM) images.....	75
Figure 3.8.	Photograph of Agilent 8353 UV-Visible spectrophotometer for transmission spectroscopy.	77
Figure 3.9.	Photograph of LabRam HR800 system used for Raman spectroscopy.	78
Figure 3.10.	Device structure of the perovskite solar cell.....	80
Figure 3.11.	Etching PEDOT:PSS with cotton applicator.	80

Figure 3.12.	Photograph of spin coater used inside grove box to deposit perovskite, PC ₆₀ BM, and Rhodamine films.....	81
Figure 3.13.	Photograph of Rigaku Smartlab system used to obtain X-Ray Diffraction (XRD) spectrum.	82
Figure 3.14.	Photograph of experimental set up using (a) Agilent 4155C semiconductor parameter analyzer and (b) Xenon arc lamp (Newport 67005) for I-V characterization.	83
Figure 3.15.	Photograph of Newport 69911 power supply used to power the Xenon Arc lamp.....	83
Figure 3.16.	Photograph of experimental setup for transient photocurrent measurement.	84
Figure 3.17.	Photograph of dry run setup for silver nanowire synthesis.....	86
Figure 3.18.	Photograph of Eppendorf Centrifuge 5424 used to clean silver nanowires.	87
Figure 3.19.	Photograph of (a) Mater airbrush G255-SET and (b) unbranded airbrush with 7cc fluid cup used to spray coat spray silver nanowires.....	88
Figure 3.20.	Photograph of nitrogen gas cylinder used to supply gas pressure to the airbrush with inset of the three-way valve nipple where the hose for the spray coater was connected.	88
Figure 3.21.	Photograph of Guardian SRM - 232 - 100 used to measure sheet resistance with an inset of the probes.	89

Figure 3.22.	Photograph of experimental set up for measuring the lifetime of silver nanowire electrodes under electrical stress with inset of 3M clips clamping a sample (upper left) and a silver nanowire electrode with silver contacts (lower right).	91
Figure 3.23.	Photograph of Plasma Sciences Inc. CrC-150 Sputtering System used to deposit gold.	93
Figure 4.1.	Comparison of sheet resistance for PEDOT:PSS with various solvent additives.	95
Figure 4.2.	Time lapsed photos of the slow drying process for PEDOT:PSS film with 15 wt. % 1:1 DMSO:EG additive.	96
Figure 4.3.	Sheet resistance for PEDOT:PSS films soaked in various solvents and solvent blends.	97
Figure 4.4.	Topography images of (a) pristine PEDOT:PSS and PEDOT:PSS with (b) 10 % wt. EG, (c) 15 % wt. DMSO, (d) 15 % wt. 1:1 DMSO:EG additives, and (e) 15 % wt. 1:1 DMSO:EG after being soaked in water:EG:ethanol (1:1:1).	98
Figure 4.5.	(a) Topography, (b) current-sensing atomic force microscopy performed at 0.1 V bias for PEDOT:PSS films with 10 wt. % EG, and (c) line scan from images (a) and (b) (indicated by white line).	100
Figure 4.6.	(a) Topography and (b) current-sensing atomic force microscopy performed at 0.3 V bias pristine PEDOT:PSS films.	101

Figure 4.7.	(a) Topography of PEDOT:PSS film with 15 wt. % DMSO:EG (1:1) additive and corresponding CS-AFM images under 0.1 Volt bias after (a) first, (c) second, and (d) third consecutive scans.....	102
Figure 4.8.	Ultraviolet-visible absorbance spectra of PEDOT:PSS films (a) with various EG wt. % additives and with 15 wt. % 1:1 EG:DMSO before and after post treatment and (b) with various wt. % DMSO additives. ..	103
Figure 4.9.	Raman spectra for PEDOT:PSS films for increasing % wt. of (a) EG and (b) DMSO and 1:1 DMSO:EG additive.....	104
Figure 4.10.	Morphology illustration of PEDOT:PSS for (a) pristine, (b) 10 wt. % ethylene glycol (EG), (c) 15 wt. % DMSO, (d) 15 wt. % DMSO:EG 1:1, and (e) 15 wt. % DMSO:EG 1:1 additive after post treatments.....	106
Figure 4.11.	(a) XRD spectra of perovskite on top of a four layer PEDOT:PSS electrode and ITO electrode and topography images of perovskite on top of (b) ITO and (c) PEDOT:PSS electrodes.....	108
Figure 4.12.	(a) Perovskite device structure and (b) I-V curves for perovskite solar cells.	109
Figure 4.13.	Transient photocurrent for perovskite solar cells made with 4 layers of PEDOT:PSS electrodes and ITO electrodes.....	110
Figure 4.14.	Dependence of sheet resistance and transmittance at 550 nm on annealing temperature with 30 minutes annealing time (highlighted data) and 10 minutes annealing time (no highlight).	112

Figure 4.15.	EDX spectrum for silver nanowire electrodes (a) before and (b) after 1 minute of UV-ozone treatment with SEM image inset of the measurement location.	113
Figure 4.16.	Distribution of silver nanowire (a) diameter and (b) length.	115
Figure 4.17.	SEM images of silver nanowire, with zoomed inset, synthesized at (a) 150 °C and (b) 160 °C.	115
Figure 4.18.	Dependence of silver nanowire formation time on synthesis temperature. The inset is a SEM image of silver nanowire synthesized at 140 °C.....	117
Figure 4.19.	Voltage verse time plot for silver nanowire electrodes with different synthesis temperatrues and nanowire diameters subject to 20 mA/cm ² of constant current density.	120
Figure 4.20.	Photographs of silver nanowire electrodes with 233 nm average nanowire diameters after (a) freshly sprayed, (b) 5 month of air exposure, (c) 5 month of air exposure after failed from electrical, (d) failed from electrical stress, and Silver nanowire electrodes with 80 nm average nanowire diameter (e) after failure and 15 months' exposure to air and (f) 15 months' exposure to air.	121
Figure 4.21.	EDS spectrum of silver nanowire electrode with thicker nanowire diameters with SEM image inset of measurement location after (a) failure from electrical stress and (b) left in air for 9 months.....	122
Figure 4.22.	(a) XRD spectra of silver nanowires with average diameters of 233 nm (b) zoomed in portion of (a).....	124

Figure 4.23.	SEM images of failed silver nanowire electrodes with average diameters of (a) (b) 80 nm and (c) (d) 223 nm, where (a) and (c) are representative of the entire sample and (b) and (d) depict broken nanowires.	126
Figure 4.24.	Voltage vs time of silver nanowire electrodes subject to 20 mA of constant current.	127
Figure A.1.	Front Panel display from lab view program used for lifetime measurements on silver nanowire electrodes, where Source Level 1 and 2 are set to 0.02 A and the maximum limit is 10 volts.....	134
Figure A.2.	Block diagram corresponding the Front Panel in Figure A.76.	135
Figure B.1.	Raman spectrum of PEDOT:PSS films with various % wt. of EG:DMSO 1:1, 1:2, and 2:1 v/v ratios	136
Figure C.1.	Silver nanowires synthesized at 160 C after (a) 10, (b) 15, and (c) 20 minutes of reaction time with average nanowire diameter of 60 nm, 312 nm, and 350 nm, respectively.	137

LIST OF TABLES

Table 4.1.	Device parameters for perovskite solar cells made using PEDOT:PSS and ITO as transparent electrode.....	109
Table 4.2.	Dependance of sheet resistance on UV-ozone treatment time on silver nanowire electrodes.....	112
Table 4.3.	Wt.% of elements detected from silver nanowire electrodes before and after 1 minute UV-ozone treatment.....	114
Table 4.4.	Relationship between silver nanowire average diameter, synthesis temperature, synthesis temperature, UV- treatment condition, electrode annealing temperature, and the resulting sheet resistance.....	118
Table 4.5.	Wt.% of elements detected from Figure 4.19 (a) and (b).....	122

ABSTRACT

FULLY SOLUTION PROCESSED PEDOT:PSS AND SILVER NANOWIRE SEMI-
TRANSPARENT ELECTRODES FOR THIN FILM SOLAR CELLS

BJORN VAAGENSMITH

2016

Building integrated photovoltaics (BIPV), such as semitransparent organic solar cells (OSC) for power generating windows, is a promising method for implementing renewable energy under the looming threat of depleting fossil fuels. OSC require a solution processed transparent electrode to be cost effective; but typically employ a non-solution processed indium tin oxide (ITO) transparent electrode. PEDOT:PSS and silver nanowire transparent electrodes have emerged as a promising alternative to ITO and are solution processed compatible. However, PEDOT:PSS requires a strong acid treatment, which is incompatible with high throughput solution processed fabrication techniques. Silver nanowires suffer from a short lifetime when subject to electrical stress. The goals of this work were to fabricate a PEDOT:PSS electrodes without using strong acids, a silver nanowire electrode with a lifetime that can exceed 6000 hours of constant electrical stress, and use these two electrodes to fabricate a semitransparent OSC. Exploring optimal solvent blend additives in conjunction with solvent bend post treatments for PEDOT:PSS electrodes could provide an acid free method that results in comparable sheet resistance and transmittance of ITO electrodes. Silver nanowires fail under electrical stress due to sulfur corrosion and Joule heating (which melts and breaks apart electrical contact). A silver oxide layer coating the nanowires could hinder sulfur corrosion and help redistribute heat. Moreover, nanowires with thicker diameters could

also exhibit higher heat tolerance and take longer to corrode. Four layer PEDOT:PSS electrodes with optimal solvent blend additives and post treatments were fabricated by spin coating. Silver nanowire electrodes of varying nanowire diameter with and without UV-ozone treatment were fabricated by spray coating and subject to electrical stress of 20 mA/cm^2 constant current density. PEDOT:PSS electrodes exhibited a sheet resistance of $80 \text{ } \Omega/\square$ and average transmittance of 73%, which were too high and too low, respectively. Silver nanowire electrodes, on the other hand, were able to achieve sheet resistances below $50 \text{ } \Omega/\square$ while maintaining a direct transmittance above 80%. Silver nanowires electrodes with average nanowire diameters of 80 nm lasted 2 days longer with UV-ozone treatment than without; and silver nanowire electrodes with average nanowire diameters of 233 nm lasted for 6,312 hours, which met the 6000 hour goal. PEDOT:PSS transparent electrode needs to be improved where the sheet resistance is below $50 \text{ } \Omega/\square$ and transmittance above 80%. This could be achieved by adding silver nanoparticles (SNP) less than 40 nm in size, which would also have a plasmonic effect enabling the solar cell to absorb ultraviolet light. Then a fully solution processed semitransparent solar cell utilizing a PEDOT:PSS:SNP and silver nanowire transparent electrodes can be fabricated.

CHAPTER 1

1.1 INTRODUCTION

The standard of living achieved by society has been undeniably linked to its energy consumption [1-3]. Alam et al. describes some of the variables associated with societies standard of living such as: infant mortality rate, life expectancy, food consumption, and percent of literate persons [1]. In developed countries such as the United States, energy consumption is high, and none of the aforementioned variables are of relative high concern in comparison to countries with low energy consumption. In light of this, energy consumption is of paramount importance for a good sustainable quality of life where basic human needs for all persons can be met. The great question facing engineers today is, “where will this energy come from?”

The question, “where will this energy come from” only becomes bigger when considering 17% and 32% of countries in the world are rated low and medium, respectively, according to the human development index scale [4]. The amount of energy expenditure needed to improve a society standard of living is much greater than the energy needed to sustain the improved standard of living [2]. This is because the social-economic environment takes time to adjust and reach an equilibrium related to the energy consumption. In a country whose food supply relies on farmers with only hand tools that consume no energy, the farmers will have to work long hours for a small amount of crop output. Depending on the population, many people may go hungry. Now with the assistance of tractors and other energy consuming tools given to the farmers, the modern farming tools will require much more energy expenditure in comparison to hand tools but they enable farmers to produce far more food than before. Despite this, the economic

status of the country may not be ready to support additional food. With time the economy may support the additional food, make hunger a less common issue, and develop more energy efficient uses of modern farm equipment. When considering the global energy need, it is important to be able to predict where more energy will be needed as societies seek to improve their standards of living.

The world's human population continues to grow and has now surpassed 7 billion. As underdeveloped countries seek to improve their standards of living, it becomes obvious that current energy sources must be reevaluated to ensure future energy security. Figure 1.1 shows global energy consumption for OECD (organization for economic co-operation and development) and non-OECD affiliated countries from 1990 to 2010 and predicted energy consumption from 2020 to 2040 [5]. From 2010 to 2040 it is expected that the demand for energy will increase by 56%.

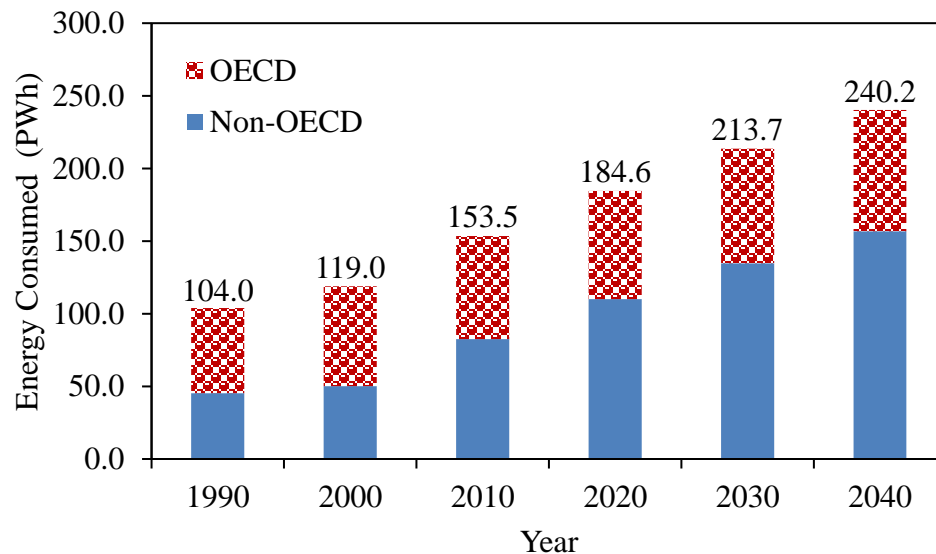


Figure 1.1. Global energy consumption for OECD and non-OECD affiliated countries from 1990 to 2010 and predicted energy consumption from 2020 to 2040 [5].

Fossil fuels are the main energy sources used to meet global energy demands. In 2013 the United States Energy Information Administration estimated that 80% of the global energy needs were supplied by fossil fuels [5], which represents a 5% decline from 2010 [6]. Fossil fuels are mainly composed of oil, natural gas, and coal. According to 2015 BP statistical review, the oil, natural gas, and coal reserves will last for only 52.5 years, 54.1 years, and 110 years, respectively [7]. In contrast, the change in the number of years left from BP's 2012 predictions indicate natural gas and coal reserves are being depleted faster than expected. Considering that 49% of the world's populations will need a large amount of energy to improve their standard of living and continued growth of the human population, it becomes obvious that fossil fuels cannot provide a secure energy future.

Our fossil fuel supply will vanish quickly if an effective alternative energy source is not found to ween the world off its fossil fuel dependence. There are several different energy sources in competition for this roll: wind turbines, hydroelectric power, nuclear energy, and solar energy. Figure 1.2 shows the global installed capacity of alternative energy sources and their predicted growth from 2020 to 2040 put out by the United States Energy Information Administration [5].

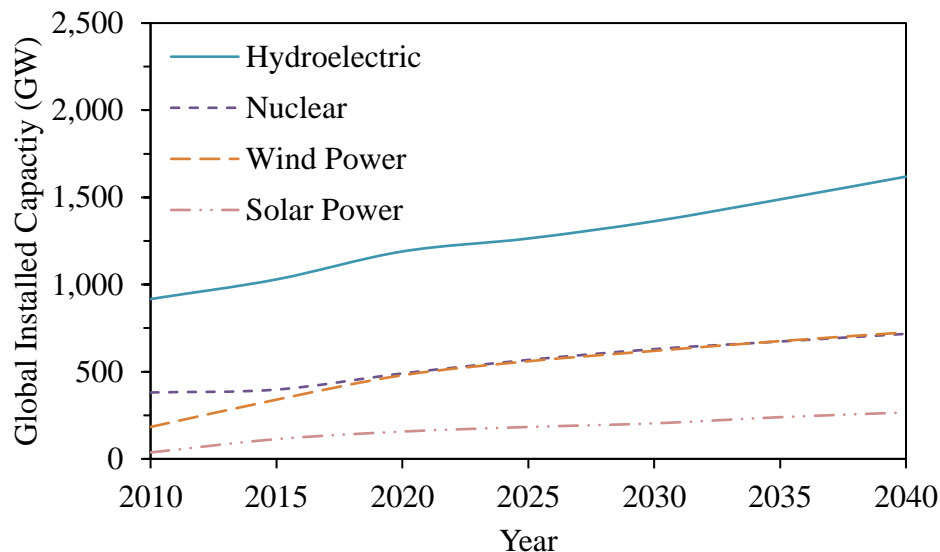


Figure 1.2. Global installed capacity of alternative energy sources and their predicted growth from 2020 to 2040.

Hydroelectric has by far the highest installed global capacity with wind and nuclear tied for second place and solar energy last. Hydroelectric energy is by far the oldest and most developed form of electrical energy generation of these technologies. Although wind energy is much older than nuclear technology, it is now finally starting to catch up in terms of energy generation. Solar technology is the youngest of all these alternative forms first demonstrated by Bell Labs in 1954. All of these technologies may have a critical part to play in weaning the world off its fossil fuel dependence.

Hydroelectric power utilizes the flow of naturally running water, and thus has no fuel cost. The major disadvantage of hydroelectric power is its dependence on where flowing water occurs. The Hoover Dam is one of the largest dams in the world and supplies power to Nevada, Arizona and California. It would not be reasonable to assume the Hoover Dam could supply power to New York due to significant energy loss associated with long distance traveled over power lines. Moreover, building dams has a

great impact on the ecological systems in the surrounding areas [8]. There are great efforts underway to better understand the damaging effects dams have on the animal and plant life. Although hydroelectric power has a role to play in meeting the future energy needs, it is not the ultimate answer in the quest for ubiquitous energy.

Wind energy has risen in popularity and continues to be a big player in renewable energy sources. Wind can be found nearly anywhere on the earth, but harvesting it is not always practical. Specific sites with excellent wind resources play a larger role in generating cost effective energy than advanced turbine technology [9]. In the United States, most of the wind resources available are located from North Dakota to Texas and on the coasts [10]. Other areas would require long transmission lines to deliver power. The total onshore energy potential for wind energy has been estimated to be 20 - 50 petawatt-hours (PWh) [11], which is higher than the global electrical energy consumption for 2010 (2.0 PWh) [5], but far below 2010's world energy consumption (153.5 PWh). As the use of fossil fuels (about 80% of the world energy needs) declines, many technologies such as cars will likely migrate to using electricity as an alternative power source; resulting in a dramatic increase in electrical power demand. In addition, concerns about killing wildlife, noise pollution, and turbines become an eyesore have all been raised against wind energy [12]. Although wind energy may be practical in the Midwest of the United States and well positioned countries such as Denmark, it does not seem to be a good solution to take care of all the worlds' energy demands.

Nuclear energy has received the strongest opposition to all energy sources but can produce a dependable constant output of energy with very little fuel. Nuclear energy has the potential to provide for all global energy needs. Many countries are discontinuing

their nuclear programs due to serious safety and environmental concerns [7]. Joseph Shuster in his book "*Beyond Fossil Fools*" makes a strong argument for nuclear technology and a detailed plan to remove the world from its fossil fuel dependence [13]. He argues that nuclear energy is currently the only non-fossil fuel based source that has the ability to meet global energy demands, and strongly urges governments to build more light water reactors. He admits that radioactive waste with the light water reactors is a significant problem but proposes the use of fast fusion reactors, which can reuse the waste from the light water reactors. After the radioactive waste is used for fuel in the fast fusion reactors the length of its radioactive toxicity drops from +10,000 years to 500 years and reduces the waste size by 95%. With great reductions in the size of nuclear waste and the length of its toxicity make current storage plans much more feasible. However, Shuster admits on page 183 that fast fusion reactor technology is not yet ready.

Shuster blames politics, media and ignorance for the slow progress of nuclear energy and calls for a fast reform. Current reports on fast fusion reactors reveal that the technology is still under development due to safety concerns and high operation cost [14, 15]. Furthermore, the 2011 nuclear reactor accident in Japan has brought great alarm to safety concerns [16]. Japan completely shut down its nuclear program in 2014. Shuster admits that the public opinion is mostly against nuclear energy. Although nuclear energy has the potential to supply the world's energy needs, the negative sentiment towards this technology has crippled its development. It is not likely that the world will look with approval on nuclear energy in the near future and the consequences of a failed reactor can be devastating. History shows if society is not ready to accept a technology, they won't-even if it is revolutionary [17]. Until the dangers with nuclear energy can be worked out

and trust with public perception can be built up again, nuclear energy does not have a bright future. Although Shuster advocates nuclear energy for today, he admits solar power will likely become the dominant energy source after it has had more time to mature.

Every year the sun irradiates a total of 8.33×10^5 PWh on the earth, which is several orders of magnitude higher than the predicted global energy needs for 2040. Sunlight can be found anywhere on the earth and solar power plants can be built faster and easier than hydro, wind, or nuclear power plants. In addition, solar panels have the flexibility to be integrated into builds to generate power where it is needed. Many corporate giants such as Walmart and Apple have already begun integrating photovoltaic (PV) panels onto the rooftop of their stores [18] [19]. Another example of building integrated photovoltaics (BIPV) is 4 Times Square [20]. A building in 4 Times Square integrates the PV on the south side of the building and can generate 13.8 MWh/year. BIPV makes effective use of unused space, emits no carbon emission, and has no negative impact on the environment.

The obvious drawback of solar energy is that no power is produced when the sun does not shine. This can be offset by the use of battery storage systems. The addition of battery storage can dramatically increase the cost of the system. However, continued research and efforts in photovoltaics have resulted in a dramatic decrease in system cost. In today's US currency, the cost of a PV system was estimated at \$500/watt in 1977 and has dropped to less than \$1/watt in 2015 [21]. Future research and improvement are needed to make it more cost competitive with fossil fuels. BIPV can cut down the cost of PV systems because they use the buildings as a support instead of racking systems.

Power generating windows are good examples of BIPV that does not need a racking system. A semi-transparent solar cell is simply integrated into the windows of a building. This additional functionality in windows can make use of energy that would have normally been wasted. Glass used in commercial applications typically reflect all ultraviolet (UV) (200 - 400 nm) and infrared (IR) (780 - 2500 nm) light and ranged from 19 – 79% transparent for light in the visible region (400 - 780 nm) [22, 23]. The UV, IR, and visible portions of the solar spectrum account for 9.3%, 38.8%, and 51.9% of the total energy [24]. Power generating windows could harness the 48.1% of solar energy that would have otherwise been reflected back into the environment.

The first attempts at window solar cells used silicon. Silicon is not a transparent material but was made so by drilling small holes within PV cells. The transmittance and efficiency of these devices was 10 - 20% and 6 - 12%, respectively [25-27]. Other designs attempted to fabricate micro cells that could be spaced apart on a transparent substrate, allowing light to pass through the spaces between them [28, 29]. However, these micro cell studies never reported on the efficiency and transmittance of their semi-transparent PV panels. From the work that has been done, it is evident that silicon based solar cells are limited in their applications as power generating windows due to their low transmittance.

Organic solar cells (OSCs), on the other hand, are able to exhibit high transmittance, which can be used in a wider range of window applications [30-32]. This is because OSCs are able to be tuned to absorb different portions of the solar spectrum. Mulligan et al. studied OSC economics and indicated that they are now cost competitive with silicon solar cells [33]. Although efficiency and device lifetime for OSCs are lower

than their silicon counterparts, OSC fabrication is significantly cheaper. The flexibility in transmittance and low cost fabrication methods make OSCs a better candidate for power generating window applications.

The low cost fabrication of OSCs is dependent on the use of solution processing techniques. Silicon solar cells are fabricated using high temperature methods and costly vacuum deposition techniques which results in an overall PV panel that is rigid and heavy. Solution processed OSCs can use roll-to-roll printing methods leading to mechanically flexible and lightweight panels. The study by Mulligan et al. assumes that all layers of the OSCs are solution processed, which is not always the case. Many OSCs make use of vacuum deposited top and bottom electrodes, and, assuming this is the case, Azzopardi et al. found that OSCs would not be cost effective [34]. Nearly all reports on OSC rely on vacuum deposition technology to deposit indium tin oxide (ITO) as the transparent electrode (typically the bottom electrode). OSCs for power generating windows will need a solution processed alternative to ITO for both the top and bottom electrodes to be cost effective competitive.

1.2 PREVIOUS WORK

The first solar cell was invented at Bell Labs by Chapin et al. and achieved 6% power conversion efficiency (PCE) in 1954 [35]. The efficiency was later improved to 15.5% by Lindmayer and Allison in 1973 [36]. They added a tantalum oxide layer on top of a silicon solar cell, which was able to prevent blue and violet light from radiating out of the device. The trapped blue and violet light had a better chance of being absorbed by the silicon to generate electricity. The 20% efficiency barrier was broken by Blakers et al. in 1986 [37]. They were able to reduce reflection loss to 0.2% by texturing the top

surface of a passive emitter silicon solar cell structure. Zhao et al. achieved a PCE of 24% using a crystalline silicon passivated emitter, rear locally-diffused (PERL) structure in 1996 [38]. They enhanced light absorption by incorporating an inverted pyramid structure on the top of the PERL device. They later improved the PERL efficiency to 24.7% by using float zone silicon substrates in 1999 [39]. The world record single junction silicon solar cell achieved by Panasonic Corporation in 2014 was 25.6% [40]. Panasonic researchers developed the heterojunction with an intrinsic thin layer (HIT) silicon solar cell device structure. The HIT structure differed from other silicon solar cells in that it incorporates both crystalline and amorphous silicon, which Panasonic claims reducing recombination losses within the device. By applying a patterned back contact, Panasonic improved the efficiency of HIT solar cells. These solar cell devices fall into the first generation photovoltaic devices.

The second generation solar cells attempted to reduce the cost of the first generation by reducing device thickness to be on the order of 1 μm . By using less material, the second generation solar cells were cheaper but sacrificed device efficiency. The first thin film solar cell was reported by Carlson et al. in 1976 [41]. Carlson employed amorphous silicon in a p-i-n device structure and achieved 2.4% efficiency. Torres et al. reported a microcrystalline silicon thin film solar cell with PCE of 7.7% in 1996 [42]. Keevers et al. demonstrated the highest reported thin film silicon solar cell device with PCE of 10% in 2007 [43]. They used crystalline silicon on glass (CSG) device structure and a new abrasive-etch treatment to texture the glass substrate and finished the device with an anti-reflection layer on top.

Third generation solar cell technology seeks to further reduce the cost of solar cell fabrication using solution processed technology to replace vacuum deposition methods such as chemical vapor deposition (CVD). Solution processed solar cells could be fabricated through printing techniques such as inkjet or roll-to-roll, allowing for fast continuous output of light weight and flexible PV modules. Typically, the third generation PV technology refers to organic solar cells such as dye sensitized, perovskite and polymer solar cells. Although attempts to create a fast continuous output fabrication of inorganic solar cells have been made [44], they typically result in low efficiencies and require vacuum deposition[45].

The first OSC was demonstrated by Kearns et al. in 1958 [46]. Kearns produced a photovoltage of 200 mV using tetramethyl p-phenylenediamine coated on a Magnesium phthalocyanine disk. A OSC made by merocyanine 5 dye between Al and Ag electrodes exhibited 0.7% efficiency was reported by Morel et al. in 1978 [47]. A bi-layer solar cell utilizing a donor and acceptor material stacked on top of one another was reported by Tang et al. in 1986 [48]. The bi-layer device exhibited 0.95% efficiency under illumination of 75 mW/cm^2 . The concept of a bulk heterojunction was reported by Sariciftci et al. in 1992 [49]. The bulk heterojunction was made by blending a conjugated polymer (donor) with a fullerene (acceptor) between two electrodes. The bulk heterojunction was first reported in OSC by Yu et al. in 1995 [50]. Using the same system reported by Sariciftci et al., Yu et al. fabricated an OSC with a PCE of 2.9%. A 4.4% efficient bulk heterojunction OSC was reported by Li et al. in 2005 [51]. Li et al. used a slow drying method to allow the donor (poly(3-hexylthiophene)) and acceptor ([6,6]-phenyl-C61-butyric acid methyl ester) to arrange themselves in a more optimal

morphology. The highest OSC efficiency of 11.2% was reported by Zhao et al. in 2016 [52]. Zhao et al. used a fullerene free bulk heterojunction solar cell with PBDB-T (poly[(2,6-(4,8-bis(5-(2-ethylhexyl)thiophen-2-yl)benzo[1,2-b:4,5-b']dithiophene))-alt-(5,5-(1',3'-di-2-thienyl-5',7'bis(2-ethylhexyl)benzo[1',2'-c:4',5'-c']dithiophene-4,8-dione))] as the donor and ITIC (3,9-bis(2-methylene(3-(1,1-dicyanomethylene)-indanone))-5,5,11,11-tetrakis(4hexylphenyl)-dithieno[2,3-d:2',3'-d']-s-indaceno[1,2-b:5,6-b'] dithiophene) as the acceptor. The PBDB-T:ITIC device outperformed the PCE for the PBDB-T:fullerene acceptor device by 3.8%. Zhao et al. also demonstrated that the PBDB-T:ITIC was thermally stable, could withstand temperatures of 200 °C and maintained efficiency's greater than 10%. The fullerene-based counterparts, which lost over 50% of their original PCE when exposed to the same heat. The record PCE for polymer solar cells shows great promise for the future of OPV and strongly suggests they may soon become cost competitive to fossil fuels [33, 34].

Perovskite solar cells are also a third generation solar cell technology that utilizes organic compounds but have earned a right to their own category due to significant advancements. The first perovskite solar cell achieved 3.8% PCE and was reported by Kojima et al. in 2009 [53]. Kojima et al. employed a single step method by spin coating a precursor solution to form the $\text{CH}_3\text{NH}_3\text{PbI}_3$ -based perovskite solar cell which had good light absorption but poor device stability. Four years later a perovskite solar cell with 15% PCE was reported by Burschka et al. [54]. Burschka et al. employed a two-step method by first depositing a PbI_2 solution then soaking the PbI_2 film in a $\text{CH}_3\text{NH}_3\text{I}$ solution, which resulted in formation of the $\text{CH}_3\text{NH}_3\text{PbI}_3$ perovskite film. Perovskite solar cells with a PCE of 18% were reported by Nie et al. in 2015 [55]. They used a

single step hot casting technique where a perovskite precursor solution (PbI_2 mixed with methylamine hydrochloride) is heated to temperatures as high as 180°C and spin coated onto a substrate heated to the same temperature. The perovskite films were highly crystalline with grain sizes as large as $1\ \mu\text{m}$ and exhibited improved charge transport. The perovskite PCE was then improved to 20% by Yang et al. in 2015 [56]. Yang et al. used FAPbI_3 instead of MAPbI_3 as a perovskite layer because it has a broader light absorption. Successful deposition of FAPbI_3 is difficult, but Yang et al. employed an intramolecular exchange process, which enabled the formation of high quality and thick ($500\ \text{nm}$) FAPbI_3 films. The highest reported efficiency for perovskite solar cells was announced by the national renewable energy laboratory (NREL) to be 22.1% in 2016 [57].

Since 2009 perovskite solar cells have made remarkable progress from 3.8% PCE to 20% in 2015, however all these perovskite solar cells use lead – a water soluble toxin. Moreover, the stability of these devices is on the order of months [58]. Lead free perovskite solar devices have been explored but these attempts resulted in even worse stability and low PCE [59]. The heavy dependence on toxic materials and low stability of perovskite solar cell devices dampen the prospect of becoming a commercially viable energy solution.

With the advent of 2nd and 3rd generation photovoltaic devices, semi-transparent solar cells for power generating windows began to be explored. Early attempts that fabricated semi-transparent solar cells for power generating window used silicon. One of the first reports was in 1990 by Ohnishi et al. who attempted to use a laser patterning method to create microscopy holes in an amorphous silicon solar cell [60]. Ohnishi et al.

reported a 5.0% PCE with 15% transmittance. They found that using the laser patterning method resulted in little effect to the devices' fill factor and that theoretical transmittances up to 60% were possible. The drawback was that the transmittance of the device had a reddish color due to the nature of the amorphous silicon and that a transmittance of 15% was very low.

Takeoka et al. used a chemical etch method to create pin holes in an amorphous silicon solar cell and achieved a transmittance of 10% and a PCE of 4.6% [26]. They used photolithography with no photoresist developer to create a hexagonal pattern to be etched into the silicon solar cell. Simulations showed this method could allow for transmittances up to 50%, although the highest transmittance reported here was 30% with 3.6% PCE. The drawback of this work is the low PCE in comparison with the transmittances. These devices are limited to security window applications (or sun roofs in a car as suggested by Takeoka et al.).

Kuhn et al. reported a transparent solar cell with 10.4% PCE and a transmittance of 18% [27]. Kuhn et al. used a mechanical dicing saw to cut grooves into a silicon wafer running vertically on one side and horizontally on the other. The locations where the cuts interacted formed small holes in the silicon wafer making it semi-transparent. These wafers were then fabricated into a monofacial silicon solar cell. The main drawback of this work is the low transmittance and the authors did not discuss how increased device transmittance would affect its PCE.

A semi-transparent silicon solar module was fabricated by arranging small silicon solar cells in the shape of spears on a plastic substrate by Biancardo et al. in 2007 [29]. The spheres were fabricated by dicing p-type silicon wafer into small cubes, which were

sequentially rounded into spheres via mechanical grinding. The spheres were oxidized followed by the formation of a n-type layer through phosphorous diffusion. Silver and aluminum were used as top and bottom electrodes, respectively. The spheres had a diameter of 1.8 μm and were able to absorb light equally from any angle unlike a conventional planar solar cell. These spherical cells exhibited efficiencies of 23.5% with a reflective mirror behind them and 13.5% without a mirror. To fabricate a transparent solar cell module, the spheres were spaced apart inside a silicon matrix. However, the efficiency and its relationship to transmittance of these modules was not reported.

Denizot et al. reported a semi-transparent silicon solar cell to be used as a window shade in 2009 [25]. The transparent solar cell was fabricated on top of an aluminum/zinc oxide (ZnO) substrate with pre-patterned holes in it. The rest of the device was deposited via CVD and achieved a PCE of 5.9%. The transmittance of this device was not measured, instead photographs of the solar shades were presented where images of clouds could be seen through them. This publication, to the best of my knowledge marks the latest results presented on this topic. Clearly semi-transparent silicon solar cells can only be used for low transmittance cases (less than 20% transparent). Reports which claimed transmittances of 60% could be achieved did not discuss how the high transmittance would affect the PCE. The PCE would most likely be extremely low because cutting holes in the device or arranging micro cells on a transparent substrate significantly reduces the amount of light absorbed by the solar module. A semi-transparent solar cell that does not absorb visible light would be a better solution over silicon based solar cells.

The third generation solar cell have a much better potential over the first and second generation solar cells because organic materials can be tuned to only absorb light not visible to the human eye, such as infrared light. One of the first reports for semi-transparent organic solar cells was by Bailey-Salzman et al. in 2006 [31]. Bailey-Salzman et al. used a small molecule organic solar cell by thermally evaporating copper phthalocyanine (CuPc) and 3,4,9,10-perylenetetracarboxylic bis-benzimidazole (PTCBI) as active layer. The device was fabricated on a glass\ITO substrate with a thermally evaporated silver\ITO top electrode. The device exhibited 0.28% PCE and a transmittance of 60%. An opaque device with Ag as the top electrode exhibited a PCE of 1.3%. The PCE of this work is a major drawback along with the use of vacuum deposition technology making these devices impractically expensive.

A silver nanowire transparent electrode was first reported by Lee et al. as a solution processable alternative to ITO in 2008 [61]. Silver nanowires were fabricated via polyol method, deposited on a glass substrate via drop coating, and annealed at 200 °C for 30 minutes. The films exhibited a transmittance of 86% and a sheet resistance of 16 Ω/\square . It was found that the transmittance was composed of 66% direct light and 20% diffused or scattered light. A renovating sphere is required to detect the addition 20% of transmitted diffused light. Polymer solar cells made on top of the silver nanowire electrodes and ITO electrodes exhibited a PCE of 0.38% and 0.42%, respectively. This work did not report on a transparent solar cell.

In 2009 Heraeus-CleviosTM produced a PEDOT:PSS (poly(3,4-ethylenedioxythiophene: polystyrene sulfonate)) ink known as PH 1000 that was able to achieve conductivities as high as 1000 S/cm [62]. PEDOT:PSS, commonly used as a

solution processed transparent hole transport layer (HTL) in organic solar cells, with improved conductivity could now contend as a transparent electrode. One of the first reports on transparent PEDOT:PSS was from Kim et al. in 2011 [63]. They experimented with ethylene glycol additives in PEDOT:PSS PH 1000 inks and post treatments on PEDOT:PSS PH 1000 films and found the films conductivity was enhanced to 735 S/cm and 1418 S/cm, respectively. Small molecule solar cells were fabricated on an ITO or PEDOT:PSS transparent electrode and exhibited a PCE of 2.6% and 2.0%, respectively. The PEDOT:PSS transparent electrode exhibited a high sheet resistance of $65 \Omega/\square$ compared to ITO transmittance of 80%. The main drawback of this work was the high sheet resistance of the PEDOT:PSS electrode but low PCE of the solar cell. No semi-transparent solar cells were reported here.

Silver nanowire electrodes fabricated with very thin nanowires were reported by Hu et al. in 2010 [64]. Hu et al. found that using thinner wires with diameters ranging from 30-50 nm resulted in silver nanowire transparent electrodes with lower sheet resistance and transmittance than electrodes composed of nanowires with diameters ranging from 50-100 nm. The thinner nanowires electrodes achieved a sheet resistance of $8 \Omega/\square$ and a transmittance of 80% (65% transparent without diffused light). Atomic force microscopy (AFM) images showed the nanowire surface was extremely rough having peaks up to 800 nm which limits the use of these electrodes as a bottom electrode in a solar cell.

Xia et al. reported a PEDOT:PSS 4083 (4083 is a much less conductive ink than the PH1000 and typically used as an HTL) transparent electrode for a polymer solar cell in 2011 [65]. They used various solvent and water-co-solvent blend post treatments on

PEDOT:PSS films. A blend of 80% ethanol and 20% water resulted in the highest conductivity of 103 S/cm. The post treatment was drop coated onto the PEDOT:PSS film and allowed to evaporate. UV-visible absorption spectrum showed PSS peaks decreasing. Xia et al. proposed that the PSS was rearranging itself and allowing for less absorbance since no PSS could leave the film. It was postulated that the co-solvent blend was able to separate excess PSS species within the film to form PSSH. The hydrophilic PSSH species would surround itself with water and the more hydrophobic PEDOT:PSS chains would be surrounded by ethanol. As the PEDOT:PSS chains become more isolated they tend to form a more conductive linear structure. An ideal solvent will be able to isolate excess PSSH groups and penetrate into the PEDOT:PSS groups. Polymer solar cells were fabricated and exhibited PCE of 2.87% but this efficiency was never compared to an ITO reference device. This work presented excellent theory but the PEDOT:PSS electrode conductivity was very poor.

A semi-transparent small molecule solar cell that used ITO as both the anode and cathode was fabricated by Lunt et al. in 2011 [66]. Lunt et al. used thermal evaporation to fabricate the entire device. A distributed Bragg refractor (DBR) was incorporated on the top ITO electrode by sputtering sequential layers of TiO_2 and SiO_2 . The DBR was tuned such that it was transparent to light visible to humans but reflected infrared light back into the solar cell. For comparison, an opaque device was fabricated by replacing the top ITO electrode with a silver electrode. The semi-transparent solar cell achieved 1.7% efficiency with a total transmittance of 55% and the opaque reference device achieved a 2.4% efficiency. The drawback of this work is the low PCE and the use of ITO and vacuum deposition technology.

Leem et al. reported a silver nanowire electrode coated with TiO₂ based polymer solar cell device in 2011 [67]. The silver nanowire/TiO₂ electrode was used as a bottom electrode with the active layer P3HT:PCBM (poly(3-hexylthiophene):[6,6]-phenyl-C61-butyric acid methyl ester) spin coated on top. Normally silver nanowire electrodes could not be used as a bottom electrode due to their rough surface, but the TiO₂ was able to smooth out the rough silver nanowire electrode without acting as an insulating barrier. The transparent silver nanowire electrode exhibited a transmittance of 98% and sheet resistance of 34 Ω/□. The silver nanowire based devices exhibited 3.5% PCE and the ITO reference device exhibited 3.6% PCE. This work demonstrates that silver nanowire electrodes can compete with ITO. No transparent solar cell was made in this work.

A polymer solar cell fabricated on top of a silver nanowire/PEDOT:PSS transparent electrode was reported by Gaynor et al. in 2011 [68]. Silver nanowires on a glass slide were pressed into a PEDOT:PSS/glass substrates, leaving the nanowires embedded in the PEDOT:PSS layer. The PEDOT:PSS/silver nanowire transparent electrode exhibited a sheet resistance of 12 Ω/□ and transmittance of 86% (including diffused light). The silver nanowire electrode was shown to be flexible on a PET (polyethylene terephthalate) substrate, whereas the ITO has a brittle nature and exhibited a dramatic increase in sheet resistance after being bent. Polymer solar cells with silver nanowire/PEDOT:PSS or ITO semitransparent electrode both exhibited 4.2% efficiency. This further demonstrated that silver nanowire transparent electrodes can compete with ITO. No transparent solar cells were fabricated in this work.

A semi-transparent solar cell that utilized silver nanowire transparent electrode was reported by Chen et al. in 2012 [30]. This device used PBDTT-DPP (poly(2,60-4,8-

bis(5-ethylhexylthienyl)benzo-[1,2-b;3-4-b]dithiophene-alt-5-dibutyloctyl-3,6-bis(5-bromothiophen-2-yl)pyrrolo[3,4-c]pyrrole-1,4-dione):PCBM as the active layer which absorbed only in the infrared region. The device used ITO as the bottom electrode and a silver nanowire\ITO nanoparticles top electrode which exhibited a transmittance of 87% in the visible light region and a sheet resistance of $30 \Omega/\square$. Devices exhibited a PCE of 4.0% and transmittance of 66%. A mirror was held on the back side of the device to simulate the operation of an opaque solar cell and produced a PCE of 5.3%. The main drawback of this work was the use of ITO and a vacuum deposited bottom electrode.

A silver nanowire\aluminum doped zinc oxide (AZO) and silver nanowire\zinc oxide (ZnO) transparent electrode was explored by Stubhan et al. in 2012 [69]. Stubhan et al. deposited the silver nanowire transparent electrodes via doctor blading. The active layer P3HT:PCBM was also deposited via doctor blading. The AZO or ZnO layers were able to smooth out the rough surface of the bare nanowires. Despite the smoother surfaces, a reverse bias of -2 V was needed to burn short circuits made from the bottom silver nanowire electrode making contact with top thermally evaporated silver electrode. The solar cells exhibited a PCE of 2.9%, 2.5%, 3.2%, and 2.9% for devices with silver nanowires\AZO, silver nanowire\ZnO, ITO\AZO, and ITO\ZnO bottom transparent electrodes, respectively. The main drawback of this work was the need to burn shorts due to a rough silver nanowire surface.

A polymer solar cell with a PEDOT:PSS (PH 1000) transparent electrode was reported by Alemu et al. in 2012 [70]. Alemu et al. dropped methanol onto the PEDOT:PSS films heated to 140 °C. The resulting transparent electrodes exhibited a conductivity of 1110 S/cm. The PCE of ITO based devices and PEDOT:PSS based

devices were 3.7% and 3.7%, respectively. However, the PCE of the PEDOT:PSS based device was strongly depended on how far the cathode was placed from the PEDOT:PSS anode. Anodes placed far away from the cathode on the PEDOT:PSS based device resulted in PCE of 3.1%, whereas the ITO device exhibited no PCE degradation. The sheet resistance and transmittance of the PEDOT:PSS transparent electrode was $164 \Omega/\square$ and 90%, respectively. The high sheet resistance for the PEDOT:PSS electrode compared to the ITO (typically $20 \Omega/\square$) seems to make this work unrealistic. No discussion on repeatability of this work was presented which likely means that the authors presented the devices that exhibited unusually high PCE with the ITO devices of average PCE.

Reinhard et al. compared silver nanowire/PEDOT:PSS anode with silver nanowire/vanadium oxide (V_2O_5) as an anode in 2013 [71]. Charge mapping from light beam induced current demonstrated that the V_2O_5 based electrodes exhibited poor charge transport compared to the PEDOT:PSS alternative. The PCE for devices with a silver nanowire/ V_2O_5 vs silver nanowires/PEDOT:PSS electrode was found to be 0.84% vs 2.4%.

A fully solution processed polymer solar cell was fabricated by Guo et al. in 2013 [72]. Guo et al. employed a silver nanowire/AZO and a silver nanowire/PEDOT:PSS semi-transparent electrode in an inverted type structure. The PCE of the device with silver nanowires as both top and bottom electrodes was 2.2% compared to 3.5% for the solar cells with thermally evaporated silver and ITO as top and bottom electrodes. The lower PCE for the silver nanowire based device was due to its transparency. No semi-transparent solar cell was fabricated in this work.

The stability of silver nanowires under electrical stress was studied by Khaligh et al. in 2013 [73]. Khaligh et al. found that the silver nanowires electrode with a sheet resistance of $12 \Omega/\square$ lasted for only 17 days. By increasing the sheet resistance to $37 \Omega/\square$, the life time was reduced to less than one day. Khaligh et al. attributed the failure to Joule heating breaking electrical connection between nanowires and possible corrosion from sulfur present in the air. This work alerted to a big need for improved stability of silver nanowire electrodes.

Kim et al. reported a PEDOT:PSS transparent electrode with conductivity of 4380 S/cm in 2014 [74]. The high conductivity of the PEDOT:PSS electrode was very similar to the conductivity of ITO. Kim et al. achieved a high conductivity by soaking the PEDOT:PSS films in sulfuric acid. The proposed mechanism was attributed to the sulfuric acid removing excess PSS and hydrolyzing to separate the PEDOT and PSS chains and form a more optimal morphology. A transparent PEDOT:PSS electrode with sheet resistance of $46 \Omega/\square$ and transmittance of 90% was used to fabricate a polymer solar cell. The PCE of ITO and PEDOT:PSS based devices was 7.2% and 6.6%, respectively. The main disadvantage of this work was the use of highly corrosive acids to enhance the conductivity of PEDOT:PSS.

A semi-transparent perovskite solar cell was reported by Guo et al. in 2015 [75]. Guo et al. used ITO as the bottom electrode and ZnO nanoparticles\silver nanowires as top electrode. The ZnO nanoparticles served as a buffer layer to protect the perovskite\PCBM layers from spray coated silver nanowire electrodes. This resulted in a transparency of 21.5% and PCE of 8.5%, which was comparable to the PCE of 10.7% for the device with an opaque silver electrode. The authors noted that devices with nanowire

electrodes were extremely unstable even when kept in a nitrogen gas environment. The device instability was attributed to iodine ions within the perovskite bonding with silver nanowires to form an insulating layer. Along with poor stability, these devices exhibited low transmittance due to the perovskite layer absorbing visible light. Semi-transparent solar cells should be fabricated with materials that primarily absorb UV or infrared light.

A perovskite solar cell fabricated on top of a transparent PEDOT:PSS electrode reported by Sun et al. in 2015 by dropping methanesulfonic acid (MSA) onto PEDOT:PSS films during annealing. A two layer PEDOT:PSS electrode exhibited conductivity of 2540 S/cm ($50 \Omega/\square$) and transmittance of 92%. The PCE of the perovskite solar cells fabricated on top of a glass\ITO, glass\PEDOT:PSS, and PET\PEDOT:PSS was 15.6%, 14.7%, and 10.6%, respectively. The disadvantage of this work is the use of highly corrosive MSA to enhance the PEDOT:PSS.

In summary, a fully solution-processable, ITO-free, semi-transparent solar cell has yet to be reported. From the previous works, silver nanowires seem to be a very promising candidate, however, very little work has been done to improve electrode stability under electrical stress. PEDOT:PSS as a transparent cathode has also emerged to have excellent conductivities similar to ITO, however these have only been achieved with highly corrosive acids. An acid free method will be needed to realize low-cost, fully-solution-processed device compatible with roll-to-roll processing. Moreover, all the previous work on semi-transparent solar cells has relied on an ITO transparent electrode or vacuum deposition technology. This dissertation aims to report the first truly fully solution processed semi-transparent solar cell for power generating window applications.

1.3 MOTIVATION

There is a need for a fully-solution-processed, ITO-free semi-transparent solar cell for power generating window applications.

1.4 OBJECTIVES

The goal of this work was to fabricate a fully solution processed semi-transparent solar cell without the use of ITO or vacuum deposition technology. To do this, a transparent solution processed anode and cathode must be designed and an active layer that does not absorb visible light must be selected. PDPP3T was chosen due to its low absorbance of light visible to human eyes and high PCE of 4.5% [76]. Silver nanowires and PEDOT:PSS were selected as cathode and anode materials, respectively. To develop a semi-transparent solar cell, the following tasks were defined:

- 1) Fabricate a transparent silver nanowire electrode (cathode) and PEDOT:PSS electrode (anode) with transparency greater than 80% and sheet resistance less than $50 \Omega/\square$
- 2) Improve silver nanowire lifetime to longer than 6000 hours of constant electrical stress
- 3) Fabricate a semitransparent solar cell with average transmittance greater than 50% within the visible light region (450 - 750 nm) and PCE greater than 4% using PEDOT:PSS and silver nanowire semitransparent electrodes.

CHAPTER 2 THEORY

2.1 OPERATING PRINCIPLES OF SOLAR CELLS

Solar cells are devices that convert energy from sunlight into electrical energy.

Regardless of the type of solar cell, there are common parameters used for characterization. All of these parameters can be found or derived from current-voltage (I-V) curves. These common parameters are short circuit current (I_{sc}), fill factor (FF), open circuit voltage (V_{oc}), and efficiency (η).

Figure 2.1 shows an I-V curve of a solar cell with V_{oc} , I_{sc} , maximum power point (P_m), voltage at maximum power point (V_m), and current at maximum power point (I_m) labeled. The V_{oc} is defined as the maximum output voltage of the solar cell. From the graph the V_{oc} can be found when no load is attached to the solar cell and current flow is zero. The I_{sc} is defined as the maximum current output from the device and is found by creating a short circuit across the positive and negative terminals of the solar cell. In a short circuit, there is no voltage potential between the positive and negative terminals. For both open circuit and short circuit cases, no power will flow through the device. Power is defined by

$$P = V \times I \quad (2.1)$$

where P is power, V is voltage, and I is current. The operating point where the solar cell delivers the maximum amount of power is called the maximum power point (P_m). The corresponding voltage and current values associated with the maximum power point are denoted as V_m and I_m , respectively. A perfect solar cell with no internal losses would have V_m and I_m equal to V_{oc} and I_{sc} , respectively. FF is used to define how far away from

perfect operation a solar cell is and can be understood as the checkered box area divided by the gray wavy lined area from Figure 2.1). FF can be calculated by

$$FF = \frac{V_m I_m}{V_{oc} I_{sc}} \quad (2.2)$$

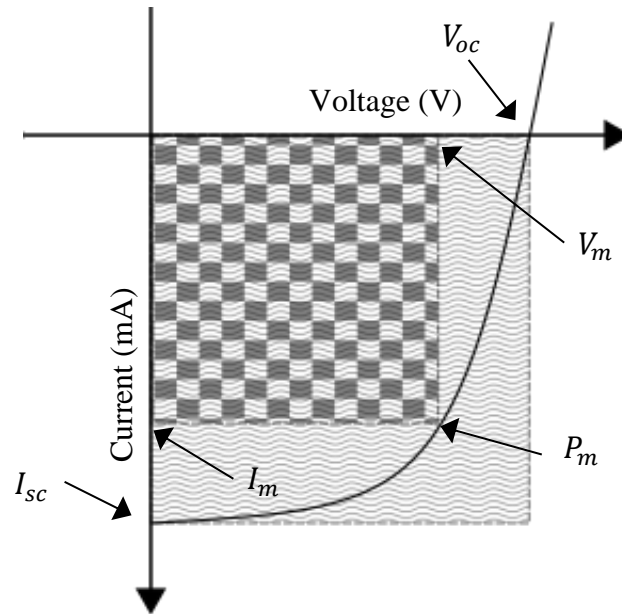


Figure 2.1. I-V curve of a solar cell with short circuit current (I_{sc}), open circuit voltage (V_{oc}), maximum power point (P_m), voltage at maximum power point (V_m), and current at maximum power point (I_m) labeled.

The solar cell power conversion efficiency (PCE) can be calculated by

$$\eta = \frac{V_{oc} I_{sc} FF}{P_{light}} = \frac{V_m I_m}{P_{light}} \quad (2.3)$$

where $V_{oc} I_{sc} FF$ is the power generated by the solar cell and P_{light} is the power from the light irradiated on the solar cell. The light used to test solar cell efficiencies is typically generated by a Xenon arc lamp with filters that emit a light spectrum similar to that of the sun. The distance the solar cell is placed from the lamp will determine the power density

of the light irradiated on it. A power density of 100 mW/cm^2 is normally used to characterize the solar cell. This power density standard of 100 mW/cm^2 is denoted as AM 1.5 lighting.

2.2 EQUIVALENT CIRCUIT OF SOLAR CELLS

The single diode model, shown in Figure 2.2, is the simplest solar cell model and works very well in most cases. Under dark conditions (Figure 2.2 (a)) no light shines on the solar cell, however a small amount of current known as dark current (I_D) can be measured. Dark current is generated by thermal excitation of electrons and holes within the solar cell and will ultimately degrade the device performance because it flows in opposition of the photocurrent (I_{ph}) (as depicted in Figure 2.2 (b)). I_{ph} is the electrical current generated when light radiates on the solar cell.

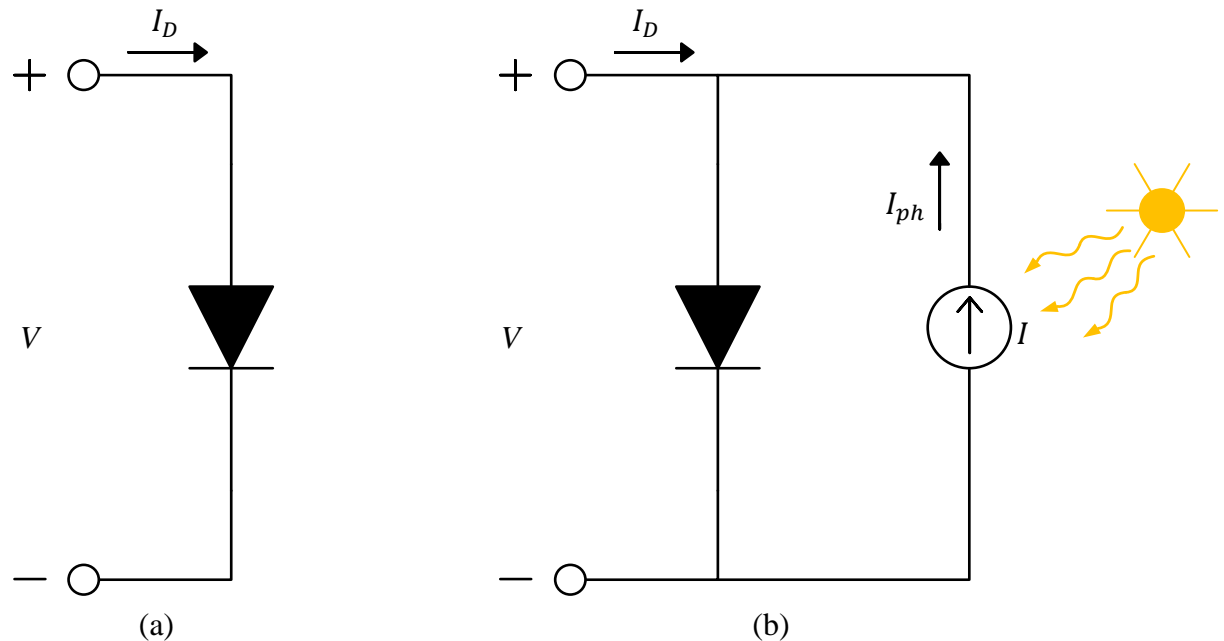


Figure 2.2. Single diode model of a solar cell under (a) dark and (b) illuminated conditions.

The total output current, $I(V)$, from the solar cell under illuminated conditions can be expressed as a function of voltage

$$I(V) = I_{ph} - I_D(V) \quad (2.4)$$

where $I_D(V)$ is dark current, which can be described by

$$I_D(V) = I_0 \left(e^{\frac{qV}{k_B T}} - 1 \right) \quad (2.5)$$

where I_0 is a constant typically used as a fitting parameter but is related to the flow of electrons and holes (charge carriers) under a constant electric field (i.e. drift current) within the device, q is the elementary charge of an electron, V is the operating voltage of the solar cell, k_b is Boltzmann's constant equal to $8.617 \times 10^{-5} \frac{eV}{K}$, and T is the temperature of the solar cell typically assumed to be room temperature (298.15 K).

By inserting equation 2.5 into equation 2.4 the I_{sc} and V_{oc} of the solar cell can be solved for. I_{sc} is found by setting $V = 0$ which yields

$$I_{sc} = I_{ph} - I_0, \quad (2.6)$$

and V_{oc} can be solved for by setting $I(V) = 0$ which yields

$$V_{oc} = \frac{k_B T}{q} \ln \left(\frac{I_{ph}}{I_0} + 1 \right). \quad (2.7)$$

I_{ph} can be described by the following equation

$$I_{ph} = q \int_0^\infty \eta_c(E) (1 - R(E)) a(E) b_s(E) dE \quad (2.8)$$

where E is photon energy, $\eta_c(E)$ is the probability that generated charge carriers will be collected at the solar cell terminals, $R(E)$ is the fraction of light reflected from the device making $1 - R(E)$ the fraction of light that enters into the solar cell, $a(E)$ is the fraction of light capable of being absorbed by the solar cell, and $b_s(E)$ is the photon flux (typically from the sun) with units *photons/s*. The $(1 - R(E))a(E)b_s(E)$ portion of

Equation 2.8 can be understood as the total number of photons of energy E absorbed by the solar cell. Equation 2.8 is integrated from 0 to infinity to cover all the different photon energies. In the case of solar cells, the integral can be simplified to only include photon energies radiated by the sun. Equation 2.8 can be simplified to

$$I_{ph} = q \int_0^{\infty} EQE(E)b_s(E)dE \quad (2.9)$$

where $EQE(E)$ is the external quantum efficiency, which is number of charge carriers extracted out of the solar cell divided by the number of photons with energy E shined on the solar cell. Similar to $EQE(E)$, internal quantum efficiency, $IQE(E)$, is the number of charge carriers extracted out of the solar cell divided by the number of photons absorbed by the solar cell. Equation 2.8 can also be expressed in terms of $IQE(E)$

$$I_{ph} = q \int_0^{\infty} IQE(E)(1 - R(E))b_s(E)dE \quad (2.10)$$

The single diode model can be expanded to incorporate series (R_s) and shunt (R_{sh}) resistance as depicted in Figure 2.3. R_s and R_{sh} represent internal resistances within the solar cell device. From Figure 2.3 it can be seen that the current generated from the solar cell is further reduced from R_{sh} . R_{sh} represents current that remains trapped (also known as leakage current) in the solar cell device, which can be due to internal device defects. Ideally, R_{sh} should have an infinity large resistance so that no current can travel through. R_s can be caused by poor contact between the different layers within a solar cell and impedes current flow out of the device. Ideally, R_s would be equal to zero.

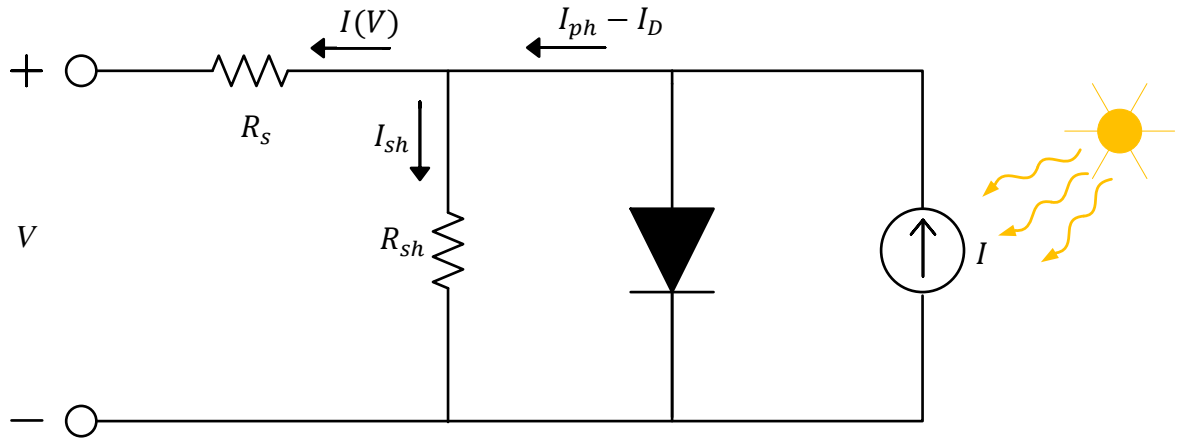


Figure 2.3. Single diode model of a solar cell for illuminated case with series (R_s) and shunt (R_{sh}) resistance depicted.

R_{sh} and R_s influence on the output current can be described by

$$I(V) = I_{ph} - I_0 \left(e^{\frac{q(V+I(V)R_s)}{k_B T}} \right) - \frac{V+I(V)R_s}{R_{sh}} \quad (2.11)$$

This equation can be solved using an iterative process where the previous solution to $I(V)$ is used to solve the current iteration. To start the first iteration, all $I(V)$ values on the right hand side of the equation are set to zero.

Figure 2.4 shows the effect (a) decreasing R_{sh} and (b) increasing R_s have on the I-V curve. By decreasing R_{sh} or increasing R_s , FF is reduced. R_{sh} can be calculated from the I-V curve by finding the slope of the line where it connects with the y-axis. Similarly, R_s can be calculated from the slope of the line that crosses the x-axis.

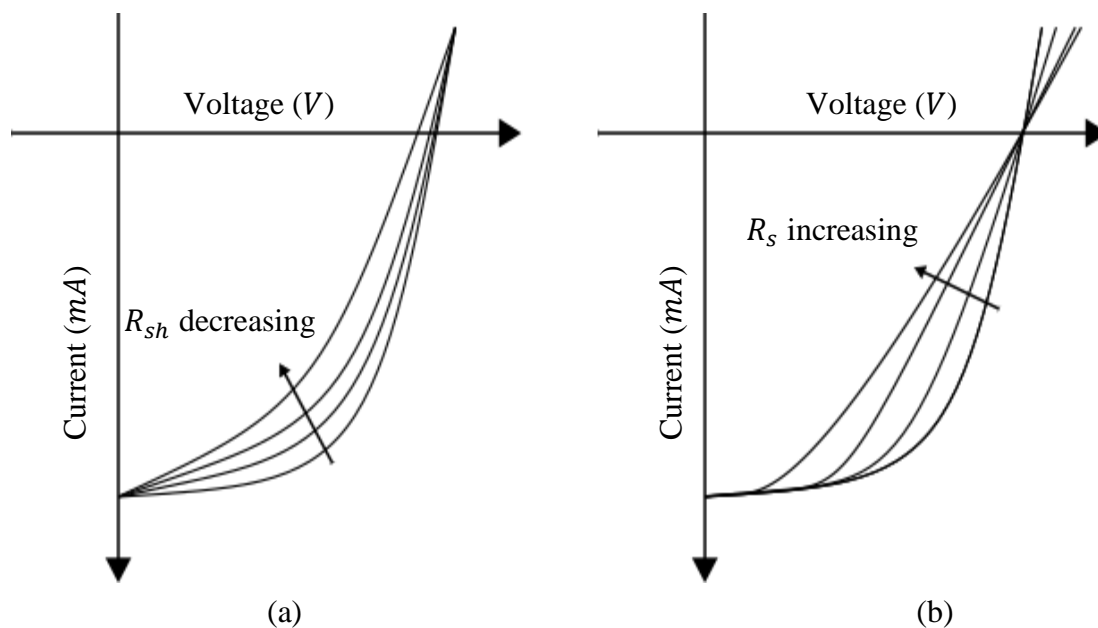


Figure 2.4. Effect of (a) decreasing R_{sh} and (b) increasing R_s have on the I-V curve.

It should be noted that equations 2.1 through 2.11 can all be expressed in terms of current density (J). Current density is current (I) divided by the solar cell area. For example, a solar cell with $I_{sc} = 1.92 \text{ mA}$ and device area of 0.16 cm^2 would result in a current density of $J_{sc} = 12.0 \text{ mA/cm}^2$.

2.3 SINGLE JUNCTION SOLAR CELL PHYSICS

Solar cells rely on semiconducting materials to absorb light and generate free charge carriers. Semiconductors are materials that do not conduct electricity as well as conductors, but are not an insulating material either. The conductivity of semiconductors typically falls within the range of 10^{-7} S cm to 10^3 S cm [77], however conductivities greater than 1 S cm are usually only achieved by doping the material (see section 2.3.1).

All materials (conductors, semiconductors, and insulators) have two kinds of energy states a valence band and conduction band. Different names such as lowest unoccupied molecular orbital (LUMO) and highest occupied molecular orbital (HOMO)

may be used for different materials but the concept remains the same as depicted in Figure 2.5. The valence band is where electrons rest in a non-conductive state. If electrons gain enough energy, they are promoted to the conduction band and are able to move freely. Insulators have a very large energy gap (E_g) between the valence band and conduction band and consequently do not conduct electricity. The valence states overlap the conduction states in conductors and thus are able to conduct electricity extremely well. Semiconductors have a small gap between the valence states and conduction states, and need some additional energy to conduct electricity.

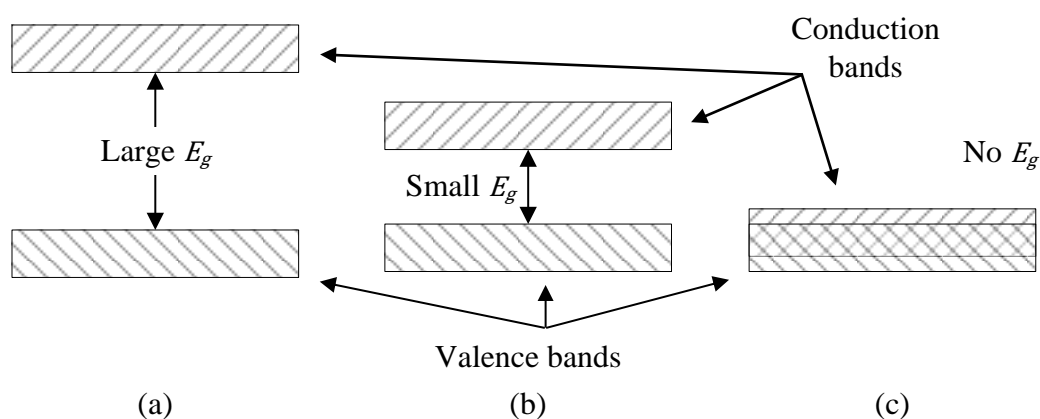


Figure 2.5. Energy band diagram of (a) insulator, (b) semiconductor, and (c) conductor.

In the case of solar cells, this additional energy comes from sunlight absorbed into the material. The size of the energy gap between the valence band and conduction band is called the band gap. The energy of the light absorbed by the electron must be equal to or greater than the band gap energy in order for an electron to become promoted to a conductive band. The electrons within the conduction band can be used to do work such as charging a battery or powering lightbulbs.

2.3.1 SILICON SOLAR CELLS

Intrinsic silicon is not very electrically conductive due to a lack of free charge carriers in the material. A silicon atom has four electrons in its valence state and each of these electrons are being used to bond with four other neighboring atoms. Because each electron is bonded with another atom, there are no free electrons or holes to conduct electricity. Conductivity (σ) measures how well a material is able to conduct electricity and is defined as

$$\sigma = qn\mu_n + qp\mu_p \quad (2.12)$$

where n is the number of free electrons, p is the number of free holes, and μ_n and μ_p are the mobility of the electrons and holes, respectively. From Equation 2.12, very small values of n and p , result in low conductivity.

Free charge carriers can be introduced by a process called doping, where impurities such as boron or phosphorous are added into the silicon crystal lattice as shown in Figure 2.6. Unlike silicon, boron and phosphorus have three and five valence electrons, respectively. When placed into the silicon lattice, boron leaves one atom without a bond or a free hole charge carrier (positively charge) and phosphorus contains one extra electron to serve as a free electron charge carrier (negative charge). These free charge carriers can move about within the crystal lattice by jumping from atom to atom. The high charge carrier mobility of silicon relies on its crystallinity. The introduction of dopants into the silicon structure causes defects within the crystal structure and in turn reduces the charge carrier mobility. From Equation 2.12 it can be inferred that too much doping will begin to reduce the conductivity because the mobility of electrons and holes becomes compromised.

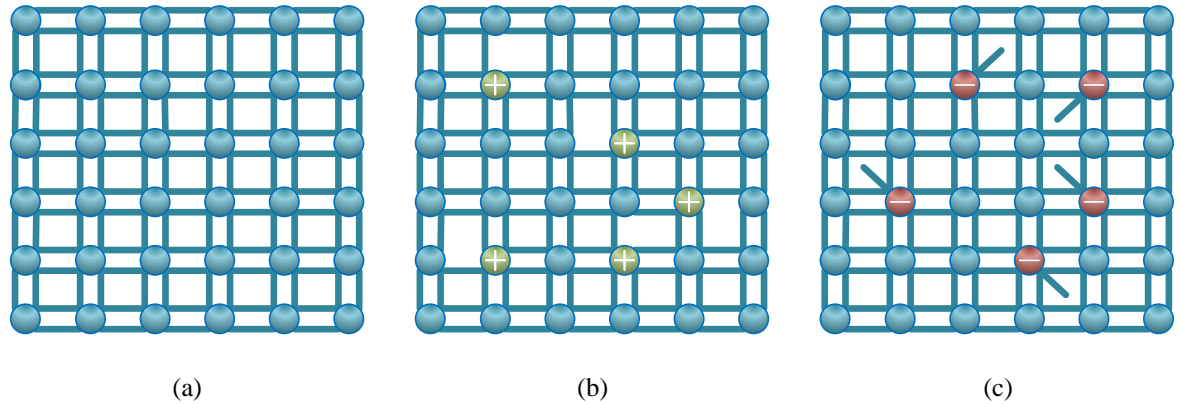


Figure 2.6. (a) intrinsic silicon crystal lattice, (b) silicon crystal lattice doped with boron, and (c) silicon crystal lattice doped with phosphorus.

A p-n junction is the fundamental basis for silicon solar cell devices and is formed by placing a p-type silicon crystal lattice up against a n-type crystal lattice. Figure 2.7 shows a p-n junction (a) before and (b) and after the free charge carriers reach equilibrium. Before equilibrium, the negatively charged electrons in the n-type portion are attracted to the positively charged holes in the p-type portion. The electrons then move to fill up the empty spaces (holes) which creates negatively charged boron ions and leaves behind positively charged phosphorus ions. After some time, the negatively charged boron ions and positively charged phosphorus ions create an internal electric field \vec{E}_D strong enough to repel any additional electrons or holes from recombining together. The area where \vec{E}_D repels any further electron hole interaction is known as the depletion region (also known as the space charge region).

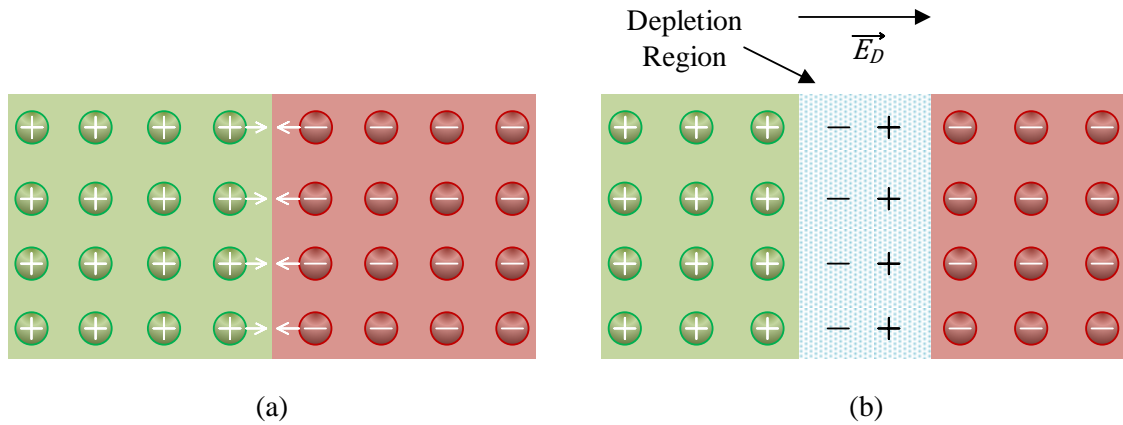


Figure 2.7. P-n junction (a) before and (b) and after the free charge carriers reach equilibrium

Figure 2.8 illustrates light being absorbed into a solar cell and freeing an electron-hole pair, which is used to power a lightbulb. The electron-hole pairs are driven apart by the internal electric field within the space charge region. Once the electron and hole have drifted into the p-type and n-type region, respectively, they diffuse toward their respective electrodes where they are collected and used to do work such as charging a battery, or powering a light.

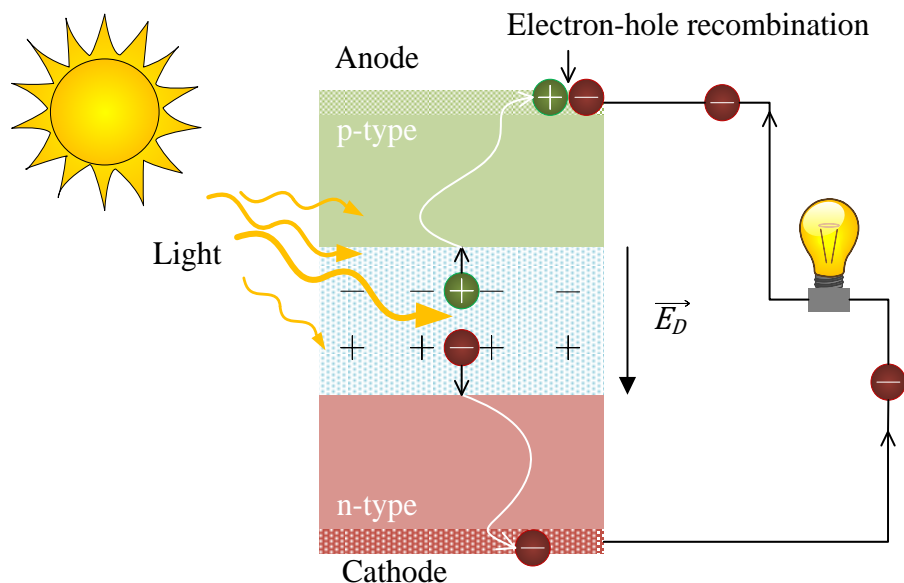


Figure 2.8. Light absorbed into a solar cell frees an electron-hole pair, which is used to power a lightbulb.

2.3.2 POLYMER SOLAR CELLS

Polymer solar cells use semiconducting polymer materials as the light absorbing layer. The most popular combination is a polymer donor material (similar to p-type in silicon) and a fullerene acceptor material (similar to n-type in silicon). The term ‘donor’ and ‘acceptor’ are assigned because the polymer donates an electron and the fullerene accepts the electron. First attempts at polymer solar cells used a bi-layer structure similar to Figure 2.8 where the donor layer and acceptor layer are stacked one on top of the other. This however resulted in very poor efficiencies due to low light absorption. In reality, organic materials are able to absorb light better than inorganic materials such as silicon; however, due to their low conductivity, the organic active layer must be made extremely thin, which inhibits light absorption. Thicker donor and acceptor layers would

result in electron or hole recombination before they could be collected at their respective electrodes.

The bulk heterojunction (BHJ) structure for (a) regular (p-i-n) and (b) inverted (n-i-p) polymer solar cells is shown in Figure 2.9. The BHJ was used to increase the thickness of the donor/acceptor layers without greatly increasing the risk of electron-hole recombination. The increased thickness of the donor/acceptor layers (also referred to as the active layer) improved light absorption and overall PCE. The BHJ creates a donor-acceptor interface throughout the entire active layer so an electron-hole pair do not have to travel far to reach this interface despite having a thicker active layer. However, this means that charge carriers are also generated close to their opposite electrode (i.e. holes generated close to the anode and electrons the cathode). The opposite charge carriers within the electrode may recombine with them and reduce the device PCE. To prevent this electron-hole recombination, hole transport layers (also known as electron blocking layer) and electron transport layer (or hole blocking layer) are incorporated into the device to block any of the charge carriers from entering into the wrong electrode while safely transporting the correct charge carrier to its respective electrode. As seen in Figure 2.9, the regular structure refers to having the cathode as a transparent electrode (and having a transparent hole transport layer) whereas, inverted structure has the anode as the transparent electrode (and a transparent electron transport layer).

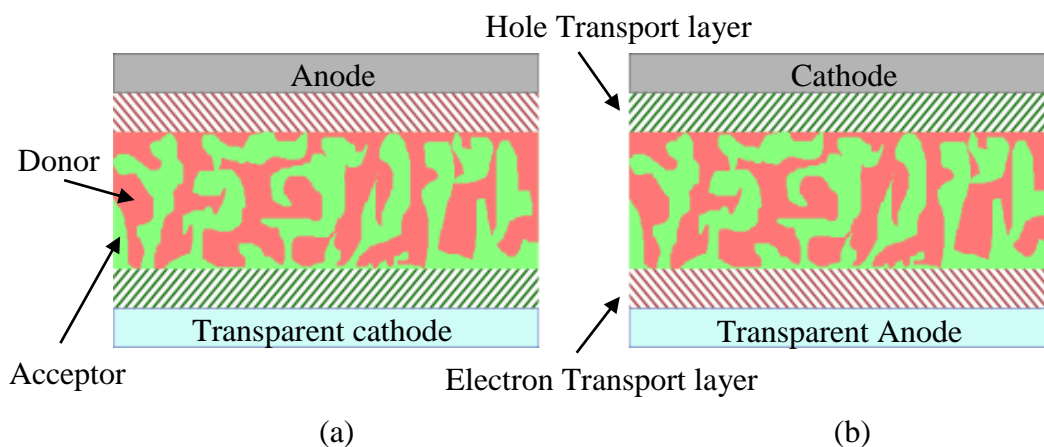


Figure 2.9. HJB structure for (a) regular and (b) inverted polymer solar cells.

2.3.3 PEROVSKITE SOLAR CELLS

Perovskite solar cell use perovskite crystals as the active layer for light absorption. Figure 2.10 shows the perovskite crystal structure. ABX_3 is the generic chemical formula of a perovskite crystal. In photovoltaic applications A is $CH_3NH_3^+$, B is Sn^{2+} or Pb^{2+} , and X is typically F^- , Cl^- , Br^- , or I^- [59]. The perovskite solar cell has a unique ambipolar charge-transport where both holes and electrons can freely flow through the material [78, 79], thus there is no need for a p-n junction or donor-acceptor interface. Films can be deposited via vapor growth or solution processing and can exhibit similar architecture to polymer solar cells (Figure 2.9). Because of the crystalline nature of perovskite films, some reports claiming an electron-hole diffusion length greater than 1 micron [80]. Moreover, perovskite solar cells exhibit excellent light absorption with EQE greater than 80% from 350 - 775 nm [56]. In one sense, perovskite solar cells have the best qualities of organic, and inorganic solar cells with low cost fabrication, high light absorption, and excellent charge transport.

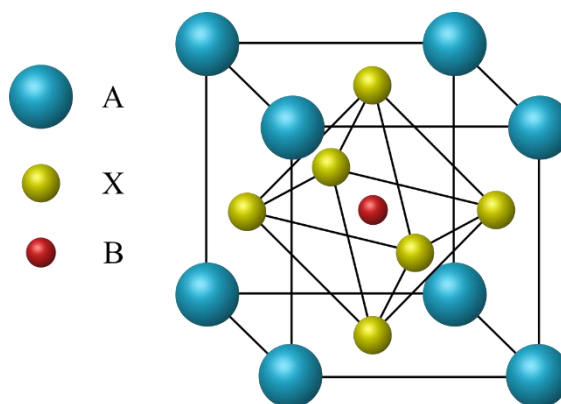


Figure 2.10. Perovskite crystal structure.

The drawback of perovskite solar cells is their instability. The perovskite crystal is very sensitive to moisture and high temperature (e.g. 100 °C) and can easily break down. Moreover, the toxicity of lead raises environmental concerns and essentially eliminates the possibility of commercialization [59]. Although lead free perovskite solar cells have been tried; their efficiencies are around 5.7% [59].

2.4 SEMITRANSSPARENT SOLAR CELLS

Semitransparent solar cells differ in that they can allow partial visible light (400 nm - 780 nm) to pass through them, but generate power by absorbing IR (780 nm - 2500 nm) or UV (200 nm – 400 nm) light. In the case of silicon solar cells, visible and some IR light is absorbed. To make these devices transparent, they must be punctured to make small holes so that light to shine through. The more transparent these devices are, however, the less efficient they become because there is less area to absorb light. There is a limit as to how transparent silicon can be made, although for security window applications the silicon models of 20% transmittance and 10% efficiency would work fine [81]. For applications where greater than 20% efficiency is needed organic solar cells are the best option because they can be tuned to absorb only IR light. A semitransparent

organic solar cell would utilize both a semitransparent anode, cathode, hole transport layer, and electron transport layer. This makes deciphering whether or not the device is inverted or regular structure difficult. While many reports choose to not claim any structure type, others simply base it on which electrode is the first layer. If the solar cell is fabricated on top of the anode it is an inverted structure, if the cathode then regular structure.

2.4.1 BANDGAP AND LIGHT ABSORPTION

The energy of light must be equal to or greater than the energy gap between the conductive band (LUMO for OSC) and valence band (HOMO for OSC). The energy of light can be calculated by

$$E = \frac{hc}{\lambda} \quad (2.13)$$

where E is energy, h is planks constant ($4.136 \times 10^{-15} \text{ eV} \cdot \text{s}$), c is the speed of light ($3 \times 10^8 \text{ m/s}$), and λ is the wavelength of the light. In the case of polymer solar cells, the chemical structure can be tuned such that significant absorption occurs in IR region but not in the visible light region. This is due to the length of the chemical bonds and degrees of freedom through which they can rotate and vibrate. The vibrations within the molecular structure are able to resonate with particular wave lengths of light better than others. This allows for selectively tuning which can result in semitransparent polymers which dominantly absorb in the IR light region and minimal absorption in the visible light region.

2.4.2 PEDOT:PSS TRANSPARENT ELECTRODES

PEDOT:PSS is a conductive polymer blend composed of conductive PEDOT and a highly soluble PSS polymer. In its natural state, PEDOT is not very conductive or

stable, however, it is easily doped and highly stable after being oxidized from air exposure [82]. Figure 2.11 shows PEDOT in its natural (a)(b) and oxidized (c)(d) state for the benzoid (a)(c) and quinoid (b)(d) structures. PEDOT doping can range from no monomers to one third of every monomer [82]. The benzoid structure typically takes on a more coiled shape because the single bonds between each monomer are flexible. The quinoid structure has double bonds between each monomer which are less flexible and results in a more rigid straight line like shape. Because the quinoid tends to hold itself more in a straight line, it is the most conductive form of PEDOT [83]. The polymer chain that form straight lines improve intra-chain-conductivity because charges can travel further distances before needing to hop to another neighboring chain. A coiled up polymer chain has extremely poor intra-chain-conductivity as delocalized charges (charges that move freely along the polymer backbone) do not travel far, but heavily relies on inter-chain-conductive where charges need to hop from one chain to the next in order to move about.

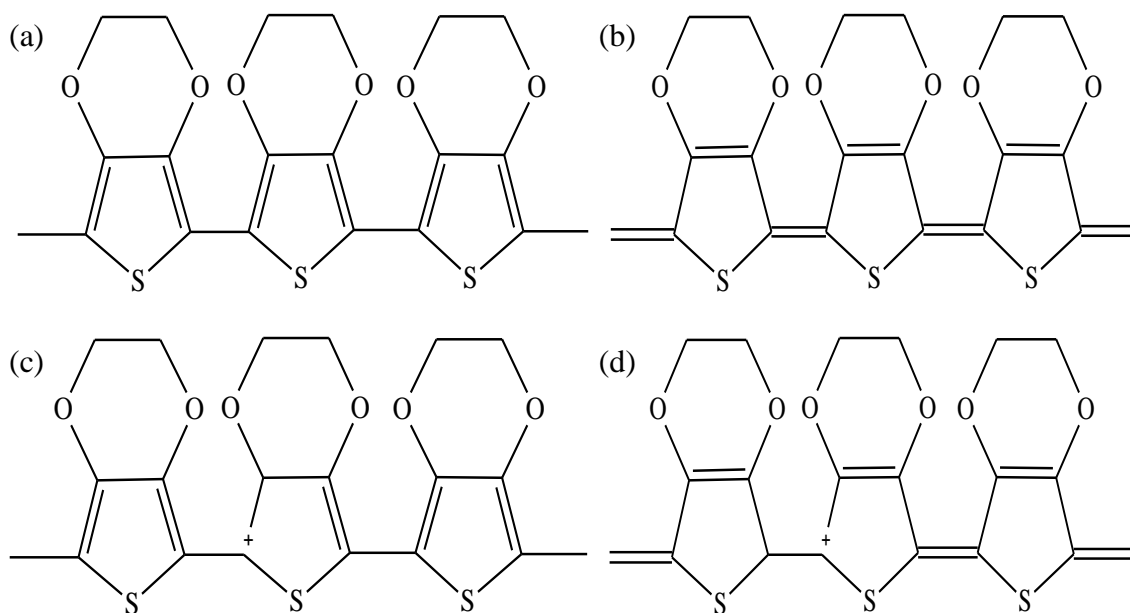


Figure 2.11. PEDOT in its natural (a)(b) and oxidized (c)(d) form and benzoid (a)(c) and quinoid (b)(d) structures.

Upon its discovery, PEDOT was found to be insoluble and unable to melt [84]. By blending PEDOT with PSS the polymer blend can be easily dispersed in water [84]. PEDOT in its doped state is a polycation (positively charged polymer), which was found to be an insoluble polymer unless the cation charges were neutralized [85]. PSS is water soluble and can serve as a counter ion to balance out the positive charges from the PEDOT chain. PSS can also be used to synthesize PEDOT by acting as an oxidizing agent for the EDOT monomer and initiator in the polymerization process. The end result is PEDOT:PSS as the PEDOT and PSS are bound together by coulombic interactions as shown in Figure 2.12. PSS is insulating and ultimately reduces the conductivity of pristine PEDOT, however, highly ordered PEDOT:PSS morphology allows for some conductivity via percolation of conductive sites [86].

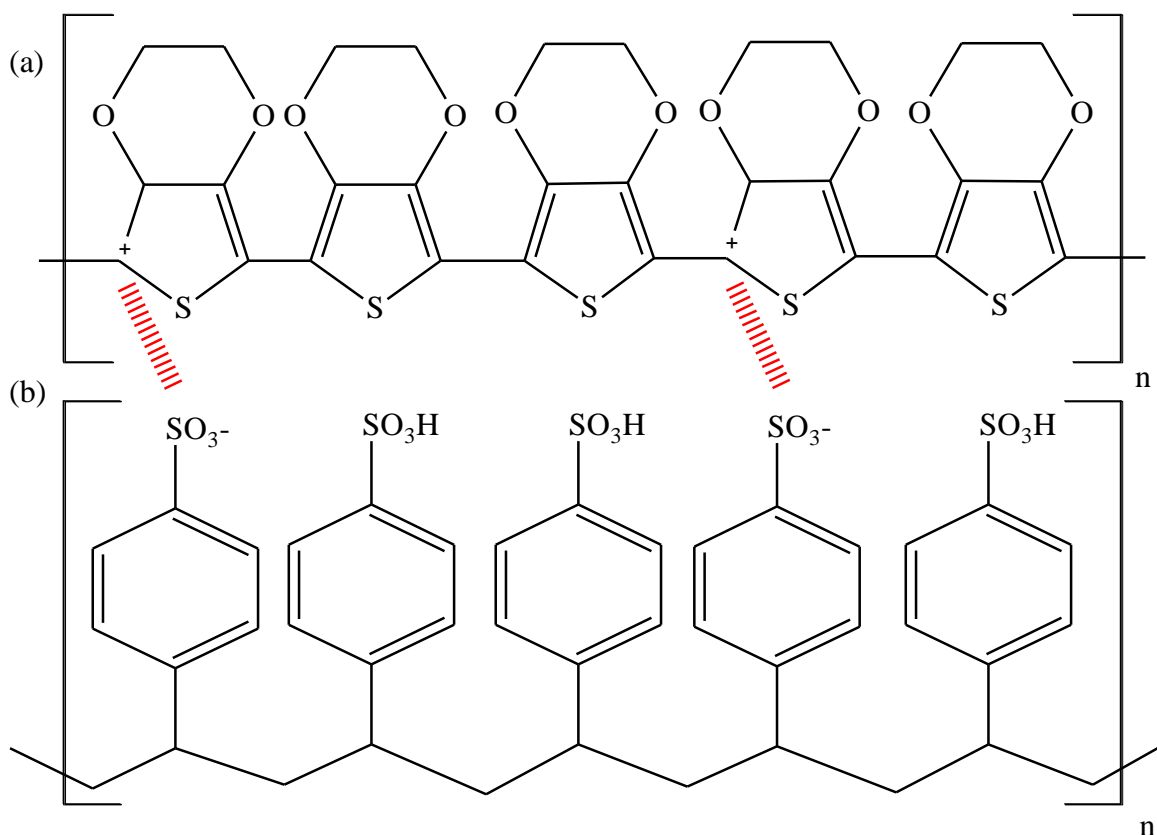


Figure 2.12. (a) Doped PEDOT with positive charge coulombically bound to (b) PSS species.

One big misconception about the PEDOT:PSS is that the PSS is actually doping the PEDOT and enhancing the overall conductivity of the fill. A study done by Stocker et al. demonstrated that the addition of PSS adversely effected the conductivity of PEDOT and did not increase the charge carrier concentration [87]. Although PSS acts as an oxidizing agent during the synthesis (i.e. the PEDOT becomes doped by introduction of additional free charge carriers), this phenomenon is not dependent on the continued presents of PSS within the PEDOT:PSS film. By adding more PSS to the PEDOT:PSS complex, the number of free charge carriers does not increase. The only role PSS plays in

charge transport is to keep the PEDOT evenly dispersed in the water solution so that it can form a good percolation network upon being deposited as a film [85].

Several reports have treated PEDOT:PSS films with strong acids, such as sulfuric acid (H_2SO_4), methanesulfonic acid ($\text{CH}_3\text{SO}_3\text{H}$), and formic acid (HCO_2H) to greatly enhance the conductivity of PEDOT:PSS films [70, 74, 88, 89]. The proposed mechanisms for these enhancements were coulombic screening between the PEDOT and PSS specie due to high dielectric constant of acid, dissolving and removing access PSS from the PEDOT:PSS in the film, deprotonation of acid (donates a H^+) with PSS^- to form PSSH (thus the PSSH will not interact with the PEDOT and can be easily removed from the film), and autoprotolysis of H_2SO_4 (yielding H_3SO_4^+ and HSO_4^-) to wash away the PSS species and serve as a temporary counter-ion so that PEDOT can form a linear structure.

PEDOT:PSS is already dispersed in water, which has an equal or higher dielectric constant than many of the acids previously listed, so the dielectric constant is not likely the root cause of the conductivity enhancement. Autoprotolysis and deprotonation seem most reasonable because the positive and negative ions could actually separate the PEDOT^+ from the PSS^- , moreover, explain the loss of PSS^- species through the formation of PSSH which separates from the film due to a lack in charge. Without the coulombic counterbalance from the PSS^- species, the PEDOT^+ can easily reorder into a linear structure to minimize the interaction of the positive charges along the polymer chain. The HSO_4^- ions mixed with PEDOT^+ would more likely result in a ladder type structure versus a scrambled egg type structure as shown in Figure 2.13 [85]. The sulfuric acid can be removed from the film after rinsing with water and annealing.

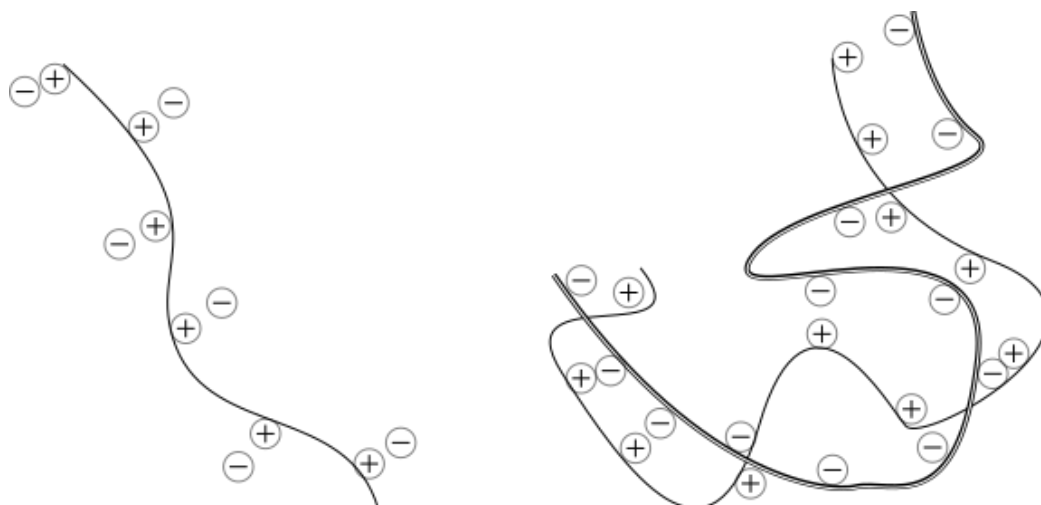


Figure 2.13. (a) ladder type structure and (b) scrambled egg type structure for a polycation and polyanion blend.

Strong acids, however, are not compatible with low-cost, solution-processed mass production methods. The highly corrosive nature of strong acids will greatly complicate and introduce hazards into the manufacturing process. To avoid these difficulties, PEDOT:PSS can also be treated with common solvents such as ethylene glycol, dimethyl sulfoxide (DMSO), ethanol, and methanol to enhance the conductivity. Solvents are used as additives to the PEDOT:PSS solution prior to film deposition or as a post-treatment on PEDOT:PSS films which results in enhanced conductivity.

DMSO and ethylene glycol have been the most successful solvent additives to enhance the conductivity of PEDOT:PSS films. Many of the mechanisms follow the same line as described in the acid treatments: remove excess PSS from the film and provide coulombic screening to allow for film reorganization. One commonality of solvent additives used to enhance the conductivity of PEDOT:PSS is the high boiling point and having a strong polarity or polar functional groups [65, 83]. Although there is still much debate on the exact mechanism, the most reasonable would seem that the high

boiling point solvent additives results more time for the film to rearrange itself as the solvent slowly evaporate or become trapped within the film. The polar functional groups of ethylene glycol work to separate excessive amounts of PSS from the film to form larger PEDOT:PSS grains surrounded by a smaller insulating PSS barrier would otherwise be seen in pristine films [88]. The small PSS barrier enables easier charge transport from one PEDOT:PSS grain to another. Similarly, DMSO, a very polar molecule, is able to separate the distance of the PEDOT from the PSS chain such that the PEDOT is able to form a more linear structure [90-92]. If too much DMSO or EG additive is added to the PEDOT:PSS ink, a decrease in conductivity is observed, which is attributed to the solvent additive remaining in the film and interfering with charge transfer. It should be noted that solvents are not as effective in enhancing the electrical conductivity compared to acids, likely due to the lower reactivity of solvents.

Post treatments are carried out by soaking films in a bath or heating film while drop coating various solvents onto the film. The most successful solvents used have been methanol, ethanol-water blend, and ethylene glycol [63, 65, 70]. The main mechanism behind the enhancement in electrical conductivity is the removal of or reorganization of excess insulating PSS species within the film to form better PEDOT percolating networks.

2.4.3 SILVER NANOWIRE TRANSPARENT ELECTRODES

Figure 2.14 illustrates the working principles of a silver nanowire electrode. Electrons can travel across the electrodes by moving through the nanowires and nanowire junctions. Light is able to transmit through the spaces between the nanowires making them visibly transparent. Dense nanowire networks result in higher conductivity and sparse

nanowire networks results in higher transparency, therefore an optimal nanowire density is needed to maximize both conductivity and transmittance. Thinner and longer nanowires result in the best transmittance and conductivity [64]. Longer nanowires facilitate higher conductivity because the electrons can travel longer distances before needing to switch to a new nanowire at a nanowire junction. Longer nanowires need for fewer nanowires and nanowire junctions to achieve high conductivity results in a higher transparency. Typical dimensions of commercially available silver nanowires are 100 nm in diameter and 20 microns long.

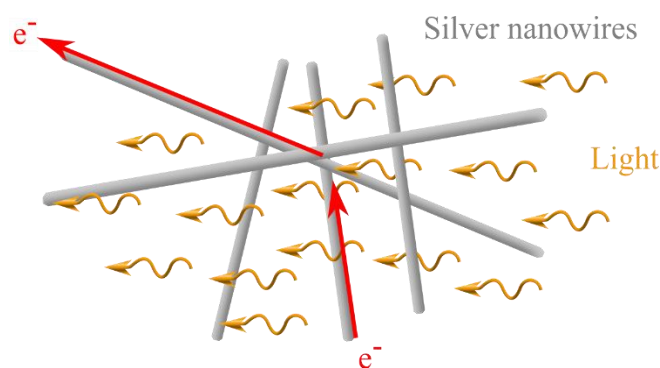


Figure 2.14. Operating principles of silver nanowire electrodes.

Silver nanowire electrodes can exhibit sharp peaks greater than 300 nm (places where three or more nanowires are stacked on top of one another). These sharp peaks typically result in short circuits for solar cells. In order to reduce these sharp peaks, various material coatings have been used to fill in the gaps between the nanowires, such as zinc oxide, aluminum doped zinc oxide, vanadium oxide, graphene oxide, and PEDOT:PSS. Another solution is to reduce the peak height by embedding the nanowires within a plastic substrate such as Poly(methyl methacrylate), and Polydimethylsiloxane.

Silver nanowires have been shown to fail when subject to electrical stress [73]. The proposed mechanism was due to Joule heating at the nanowire junctions [73] and

corrosion [93]. Joule heating occurs when excess heat is generated from the current flow through the nanowires. The resistance of individual nanowires is typically on the order of 180 - 320 Ω and the resistance of nanowire junctions is typically 1 - 10 $G\Omega$ [64, 94]. The extremely high resistance between the nanowire junctions can be reduced to 185 - 450 Ω by melting the junctions together or coating the junctions in conductive materials. The higher resistance at the nanowire junctions makes them more prone to Joule heating. If the heat generated at the nanowire junction is sufficient, the nanowires melt, coalesce, and break apart from one another. The broken nanowire junction exacerbates the problem as the current is redistributed over a fewer number of nanowire junctions, accelerating the failure.

Silver corrosion or tarnish is not typically due oxygen, but to sulfur compounds in the air [93]. Crystal defects within the silver nanowires are especially susceptible to corrosion because they are more reactive. Corrosion at crystal defects along the silver nanowire results in broken connections along the nanowire. Silver nanowire corrosion has been shown to not be dependent on relative humidity but on the environmental temperature [95]. This is because humidity does not affect the concentration of sulfur compounds in the air but higher temperatures can accelerate the corrosion process.

To improve the stability of silver nanowires various materials to encapsulate them have been used. In general metal oxide encapsulation such as TiO_2 and ZnO have been shown to improve thermal stability of the nanowire, enabling them to tolerate temperature beyond 200 $^{\circ}C$ with minimal consequence to their optical and electrical properties [96, 97]. Encapsulation in PEDOT:PSS has resulted in worse stability compared to non-encapsulated nanowires [95]. The fast degradation of silver

nanowire\ PEDOT:PSS has been attributed to the acidic nature of PEDOT:PSS, and the hygroscopic properties of PSS. The acidity of PEDOT:PSS could accelerate the corrosion of nanowires especially because both the PEDOT and PSS chains contain a sulfur ion; the main element responsible for silver corrosion. Excess PSS within the PEDOT:PSS film can absorb water and swell in size. The increase in the size of PSS destroys the conductive percolating pathways of the PEDOT chains and SNW embedded in a non-conductive PEDOT:PSS film may exacerbate the Joule heating problem.

2.5 SPRAY COATING

Figure 2.15 shows the setup of a Gravity fed Spray coater with gas pressure to aerosolize liquid and guide spray direction. This method works very well for both large and small volume productions, which can ease the transition from small scale laboratory research to large scale commercialization. Spray coating works well with solution viscosities ranging from 1 to 1000 cP [98]. Silver nanowires are typically dispersed in solvents with low boiling points and viscosities such as ethanol (78.4 °C and 1.07 cP) and isopropanol alcohol (82.6 °C and 2.96 cP) making spray coating more ideal compared to doctor blading, Meyer rod coating, or spin coating. Doctor blading and Meyer rod deposition leave excess solvents on the substrate surface, which can result in uneven silver nanowire distribution. The centrifugal force on the nanowires from spin coating results in poorly connected nanowire networks due to their unidirectional orientation. Spray coating allows for a controlled deposition rate so that the atomized solution can evaporate before hitting the substrate and form an even coating of randomly orientated nanowires. The random nanowire mesh is able to form a good network for electrical conductivity while maintaining sufficient gaps within the mesh for transparency. Gravity-

fed handheld spray coaters (Figure 2.15) are low cost and easy to set up in a laboratory, but introduces human error, which can result in unevenly sprayed films. Automated spray coating systems can increase repeatability, but are much more expensive to purchase and maintain than a gravity-fed, handheld spray coater.

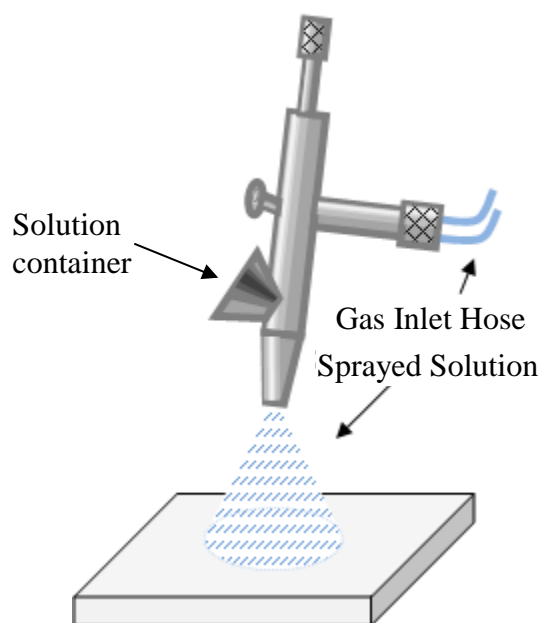


Figure 2.15. Setup of a gravity fed Spray coater with gas pressure to aerosolize solution and direct spray.

2.6 SPIN COATING

Figure 2.16 show the spin coating setup. A substrate with a liquid solution on top is held in place on a rotating platform by vacuum suction. As the substrate spins, a centrifugal force ($F_{Centrifuge}$) is created which removes excess solution from the substrate, leaving a thin and uniformly coated wet film behind. This film can be dried by evaporating in air, annealing, or spinning for a longer amount of time on the spin coater. Spin coating can be used to deposit films on the order of nanometers, is highly reproducible, and works with a wide range of solution viscosities. Spin coating is widely

used for depositing polymer and nanoparticle films [99, 100]. However, controversial reports have been made about successfully spin coating silver nanowire electrodes [95, 101], which brings this method into question. Another drawback of spin coating is its lack of scalability.

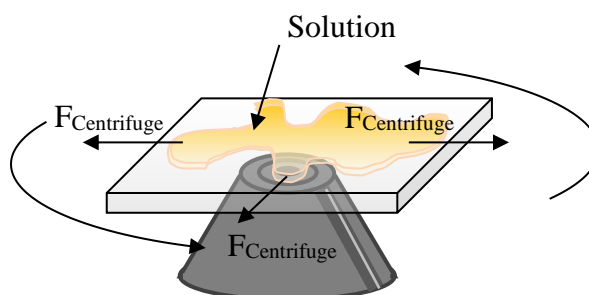


Figure 2.16. Spin coating setup

2.7 ULTRAVIOLET-VISIBLE SPECTROMETER

Figure 2.17 shows the schematic of an ultraviolet-visible spectrometer (UV-Vis). UV-Vis is used to measure the transmittance, reflectance, and absorbance of liquid, solid, or gas samples over the ultraviolet to deep infrared (190 - 2500 nm) light range. For transparent electrode applications, the transmittance should be greater than 80% [61]. The transmittance (T), absorbance (A), and reflectance (R) are given by equations 2.14, 2.15, and 2.16, respectively.

$$T = I_T/I_{0T} \quad (2.14)$$

$$A = -\log(T) \quad (2.15)$$

$$R = I_R/I_{0R} \quad (2.16)$$

Where I_T is the intensity of light transmitted through the sample, I_{0T} is the intensity of light transmitted with no sample or using a reference sample, I_R is the reflected light intensity from the sample, and I_{0R} is the reflected light intensity with no sample or using

a reference sample. Figure 2.17 has the light intensities I_T , I_{0T} , I_R , and I_{0R} correspondingly labeled. Light from the lamps inside the UV-Vis is sent to a monochromator which separates the light into a spread of individual wavelengths. This spread of light is radiated onto a small slit which only allows a very narrow range of monochromatic wavelengths to pass through. By rotating the monochromator, a different set of wavelengths are able to pass through the slit. In this way, the transmittance, absorbance, and reflectance for each wavelength can be tested on a sample. The only drawback to schematic shown in Figure 2.17 is the inability to measure light that reflects off the sample at any angle other than 0° and 180° . Silver nanowire films have been known to effectively scatter light and thus their direct transmittance (i.e. light that passes through the film without any change in direction) is around 17-20% lower than the total amount of light transmitted through the film [68]. A renovating sphere can be used to correct this problem, however, the results reported in this work do not make use of a renovating sphere.

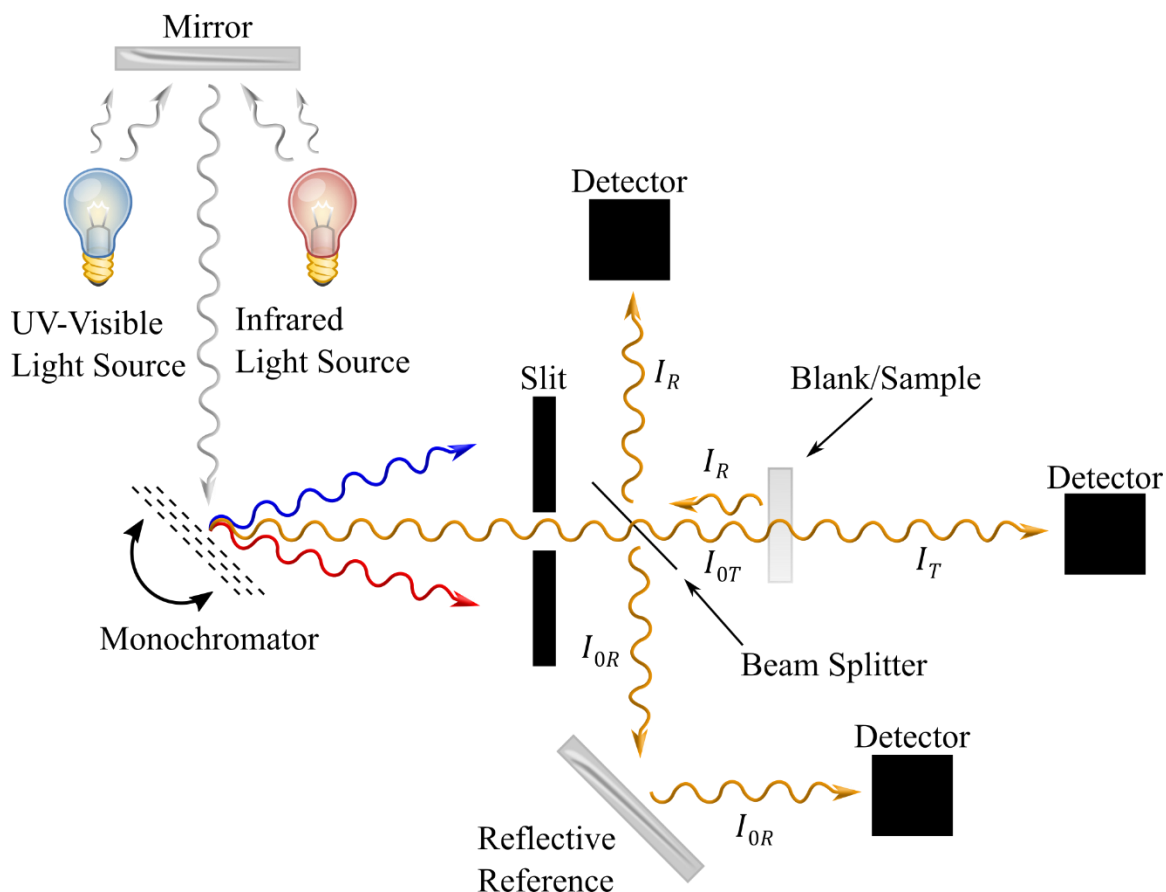


Figure 2.17. Schematic of an ultraviolet-visible spectrometer

2.8 FOUR-POINT PROBE

The four-point probe is used to measure the conductivity (σ), resistivity (ρ), and sheet resistance (R_{\square}) of thin films. σ and ρ are simply the inverse of one another and define how well or how difficult electrical current can flow through the material, respectively. The sheet resistance is the average resistivity over the sample's thickness. For transparent electrodes in solar cell applications, a sheet resistance less than $50 \Omega/\square$ is desired [102, 103]. Figure 2.18 shows (a) a four-point probe set up and (b) an electrical model for four-point probe setup. From Figure 2.18, current can flow through the two outside probes and the voltage drop is measured between the two inside probes. This unique set up allows for accurate sample measurement without the interference from the

probe-sample contact resistance (R_c) and wire resistance (R_w). The two outside probes use a current source to set the value of I regardless of R_c and R_w values, and the voltmeter has such a high internal resistance that R_c and R_w become negligible losses. If only two probes were used to measure sheet resistance, a volt source would have to be used, which would result in the voltage drop across R_w and R_c affecting the measurement.

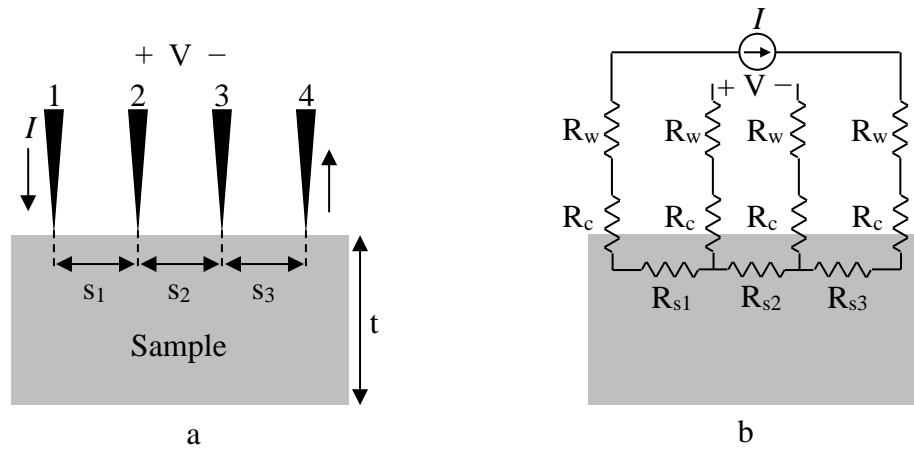


Figure 2.18. (a) Four-point probe set up and (b) electrical model for four-point probe setup.

The sheet resistance can be calculated by

$$R_{\square} = \frac{\rho}{t} \approx 4.552 \frac{V}{I} \quad (2.17)$$

where t is the thickness of the sample (Figure 2.18 a), V is the voltage across probes 2 and 3, and I is the current that passes through probes 1 and 4. The ρ/t can be approximated to $4.552 \times V/I$ only if the distance between the probes is equal ($s = s_1 = s_2 = s_3$) and that $t \leq s/2$. Four-point probe is not an ideal technique to use on a soft sample (such as PEDOT:PSS) because the sharp probes will likely puncture the sample and alter the measurement results.

2.9 TRANSFER LENGTH METHOD

The transfer length method can be used to measure sheet resistance, contact resistance (R_c), and specific contact resistivity (ρ_c) without threatening to damage soft samples. Figure 2.19 shows (a) experimental setup for the transfer length method and (b) distance vs resistance plot used to calculate R_{\square} , R_c , and ρ_c . The R_c is the resistance between the metal contact and the sample and can be found by dividing the value where the line in Figure 2.19 (b) crosses the y-axis by two. The metal contacts are typically deposited via thermal evaporation, printing or some other non-destructive deposition method. R_{\square} can be calculated by

$$R_{\square} = \text{slope} \times Z \quad (2.18)$$

where *slope* is the slope of the line in Figure 2.19 (b), and Z is the height of the contacts deposited on the sample. The ρ_c quantifies how well current can flow from the sample to the contact and is calculated by

$$\rho_c = L_T^2 R_{\square} \quad (2.19)$$

where L_T is the transfer length taken to be where line from Figure 2.19 (b) crosses the x-axis (should cross on the negative side of the access). The transfer length is the average distance an electron flows through the sample before being collected in the contact.

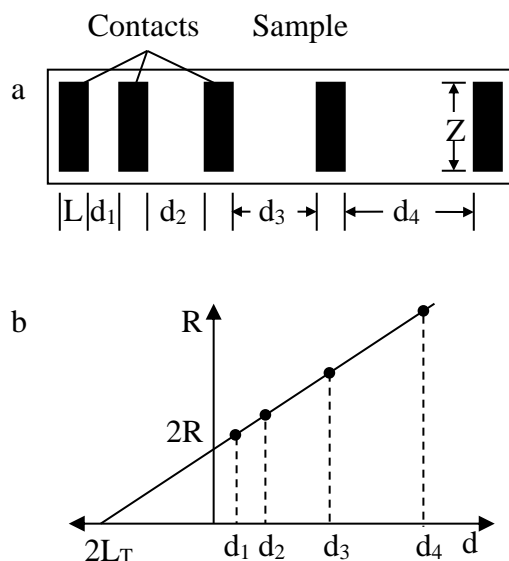


Figure 2.19. (a) Experimental setup for the transfer length method and (b) distance vs resistance plot used to calculate R_{\square} .

Figure 2.20 shows a modified version of the transfer length method where all the electrodes are evenly spaced apart. In order to create a plot like Figure 2.20 (b), contacts 1 or 5 must be used as a reference electrode. For example, the resistance between contacts 1 and 2, 1 and 3, 1 and 4, and 1 and 5 and would correspond to distances of d , $2d$, $3d$, and $4d$, respectively. The resistance between the contacts and their corresponding distances could be used to make a plot similar to Figure 2.20 (b). The distance between contacts 1 and 3 is taken to be $2d$ and not $2d + L$. This is because the electrons are assumed to flow through the contact 2 and that all contacts have negligible resistance. Thus the measured resistance value is predominantly the result of the spaces between each electrode. The main drawback of the transfer length method is that it assumes the sheet resistance to be uniform across the sample surface. One way to test this is to see if the points on distance vs resistance plot form a line. If the points do not exhibit a linear

relationship, then the sheet resistance may greatly vary across the sample and the transfer length method may not be an unsuitable technique.

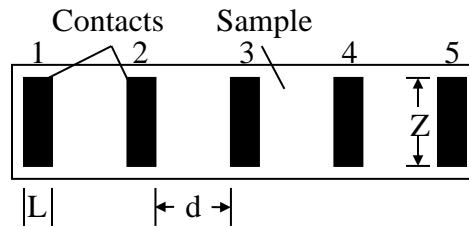


Figure 2.20. Modified version of the transfer length method where all the electrodes are evenly spaced apart.

2.10 SCANNING PROBE MICROSCOPY

Figure 2.21 shows the experimental set up for scanning probe microscopy. A cantilever is scanned over a sample in a raster fashion to gain micron and nano scale information. The piezoelectric crystals allow for extremely minute and precise control of the cantilever in the x , y and z directions. Depending on the type of cantilever and experimental setup, various sample properties can be measured such as: mechanical, electrical, surface roughness, friction, hardness, magnetic, chemical, work function, and thermal.

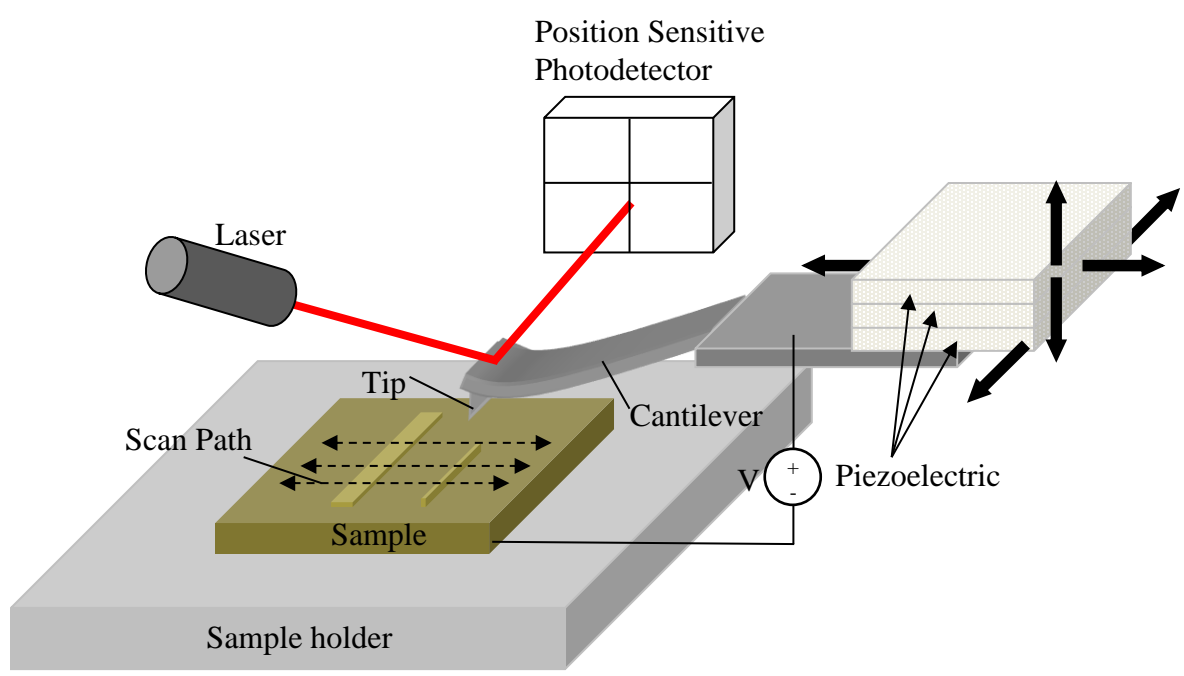


Figure 2.21. Experimental setup for scanning probe microscopy

2.10.1 ATOMIC FORCE MICROSCOPY

Atomic force microscopy is a scanning probe microscopy technique used to measure the surface topography. There various modes used to measure the topography: contact, tapping, and noncontact. Consistent with the name, atomic force microscopy uses atomic attractive and repulsive forces to measure the topography. Figure 2.22 shows the forces distance curve for atomic force microscopy as the tip is brought closer or further away from the sample. van der Waals forces repel the tip if it is brought very close to the sample and attract the tip towards if it is brought further away. The various modes for atomic force microscopy operate with specific regions of the force distance curve.

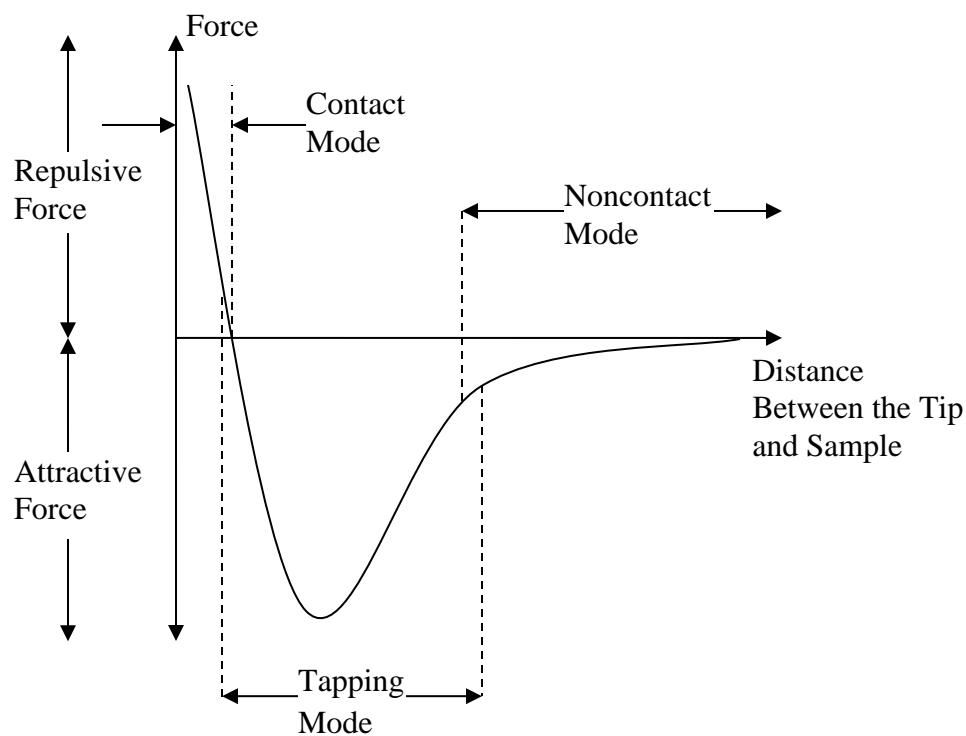


Figure 2.22. Force distance curve for atomic force microscopy

In contact mode the cantilever is brought in contact with the sample (i.e. the sample has a repulsive force acting on the tip). The tip is then dragged over the surface moving up and down with changes in morphology, which is directly translated from the laser reflecting off the cantilever to the position sensitive photodetector (Figure 2.21) into a 3-D image. The position sensitive photodetector is composed of four photodetectors. The variation of signal intensity from each photodetector provides a description of the laser's position. Contact mode can be performed so that the force between the tip and the sample remains constant or the height of the cantilever remains constant. To maintain a constant force, the piezoelectric controller adjusts the distance between the cantilever and the sample in real time based on the signal from the position sensitive diode. The piezoelectric adjustments are translated to topography. In constant height mode the cantilever is held at a constant height as it moves across the sample. The cantilever tip

will flex up and down with the surface morphology and be translated to topography. Contact mode works best for smooth hard samples and can provide the best image resolution. The cantilever can scratch and damage soft samples resulting in inaccurate morphological information. Rough sample run the risk of breaking the cantilever tip if the morphological change is high and sudden.

In Tapping mode, the piezoelectric controller oscillates the cantilever so that the tip and sample interaction oscillates between attractive and repulsive force regimes. In effect, the cantilever tip will lightly tap the samples surface. Noncontact mode will operate similarly with the exception that the cantilever tip will not touch the surface and operate only within the attractive force regime. In tapping and noncontact mode, the morphology, oscillation frequency, and oscillation amplitude are determined from the position sensitive photodetector. Tapping and noncontact mode are carried out using frequency modulation (FM) or amplitude modulation (AM). For FM, the frequency of the cantilever tip oscillations is held constant during the scan. The frequency of the cantilever is affected by the mechanical properties of the sample and can be used to discern different material types. FM has successfully been demonstrated to achieve atomic resolution. Changes in the tip amplitude can be used to gain topography information. Similarly, AM holds the amplitude of the cantilever constant. The peaks and valleys encountered by the tip will dampen or amplify the amplitude which is readjusted by the piezoelectric controller in real time and translated to topographical information. In practice, the most stable modulation is typically selected for imaging, which is influenced by the cantilever, sample, and imaging environment.

2.10.2 CURRENT SENSING ATOMIC FORCE MICROSCOPY

Current sensing atomic force microscopy is performed in contact mode and provides morphology, deflection, friction, and current flow mapping. Deflection is the difference in signal from the upper two photodetectors and lower two photodetectors on the position sensitive photodetector (Figure 2.21). Similarly, friction is the difference in signal from the right most two photodetectors and left most two photodetectors on the position sensitive photodetector (Figure 2.21). To map current flow, the cantilever (typically made from silicon) is coated with chromium and platinum to make it electrically conductive and a voltage potential is applied between the sample and the tip. Once the tip comes in contact with the sample, current can flow and be mapped out as the tip moves across the sample (typically on the order of 10^{-9} - 10^{-12} Ampere). The additional conductive coating on the cantilever makes the tip extra thick and reduces topography resolution. The conductive coating can wear off or become contaminated during scanning, which inhibits current mapping capabilities. To minimize tip contamination or degradation, the cantilever tip should touch the sample surface as lightly as possible.

2.11 SCANNING ELECTRON MICROSCOPE

Scanning electron microscope is used to magnify objects beyond typically optical microscope capability. The resolution of optical microscopes is limited due to the length of light waves in the visible region ranging from 450 – 750 nm. The scanning electron microscope uses electrons, which are much smaller than atoms and has achieved a resolution as low as 2.5 nm [104]. Because scanning electron microscopes use electrons to magnify samples, the images appear in black and white. Figure 2.23 shows scanning

electron microscope operating principles. An electron gun is used to generate electrons, which are then directed into a beam by the anode. The magnetic lens and scanning coils focus the electron beam onto the sample, which is scanned in a raster fashion. The back scattered detector detects and counts the number of electrons reflected off the sample. Electrons emitted from the sample are collected and counted by the secondary electron detector. The secondary electron detector provides topographical information based on the number of electron counts it receives. More electron counts correspond to a brighter spot on the image. The back scattered electron detector works in a similar manner but describes variation in material composition on the sample via lighter and darker spots. To prevent interference from air molecules, scanning electron microscope is performed in a vacuum. The sample being imaged must be conductive or have a conductive coating applied to prevent accumulation of charges from the electron beam, which would damage the sample before any useful information could be obtained.

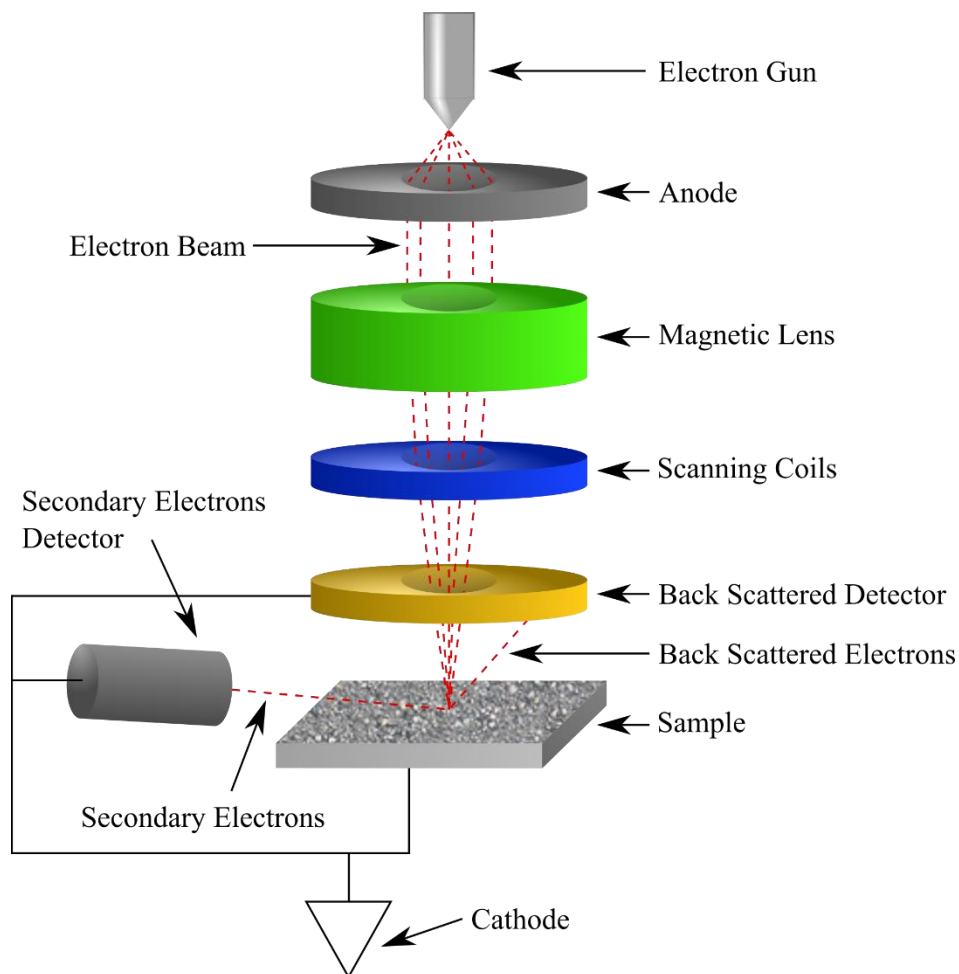


Figure 2.23. Scanning electron microscope operating principles.

2.12 ENERGY DISPERSIVE X-RAY SPECTROSCOPY

Energy dispersive X-ray spectroscopy (EDS) is an extension of the scanning probe microscopy and can be used to map out the elements present within the sample. EDS shines X-rays or high energy electrons onto the sample which are capable of ejecting core shell electrons. Figure 2.24 shows the (a) ejection of a core shell electron due to collision with a high energy electron beam and (b) emission of X-ray due to outer shell electron relaxing to the core shell. The electron composition for each element is

different, thus the energy of the emitted X-ray from the outer shell electron as it transitions to a lower energy state will correlate to that specific element.

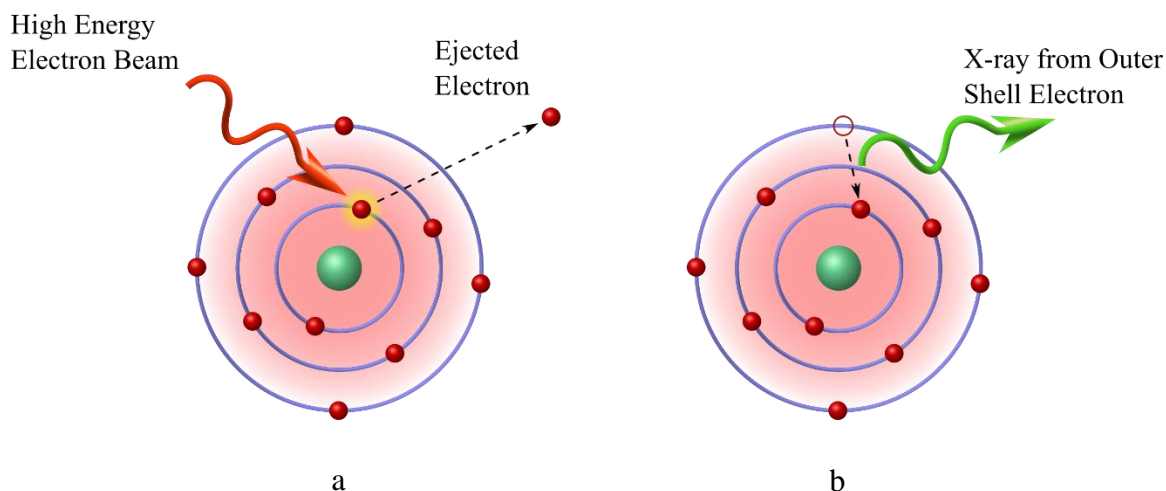


Figure 2.24. (a) Ejection of a core shell electron due to collision with a high energy electron beam and (b) emission of X-ray due to outer shell electron relaxing to the core shell.

2.13 X-RAY DIFFRACTION SPECTROSCOPY

X-Ray diffraction spectroscopy is used to determine the crystal phase composition, structure, orientation, unit cell lattice parameters, and crystallite size. Figure 2.25 illustrates the working principle of X-Ray diffraction spectroscopy. The incoming X-rays are reflected off the crystal lattice according to Bragg's law. The reflected X-rays participate in constructive or destructive interference, which enhances or mitigates the reflected signal intensity. The signal intensity is plotted with respect to the incident angle of the incoming X-ray. The slight variations in bonds within the crystal result in a signal that has a mean value and a variance distribution. The full width at half maximum (FWHM) of signal peaks show how crystalline the material is and the angles at which the peaks occur can be used to identify the crystal chemical composition. Unlike EDS, X-ray

diffraction spectroscopy does not eject core electrons from the atoms because the energy of the X-ray beam is lower than the X-rays (or electron beams) used in EDS.

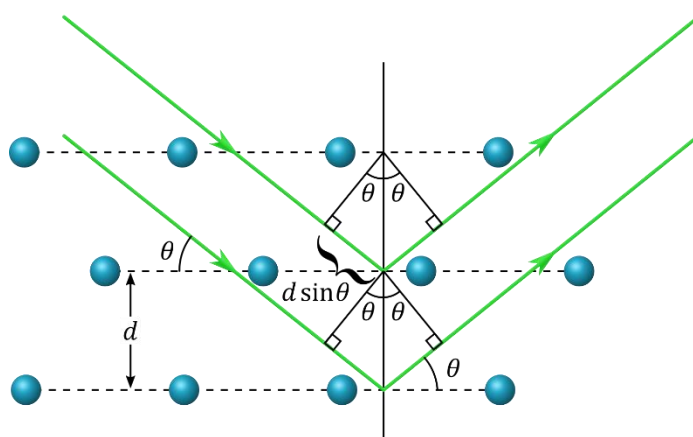


Figure 2.25. Working principle of X-Ray diffraction spectroscopy.

The conditions which reflected X-rays will maximize constructive interference (produce the highest signal intensity) is described by Bragg's Law

$$2d \sin \theta = n\lambda, \quad n = 0, 1, 2 \dots \quad (2.20)$$

where d is the distance between the planes reflecting the X-rays, θ is the angle of the incident and reflected X-rays, n is the order of interference, and λ is the wavelength of the incident X-ray. The Scherrer equation can be used to calculate the crystallite size within the sample and is given by

$$\tau = \frac{K\lambda}{\beta \cos \theta} \quad (2.21)$$

where τ is the mean crystallite size, K is the dimensionless shape factor (typically taken to be 1), λ is the X-ray wavelength, β is the width of the peak at half the maximum intensity, and θ is the angle at the maximum peak intensity (Bragg angle). The crystallites are microscopic crystals that make up a portions of a film. In the case of perovskite crystals, atomic force microscopy may detect small particles on the order of

nm on a film surface but these particles can be composed of crystallites on the order of hundreds of angstroms as detected by XRD. Perovskites used in solar cells typically undergo constructive interference at 14.1° and 28.5° , and 43.2° which corresponds to the (110), (220), and (330) planes within the crystal [105].

2.14 RAMAN SPECTRSCOPY

Raman spectroscopy uses the Raman effect to identify the types of chemical bonds within a sample. The Raman effect is the shift in energy which occurs between light that is radiated on a material and the light that is reflected off the material. The shift in energy is caused by the light interacting with the vibrational modes of the molecular bonds. Figure 2.26 shows the vibrational modes for a water molecule. The bonds between the oxygen and hydrogen molecules have various degrees of freedom in which they can oscillate. Light (typically a laser in the case of Raman) is absorbed by interacting with these oscillations and is remitted at a particular energy in relation to bonds resonate frequencies. These signals are then collected, translated into wavenumber ($\Delta\omega$), and plotted based on their signal intensity.

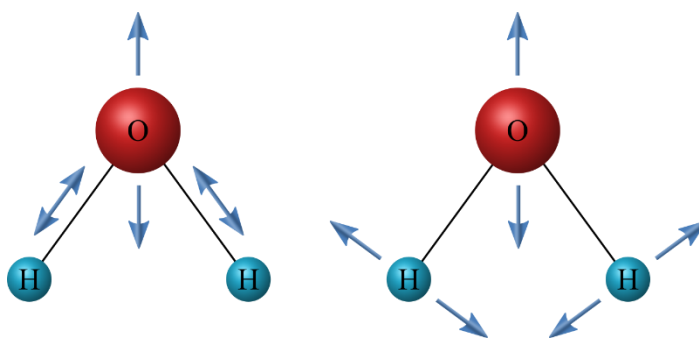


Figure 2.26. Vibrational modes for a water molecule

The wavenumber can be calculated by

$$\Delta\omega = \left(\frac{1}{\lambda_0} - \frac{1}{\lambda_1} \right) \frac{10^7(nm)}{1(cm)} \quad (2.22)$$

where λ_0 is the wavelength of monochromatic light source (i.e. laser) with units of nm, and λ_1 is the wavelength of the remitted light form the sample with units of nm. $\Delta\omega$ is typically expressed in terms of cm^{-1} . The intensity of the signal typically corresponds to number of bonds present in the sample. The slight variations in vibrations from molecule to molecule result in a signal that has a mean value and a variance distribution. The size of the FWHM of the signal peaks relays how crystalline the material is (the smaller the FWHM the more crystalline the material).

In the case of PEDOT the benzoid and quinoid structure exhibit a small shift in the Raman peak wavenumber due to the change in the $C_\alpha = C_\beta$ bond on the thiophene [83, 106]. The quinoid structure can also result in a smaller FWHM due to a more ordered film.

CHAPTER 3 EXPERIMENTAL PROCEDURES

3.1 FABRICATION AND CHARACTERIZATION OF PEDOT:PSS TRANSPARENT ELECTRODES

3.1.1 GLASS SLIDE CLEANING AND PREPARATION

Precut 1.5 cm by 1.5 cm by 2 mm glass substrates were obtained from Hartford Glass Company. Substrates were blown with pressurized N₂ gas (30 PSI) to remove large debris, wiped with Kim Wipe tissues (Fisherbrand 07301005) to remove excess grease or finger prints, and blown again to remove any fibers from the Kim Wipe tissues.

Substrates were then ultrasonicated for 20 minutes in soapy deionized (DI) water, pure DI water, acetone, and lastly propan-2-ol. The glass slides were stored in IPA prior to future use.

Prior to use, glass slides were blow dried with pressurized N₂ gas and plasma cleaned for 20 minutes. Figure 3.1 shows the plasma cleaning set up with a BOC Edwards XDS5 vacuum pump on the right and a PDC-32G plasma cleaner on the left. The vacuum pump was allowed to run for 5 minutes, then oxygen gas was slowly added to the chamber for 10 seconds, such that the position of the glass substrates was not disturbed due to the pressure change. The plasma cleaner was turned on and set to a medium power level. Every five minutes, oxygen gas was added to the chamber for 10 seconds. After 20 minutes, the power was turned off, the plasma cleaner and vacuum pump were turned off, and the chamber was slowly aired. Glass substrates were kept in a petri dish for immediate use.



Figure 3.1. Photograph of plasma cleaning set up with a BOC Edwards XDS5 vacuum pump on the right and a PDC-32G plasma cleaner on the left.

3.1.2 FABRICATION OF PEDOT:PSS TRANSPARENT ELECTRODES

Poly(3,4-ethylenedioxythiophene):polystyrene sulfonate (PEDOT:PSS) was obtained from Heraeus (PH1000). Ethylene glycol (EG), dimethyl sulfoxide (DMSO), and blends thereof (1:1, 2:1, and 1:2) were used as solvent additives to the PEDOT:PSS in 5, 10 and 15 wt. %. Films were spin coated at 4000 RPM with an acceleration of 2000 RPM/s for 60 seconds using a WS-650B-23NPP/LITE spin coater depicted in Figure 3.2. The spin coater was fed with pressurized gas at 50 PSI to regulate spin speed and connected to Fisher Scientific MaximaDry pump to create a suction on the glass substrate during the spin coating process. After spin coating, films were allowed to air dry (approximately 5 - 15 minutes) and annealed at 120 °C for 10 minutes.



Figure 3.2. Photograph of spin coater.

Post treatments were carried out by soaking PEDOT:PSS films in water, ethylene glycol, DMSO, ethanol, and different equimolar blend combinations of these solvents for 2 minutes. The solvents and solvent blends were poured in a petri dish where the PEDOT:PSS films were placed to soak. Following the soaking the PEDOT:PSS films were submerged in DI water for 20 seconds and annealed at 120 °C for 10 minutes.

3.1.3 THICKNESS MEASUREMENTS OF PEDOT:PSS TRANSPARENT ELECTRODES

Figure 3.3 show a photograph of the Veeco Dektak 150 used to measure film thickness. Operation procedures for the Dektak can be found in the user's guide manual located on the computer desktop entitled "Dektak Documentation." The Dektak was set to measure both hills and valleys, used a force of 1 to 5 mN, 30 to 60 second time duration of scans, and a 5 μm thickness resolution using Dektak software. A standardized sample (Veeco 301-031-44nm) of 46.4 nm height was used to calibrate the Dektak and

find optimal settings before each use. The “Level the Trace at the Current R and M Cursor Intercepts” tool was used to flatten data that was plotted with a slope.



Figure 3.3. Photograph of Veeco Dektak 150 used to measure film thickness.

3.1.4 SHEET RESISTANCE OF PEDOT:PSS TRANSPARENT ELECTRODES

Sheet resistance for PEDOT:PSS electrodes was measured using the transfer length method. The bottom portion of the PEDOT:PSS electrode was etched away using a cotton applicator dipped in DI water. Figure 3.4 shows the (a) mask using during the silver contact deposition and a sample with silver contacts and (b) the thermal evaporation system inside the glove used to deposit the silver contacts. Operating procedures can be found in the glovebox manual found in South Dakota State University Daktronics Engineering hall room 058 [107]. Silver contact were 100 nm thick under 10^{-5} mbar base pressure. The rate of deposition was linearly increased starting at 0.1 \AA/s and reaching 0.3 \AA/s after 8 nm had been deposited, 0.5 \AA/s after 15 nm had been deposited, 1 \AA/s after 30 nm had been deposited, and 1.5 \AA/s after 50 nm had been deposited. The

rate of 1.5 \AA/s was held constant until 100 nm of silver had been deposited. After the deposition was complete, the thermal evaporation was stopped, but the chamber was held under vacuum until the vacuum pressure dropped to 10^{-5} mbar. Once the pressure had dropped, the turbo pump was allowed to spin down, and the chamber was aired.

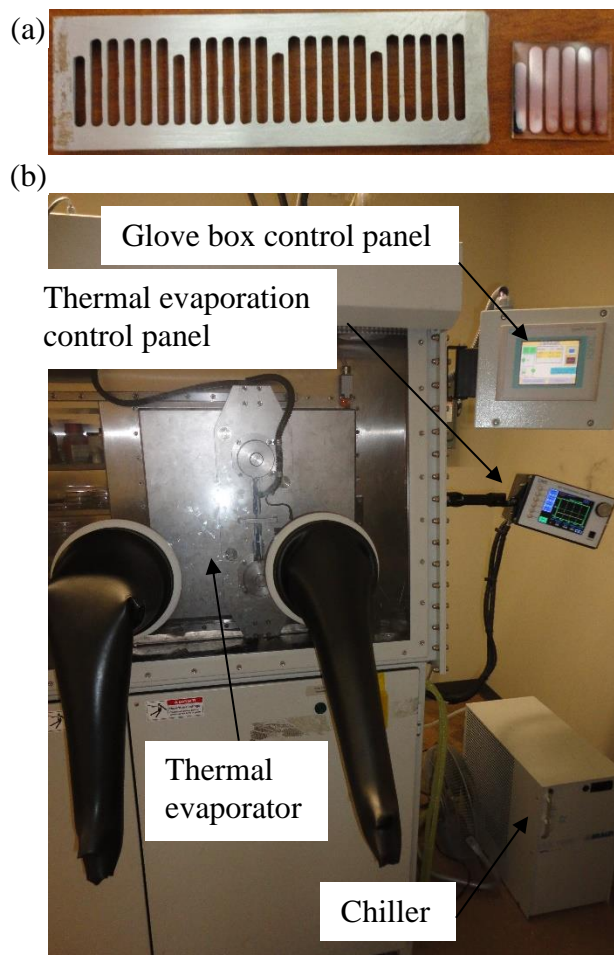


Figure 3.4. Photographs of (a) mask using during the silver contact deposition and a sample with silver contacts and (b) the thermal evaporation system inside the glove used to deposit the silver contacts.

Figure 3.5 shows the Keithley 2400 used to measure the resistance between the electrodes with an inset of a sample to be measurement. The clips were moved along the

pins on the 3M clip to measure the resistance between different electrodes. The resistance and distance between the electrodes were recorded in Excel 2016 and used to calculate the sheet resistance.

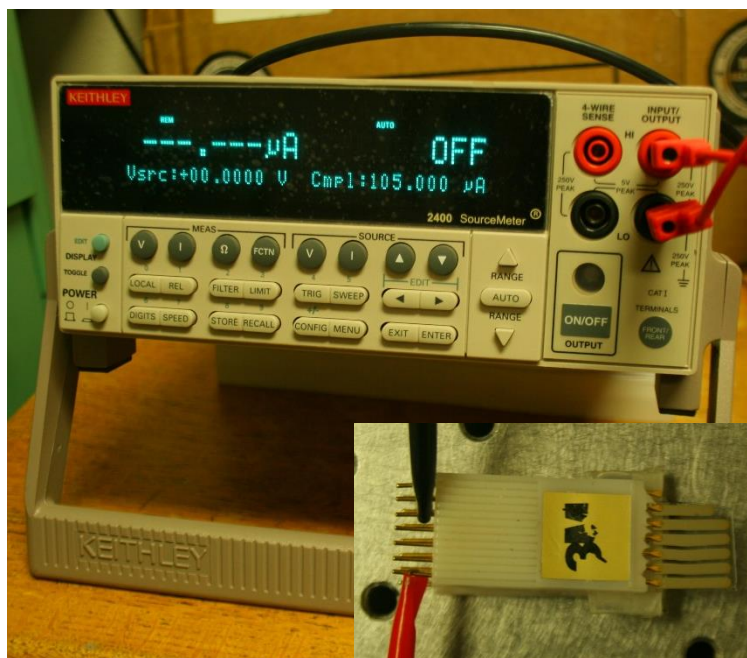


Figure 3.5. Photograph of Keithley 2400 used to measure the resistance between the electrodes with an inset of a sample to be measurement.

The distance between the electrodes was measured using a Hitachi S-3400N scanning electron microscopy (SEM) (Figure 3.6). The operating procedures for the SEM and Quarts PCI image processing software can be found in the user's guide Manual located next to the SEM system [108]. The SEM was operated using a probe current of 30 – 50 %, saturation current of 130 – 150 μA , and accelerated voltage of 10 - 25 kV. All images were taken with a 10 mm working distance between the sample and backscattered detector. SEM images were exported, analyzed, and saved in JPEG format using Quarts PCI software.



Figure 3.6. Photograph of Hitachi S-3400N system used for SEM imaging and EDX measurements.

3.1.5 OPTICAL PHOTOGRAPHS OF PEDOT:PSS ELECTRODES

Optical photographs of PEDOT:PSS electrodes were taken using a Canon EOS 400D digital single-lens reflex (DSLR) camera using an EFS 18 - 55 mm lens. The camera was set to manual mode with an ISO of 100 - 400. The aperture, shutter speed, and lens focusing were adjusted before each shot to best accommodate the lighting conditions and camera position with respect to the PEDOT:PSS electrodes. The operating manual for the Canon EOS 400D can be found online [109].

3.1.6 TOPOGRAPHY OF PEDOT:PSS TRANSPARENT ELECTRODES

Figure 3.7 shows the Agilent 5500 scanning probe microscope (SPM) used to take topography and current sensing AFM (CS-AFM) images. Operating instructions for the AFM can be found online [110]. The 5500 SPM was controlled through Pecoview software on the desktop computer. Images taken in AM tapping mode were performed in

air under normal atmospheric conditions and produced topographical, amplitude, and phase images. A 75 kHz SSS-SEIH-SPL or HiRes-C14/Cr-Au-5 tips from NanoSensors were used to scan across a 2 by 2 μm size area on the samples. All settings were left at the default setting except the I and P gain, which were given a value ranging from 8 to 10. Images were processed in Gwyddion SPM imaging software. User manuals on how to operate the software can be found at Gwyddion's website [111]. The following tools were used to edit AFM images: "Level data by mean plain subtraction," "Correct lines by matching median heights," and "Shift minimum data value to zero." The color range was adjusted by selecting "stretch color range to part of the data" and selecting "explicitly set fixed color range." The base color which represented 0 nm was set as the minimum and the maximum was adjusted to best enhance the features within the image. The color of the images was selected to be "Gold" by right clicking on the color bar.

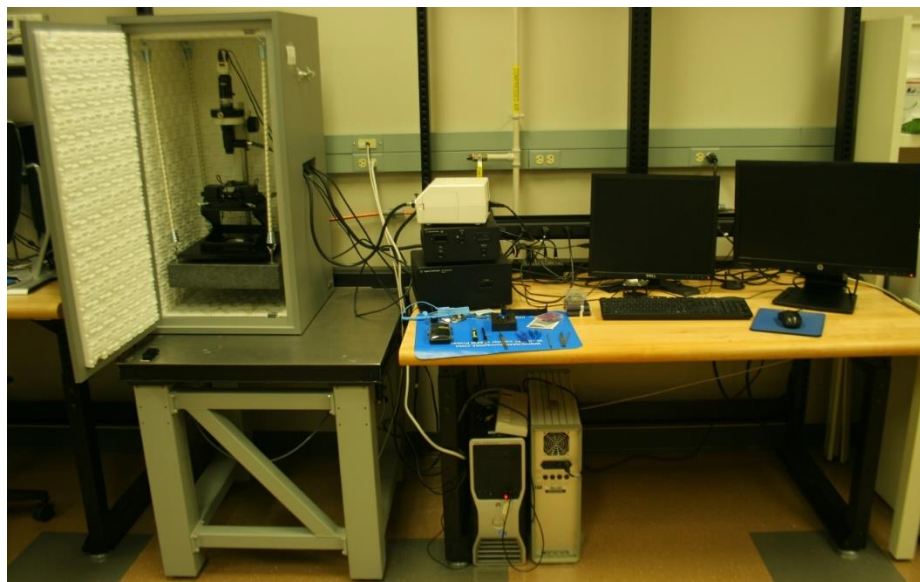


Figure 3.7. Photograph of Agilent 5500 scanning probe microscope (SPM) used to take topography and current sensing AFM (CS-AFM) images.

3.1.7 CURRENT SENSING ATOMIC FORCE MICROSCOPY OF PEDOT:PSS ELECTRODES

CS-AFM was performed in contact mode using the Agilent 5500 system shown in Figure 3.7. A Pt/Ir coated silicon tip (Budget Sensors ContE-G) with radius of 20 nm, force constant of 0.2 N/m, and resonance frequency of 14 kHz was used for imaging. The deflection of the laser was adjusted to $-1.00 \text{ V} \pm 0.02 \text{ V}$. The tip was lowered at a rate of $0.3 \mu\text{m/s}$ until it came in contact with the sample. Once in contact with the sample, the set point was raised such that the tip lost contact with the sample, and then slowly lowered again until the tip lightly touched the sample. Performing a “soft touch” by using the set point removes excess friction between tip and sample. Without the soft touch, the Pt/Ir coating quickly rubs off and the silicon tip loses its ability to conduct current. Prior to imaging, I-V curves were generated in Pecoview software by selecting spectroscopy under the controls tab and choosing current vs. sample bias. I-V curves were used to insure an ohmic contact existed between the tip and the sample. Measurements were taken under a 0.1 - 0.3 V bias placed on the Pt/Ir coated tip. CS-AFM Images were viewed and cropped using Gwyddion software with no other modification and topography images were processed as described in section 3.1.6.

3.1.8 TRANSMITTANCE OF PEDOT:PSS TRANSPARENT ELECTRODES

Figure 3.8 shows the transmittance measurement set up using the Agilent 8353 UV-Visible spectrophotometer (UV-Vis). The UV-Vis utilizes a tungsten and hydrogen lamp generate a light spectrum ranging from UV to infrared (300 nm – 1100 nm). The Chemstation software was used to control the UV-Vis through a desktop interface. Operation instructions for the UV-Vis and Chemstation can be found in the user’s manual

located in Daktronics engineering 056 [112]. Air was used as a reference for all samples. Samples were placed on a foam platform in front of the liquid sample holder. All data was exported in .CSV format and later analyzed in Microsoft Excel 2007 - 2016.

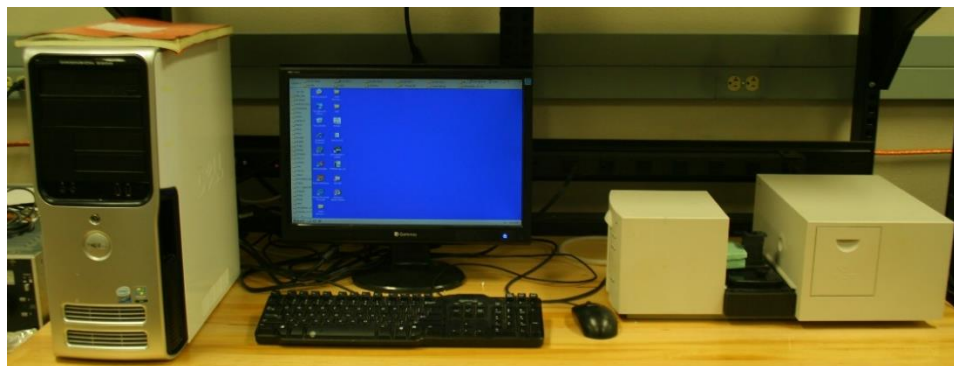


Figure 3.8. Photograph of Agilent 8353 UV-Visible spectrophotometer for transmission spectroscopy.

3.1.9 RAMAN SPECTROSCOPY OF PEDOT:PSS ELECTRODES

Figure 3.9 shows the LabRam HR800 system used for Raman spectroscopy. Raman spectroscopy was performed using an Argon laser with a wavelength of 514.5 nm, a 300 nm grating, D3 filter, and 60 second detector integration time. Operating procedures for the LabRam HR800 can be found in the standard operation procedures (SOP) next to the system [113]. Optical images of each site measured were saved along with the Raman data that was exported in .TXT format. The Raman data was later plotted and analyzed in Microsoft Excel 2007 – 2016.



Figure 3.9. Photograph of LabRam HR800 system used for Raman spectroscopy.

3.1.10 FABRICATION OF ITO FREE PEROVSKITE SOLAR CELLS

Figure 3.10 shows the device structure of the perovskite solar cell. PEDOT:PSS (Clevios PH1000) with 15 wt. % DMSO:EG 1:1 was blended with IPA 2:1 v/v to improve wetting. The PEDOT:PSS ink was then spin coated at 2000 RPM with an acceleration of 2000 RPM/s for 45 seconds. The films were allowed to air dry for 15 minutes before annealing at 120 °C for 10 minutes. After annealing, the films were soaked in water:EG:ethanol 1:1:1 volume ratio for two minutes followed by submersion in DI water for 20 seconds and annealing at 120 °C for 10 minutes. Additional layers were spin coated following the same procedures as the first layer except the spin speed was increased to 4500 RPM. A cotton applicator dipped in water was used to wipe off the bottom portion of the PEDOT:PSS electrode (Figure 3.11). Silver past (PELCO colloidal silver 16031) was applied to the left most edge to serve as a contact on the anode and prevent successive layers of the device from coating that area. Patterned ITO substrates were cleaned according to procedures outlined in section 3.1.1 and used as reference electrode. PEDOT:PSS (Clevios 4083) blended with IPA 2:1 v/v was spin coated at 4500

RPM with 4000 RPM/s acceleration for 45 seconds onto the patterned PEDOT:PSS (PH1000) or ITO electrode and annealed at 120 °C for 10 minutes. The mixed halide perovskite solution was made by mixing 581 mg of lead iodide (PbI₂), 225 mg of Methylammonium iodide (CH₃NH₃I), and 39 mg of lead chloride (PbCl₂) in 1 ml of γ -butyrolactone blended with DMSO (7:3 v/v) inside a N₂ filled glove box. The perovskite solution was stirred at 1150 RPM at 70 °C for at least 2 hours before use. The perovskite solution was spin coated inside a N₂ filled glove box at 750 RPM (750 RPM/s) for 20 seconds which was then ramped up to 4000 PRM (4000 RPM/s) for the remaining 60 seconds (Figure 3.12 depicts the spin coater used inside the glove box). Half way into the spin coating the perovskite layer, 160 μ l of toluene was drop coated onto the film to remove the DMSO solvent. [6,6]-phenyl C₆₁-butyric acid methyl ester (PC₆₀BM) was mixed in chlorobenzene solution (20 mg/ml) and stirred at 1150 RPM on 70 °C heated surface for at least 2 hours before use. The PC₆₀BM solution was spin coated on top of the perovskite layer at 2000 RPM (2000 RPM/s) for 40 seconds. Rhodamine powder (company and model number) was mixed in IPA to form a 0.5 mg/ml solution. The Rhodamine solution was spin coated on top of the PC₆₀BM layer at 4000 RPM (4000 RPM/s) for 40 seconds. The top silver electrodes were thermally evaporated according to the procedures outlined in section 3.1.4.

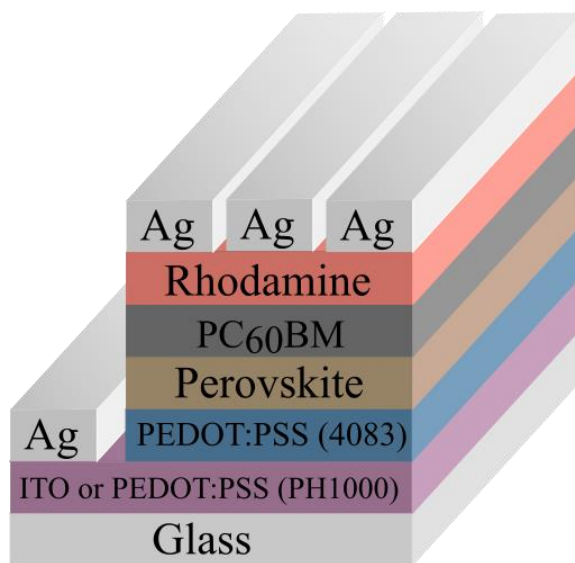


Figure 3.10. Device structure of the perovskite solar cell.

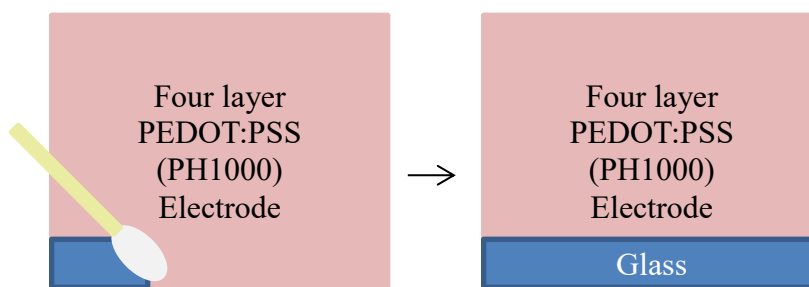


Figure 3.11. Etching PEDOT:PSS with cotton applicator.



Figure 3.12. Photograph of spin coater used inside glove box to deposit perovskite, PC₆₀BM, and Rhodamine films.

3.1.11 X-RAY DIFFRACTION SPECTROMETER OF PEDOT:PSS ELECTRODES

Figure 3.13 shows the Rigaku Smartlab system used to obtain X-Ray Diffraction (XRD) spectrum. The XRD measurement were carried out at 2.2 kW power using a Cu-K α (1.54 Å) radiation. Operating procedures can be found in the SOP for the XRD located in Daktronics Engineering Hall 056 [114]. XRD data was viewed in PDXL Software and edited, if necessary, using “Hide BG” before the data was copied, pasted, and saved into a Microsoft Excel 2016 spread sheet for future analysis. The “Hide BG” feature subtracts out any background noise in the form of long broad humps that distracts from the sharp peaks observed in the spectrum. The average crystallite domain size was automatically calculated by PDXL software using the Scherrer equation (see chapter 2 section 2.13 for more details).



Figure 3.13. Photograph of Rigaku Smartlab system used to obtain X-Ray Diffraction (XRD) spectrum.

3.1.12 I-V CHARACTERIZATION OF PEROVSKITE SOLAR CELLS

Figure 3.14 shows the experimental set up using (a) Agilent 4155C semiconductor parameter analyzer and (b) Xenon arc lamp (Newport 67005) for I-V characterization.

The Newport 69911 power supply (Figure 3.15) was turned on and used to set Xenon arc lamp power to 300 W. The Xenon arc lamp was turned on and allowed to stabilize for 30 minutes. The Agilent 4155C was turned on. Once booted up, the entire rows for V1 and V2 variables were deleted from the VNAME column, after pressing “next” the sweep mode was set to “double,” a start and stop voltage set to 0 - 1 V, and a hold time of 0.5 seconds. To view the I-V plot area the “graph/List” button was pressed. To begin the I-V measurement the scan rate “short” was pressed (scans at a rate of 0.01V per 0.01

seconds) followed by the “single” button to take a single measurement. To save the data, the “graph/List” was pressed again to view the raw data, followed by “spread sheet.” A name for the I-V data was typed followed by pressing “Execute” to save the data to a floppy disk. The floppy disk was then transferred to a PC where all the data was placed in Excel 2007 - 2016 spread sheets for future analysis. In Excel the data was plotted onto I-V curves and I_{sc} , V_{oc} , FF , R_s , R_{sh} , and η were calculated (see chapter 2 section 2.1 and 2.2 for details).

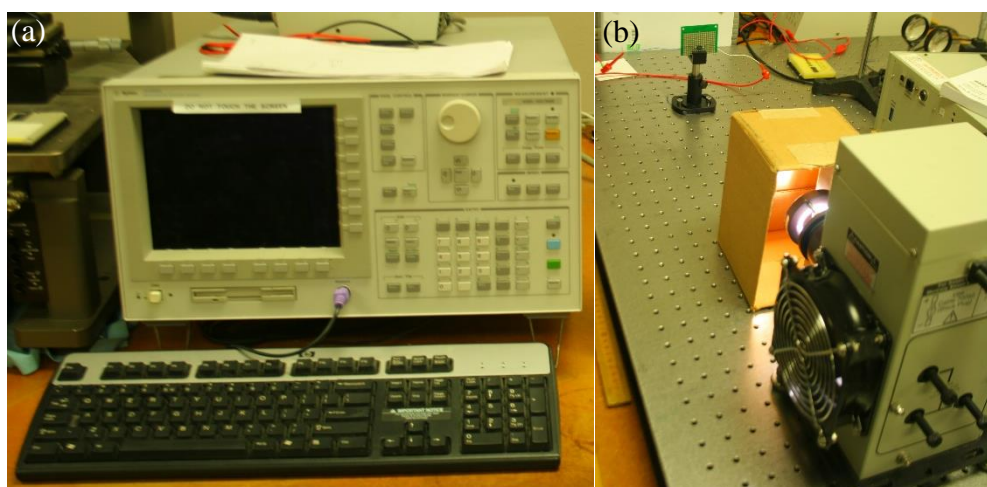


Figure 3.14. Photograph of experimental set up using (a) Agilent 4155C semiconductor parameter analyzer and (b) Xenon arc lamp (Newport 67005) for I-V characterization.



Figure 3.15. Photograph of Newport 69911 power supply used to power the Xenon Arc lamp.

3.1.13 TRANSIENT PHOTOCURRENT MEASUREMENT OF PEDOT:PSS ELECTRODES

Figure 3.16 shows the experimental set up for transient photocurrent measurement. A Nitrogen Laser (Photon Technologies international GL-3300) coupled with a Dye laser (Photon Technologies international GL-301) was shined onto the solar cell which generated a small photocurrent which decayed with time. The photocurrent signal was detected by an oscilloscope (Agilent Technologies MSO-X-4154A mixed oscilloscope) with a small resistance of $50\ \Omega$ to simulate short circuit conditions. The data was saved onto a USB flash drive, transferred to a PC, and plotted in Excel 2007-2016. Origin software was used to fit the decay curve with a mono-exponential function. The data was plotted in Origin and highlighted and from the pull down menu Analysis\fittings\fit exponential “open dialogue” was selected. Under the settings tab from the popup menu “ExpDac1” was selected and under the code tab “Ok” was selected. In the plot window the value shown for t_1 in the table was taken to be the charge transport time.

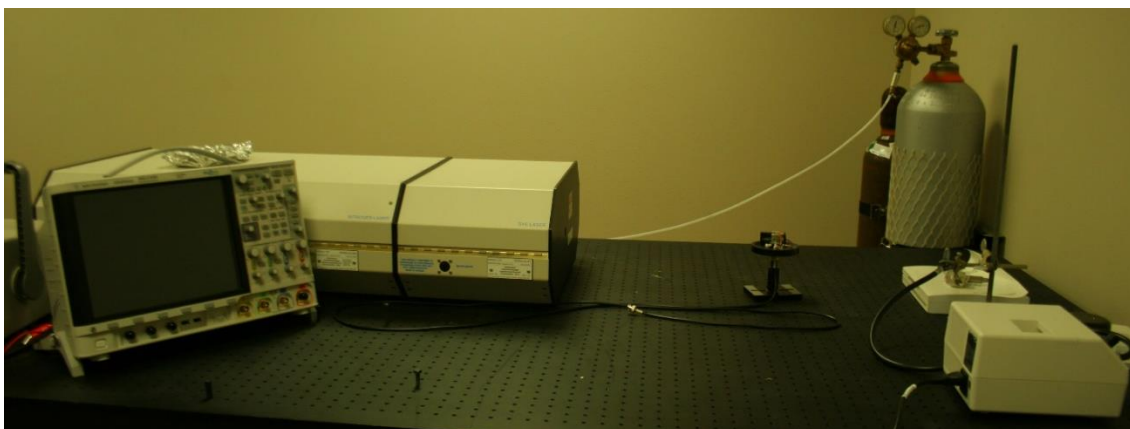


Figure 3.16. Photograph of experimental setup for transient photocurrent measurement.

3.2 SILVER NANOWIRE TRANSPARENT ELECTRODES FABRICATION AND CHARACTERIZATION

3.2.1 SILVER NANOWIRE SYNTHESIS AND SOLUTION PREPARATION

Figure 3.17 shows a dry run setup for silver nanowire synthesis. In a 20 ml vial, 0.5 grams of silver nitrate (Fisher Scientific CAS 7761-88-8) was dissolved in 6 ml of ethylene glycol (Arcos CAS 107-21-1). A 25 mM solution of CuCl_2 (Fisher Scientific CAS 7447-39-4) in ethylene glycol was made. Prior to use, glassware was cleaned with scrubbed with soap and water and rinsed with water. The two necked round bottom flask (100 ml or 250 ml) was cleaned by ultrasonciating for 20 minutes each in soapy DI water, DI water, acetone, and IPA and dried with pressurized N_2 gas (30 PSI) before use. Vegetable oil was poured into the glass trough for the oil bath and placed on the hotplate (Corning PC-420D). In the two necked round bottom flask, 0.3 grams of Polyvinylpyrrolidone (PVP) (Sigma-Aldrich CAS 9003-39-8) was dissolved in 24 ml of ethylene glycol, placed in the oil bath, which was heated to 141 °C, 145 °C, 151 °C, or 160 °C and stirred at 280 RPM. The temperature of the PVP solution was controlled using a Corning Temperature Controller (Cat#6795PR). Once the temperature was stable, 40 μl of the CuCl_2 solution was added to the PVP solution and allowed to mix for 1 minute. The AgNO_3 solution was ultrasonicated for 4 minutes until it became a translucent pale amber color. The AgNO_3 solution was added drop by drop for 8 to 9 minutes. The solution was added at a slower rate towards the beginning ($\sim 5 \mu\text{l}/\text{second}$) and faster after 3 minutes ($10 \mu\text{l}/\text{second}$) towards the end of the reaction $100 \mu\text{l}/\text{second}$ (7 to 8 minutes). The reaction was then sealed with a glass plug until shimmering swirls

became visible within the reaction; indicating the silver nanowires had formed. The reaction was then cooled and stored in 20 ml glass vials until they were cleaned.

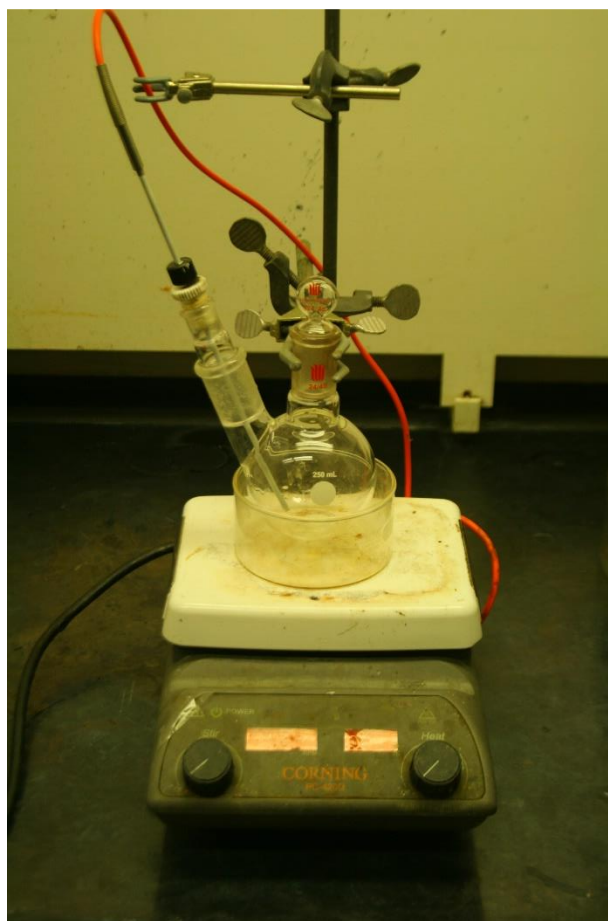


Figure 3.17. Photograph of dry run setup for silver nanowire synthesis.

Silver nanowires were cleaned by centrifuging (Figure 4.18) a dilute silver nanowire solution with acetone (1:2) at 2000 RPM for 20 minutes. The supernatant was discarded and the silver nanowires were dispersed in DI water. This process was repeated three more times with DI water, after which the nanowires were finally dispersed in IPA. The concentration of the silver nanowire solution was determined by placing 1 ml of solution in the centrifuge at 6000 RPM for 5 minutes, discarding the supernatant, drying out the nanowires, and weighing the centrifuge vial with the dry silver nanowires inside.

The original weight of the vial was subtracted from its weight with the nanowires.

Typical concentrations were around 5 - 10 mg/ml.



Figure 3.18. Photograph of Eppendorf Centrifuge 5424 used to clean silver nanowires.

3.2.2 SILVER NANOWIRE TRANSPARENT ELECTRODE FABRICATION

Figure 4.19 shows the (a) mater airbrush G255-SET and (b) unbranded airbrush with 7cc fluid cup used to spray coat spray silver nanowires. Both spray coaters were connected to a hoses via nipple fitting and the hose was attached to a gas cylinder with pressure regulator via nipple fitting (Figure 3.20). The gas pressure was set to 25 PSI. Silver nanowire solution was diluted to 1.5 - 0.23 mg/ml and 0.5 ml was sprayed onto a glass substrate (prepared according to section 3.1.1) heated to 140 °C, which took approximately 1 to 2 minutes. The glass substrate was taped down to a ceramic plate to prevent it from blowing away during the spray coating process. Silver nanowire electrodes were annealed at 140 - 200 °C for 30 minutes to achieve sheet resistances

below $50 \Omega/\square$. UV-ozone treatment was performed for one minute using a Novascan PSD-PROUV4T UV-ozone system.

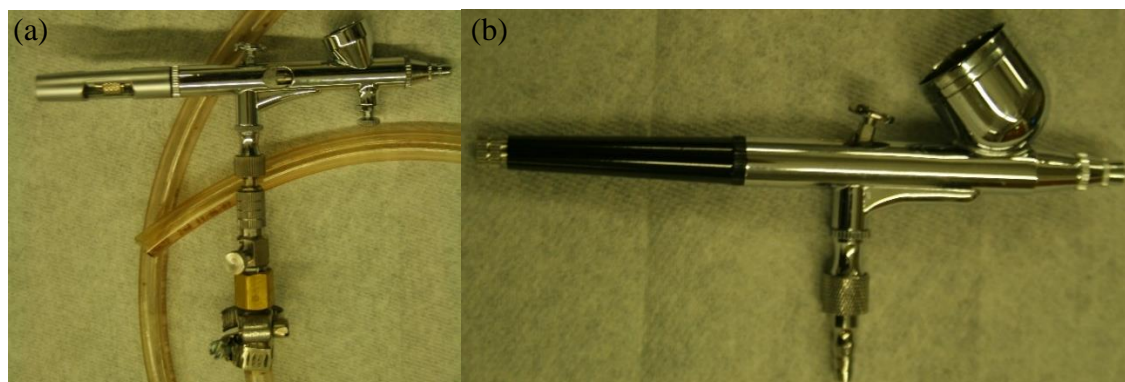


Figure 3.19. Photograph of (a) Mater airbrush G255-SET and (b) unbranded airbrush with 7cc fluid cup used to spray coat spray silver nanowires.

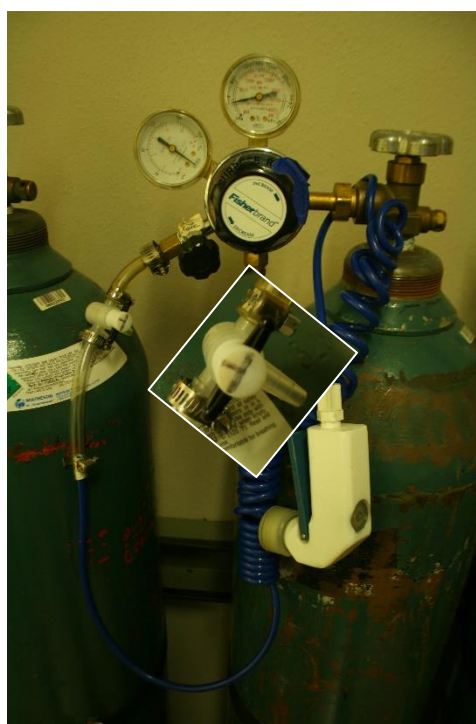


Figure 3.20. Photograph of nitrogen gas cylinder used to supply gas pressure to the airbrush with inset of the three-way valve nipple where the hose for the spray coater was connected.

3.2.3 MEASURING SILVER NANOWIRE ELECTRODE TRANSMITTANCE AND SHEET RESISTANCE

Transmittance of silver nanowire electrodes was measured according to procedures in section 3.1.8. Sheet resistance was measured using four-point probe method. Figure 3.21 shows the Guardian SRM - 232 - 100 used to measure sheet resistance with an inset of the probes. To measure the sheet resistance, the Guardian was assembled by connecting the probes to the surface resistivity meter via cat 6 cable and turned on by pressing and holding the power button. The four probes were then pressed onto the silver nanowire electrode and the sheet resistance was read off the Guardian display screen. When finished, the four-point probe was disassembled and placed in the storage container; the resistivity meter automatically turns off.



Figure 3.21. Photograph of Guardian SRM - 232 - 100 used to measure sheet resistance with an inset of the probes.

3.3 LIFETIME TEST AND CHARACTERIZATION OF SILVER NANOWIRE

ELECTRODES

3.3.1 LIFETIME TEST MEASUREMENT OF SILVER NANOWIRE ELECTRODES

Figure 3.22 shows the experimental set up for measuring the lifetime of silver nanowire electrodes under electrical stress with inset of 3M clips clamping a sample (upper left) and a silver nanowire electrode with silver contacts (lower right). A Keithley 2602A was interfaced through GPIB cable to a desktop PC and controlled through LabView 2015. The LabView program can be viewed in APPENDIX A. Silver nanowire electrodes had silver contacts deposited according to section 3.1.4 with the exception of the three middle long mask cutouts were blocked off with scotch tape (Figure 3.22 lower right). Two 3M and alligator clips were used to connect the Keithley to the silver nanowire electrode, which were subject to 20 mA of constant current. The resulting, voltage, time, and resistance was recorded every hour by the LabView program and saved in an excel spread sheet.

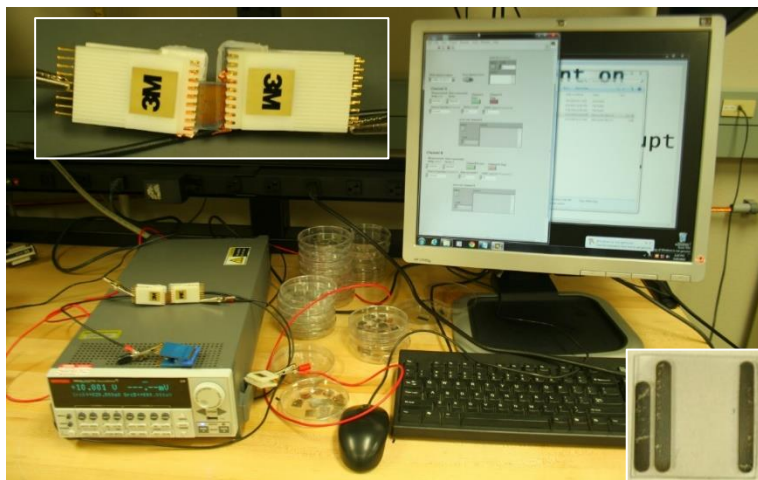


Figure 3.22. Photograph of experimental set up for measuring the lifetime of silver nanowire electrodes under electrical stress with inset of 3M clips clamping a sample (upper left) and a silver nanowire electrode with silver contacts (lower right).

3.3.2 SCANNING ELECTRON MICROSCOPE, OPTICAL PHOTOGRAPHY, X-RAY DIFFRACTION SPECTROMETER, AND ENERGY DISPERSIVE X-RAY SPECTROSCOPY OF SILVER NANOWIRE ELECTRODES

Scanning electron microscope, optical photography, and x-ray diffraction procedures are outlined in sections 3.1.4, 3.1.5, and 3.1.11, respectively. The only differences in x-ray diffraction procedures was that no software tools were used to edit the data.

Energy Dispersive X-ray Spectroscopy (Figure 3.6) operating procedures can be found in the user's manual near the system [115]. The probe current during EDS measurements was increased to 60 - 70% so that the number of X-ray counts from the EDS exceeded 1000. The infrared camera in the SEM system was turned off so that it would not interfere with X-ray signal. Images of the EDS location sites were taken from both the SEM and EDS software interfaces. EDS spectrums and SEM images were

exported into word documents. Element for detection were selected based on assumption of elements expected to be present within the sample. For example, the glass slides were made of silicon, oxygen, and sodium so the detector was set to detect silicon and oxygen. Elements silver is reactive with such as sulfur or chlorine were set to be detected. The automatic software detection of elements such as cadmium or ytterbium were removed from the detection list because their presents within the sample was not reasonable.

To isolate the detection of oxygen due to silver oxide, gold coated silicon wafers (model number) were used as substrates. Silicon wafers (~1.5 by 1.5 cm) were cleaned by soaking in near boiling soapy DI water, DI water in a piranha solution ($\text{H}_2\text{SO}_4:\text{H}_2\text{O}_2$ 30 wt. % concentration) for 5 minutes each. Silicon substrates were rinsed with DI water and dried under compressed nitrogen. Figure 3.23 shows the Plasma Sciences Inc. CrC-150 Sputtering System used to deposit a 200 nm thick gold layer on the silicon substrates. The SOP for the CrC sputtering system can be found in the clean room at Daktronics Engineering hall [116]. Silver nanowires were spray coated according to the procedures in section 3.2.3.



Figure 3.23. Photograph of Plasma Sciences Inc. CrC-150 Sputtering System used to deposit gold.

CHAPTER 4 RESULTS AND ANALYSIS

4.1 DEVELOPMENT OF PEDOT:PSS TRANSPARENT ELECTRODES

4.1.1 SOLVENT ADDITIVES TO PEDOT:PSS ELECTRODES

Figure 4.1 shows the sheet resistance for PEDOT:PSS with various solvent additives. These films were 43 nm thick on average. All films show a dramatic decrease in sheet resistance from pristine films which exhibited 478 to 550 $\text{k}\Omega/\square$. Films with dimethyl sulfoxide (DMSO) additives sheet resistance decreased from 700 to 400 Ω/\square with increasing weight (wt.) %, which is consistent with previous reports [91]. The optimal wt. % for ethylene glycol (EG) was found to be 10 wt. %, which also matched previous reports [117, 118]. Other reports claim 5 wt. % for DMSO or EG additives to be optimal [63, 119]. The reason for these contradictory reports may be attributed to processing conditions. This work utilized a slow drying for PEDOT:PSS films which has not been reported elsewhere. Films with 15 wt. % 1:1 EG:DMSO solvent blend additive were observed to have the lowest sheet resistance of 297 Ω/\square . These trends were found to be repeatable for 8 samples and no reports on optimal solvent blend additives were found.

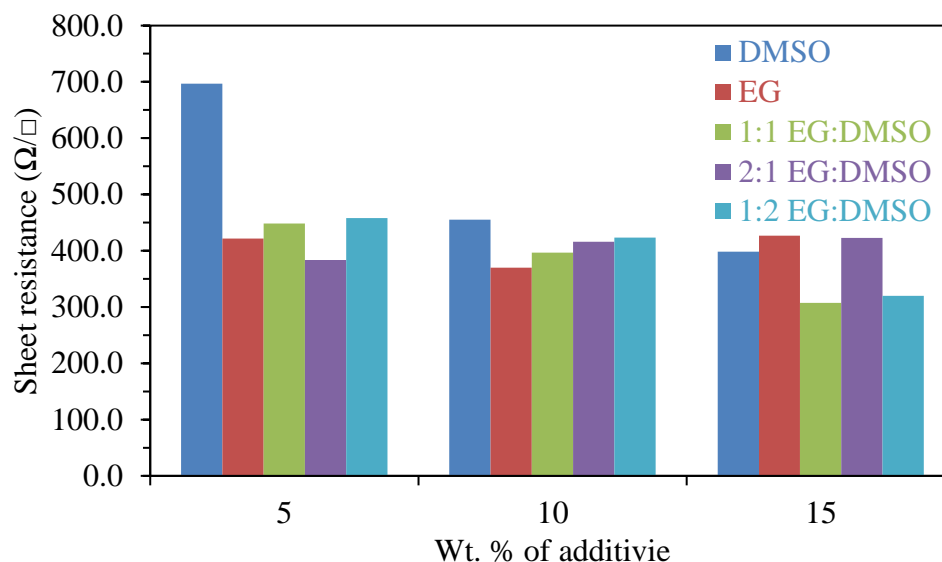


Figure 4.1. Comparison of sheet resistance for PEDOT:PSS with various solvent additives.

Figure 4.2 shows time lapsed photos of the slow drying process for PEDOT:PSS film with 15 wt. % 1:1 DMSO:EG additive. These photos are represented for samples with 15 wt. % of other solvents and solvent blends and took approximately 15 minutes to completely dry in air. Samples with 0, 5, and 10 wt. % additive take 0, 5, and 10 minutes to completely dry, respectively. The increasing dry time is directly linked to the amount of solvent additive in the PEDOT:PSS films. The longer drying time was attributed to additional high boiling point solvents within the film and may allow for the films to rearrange PEDOT and PSS in a more optimal morphology.

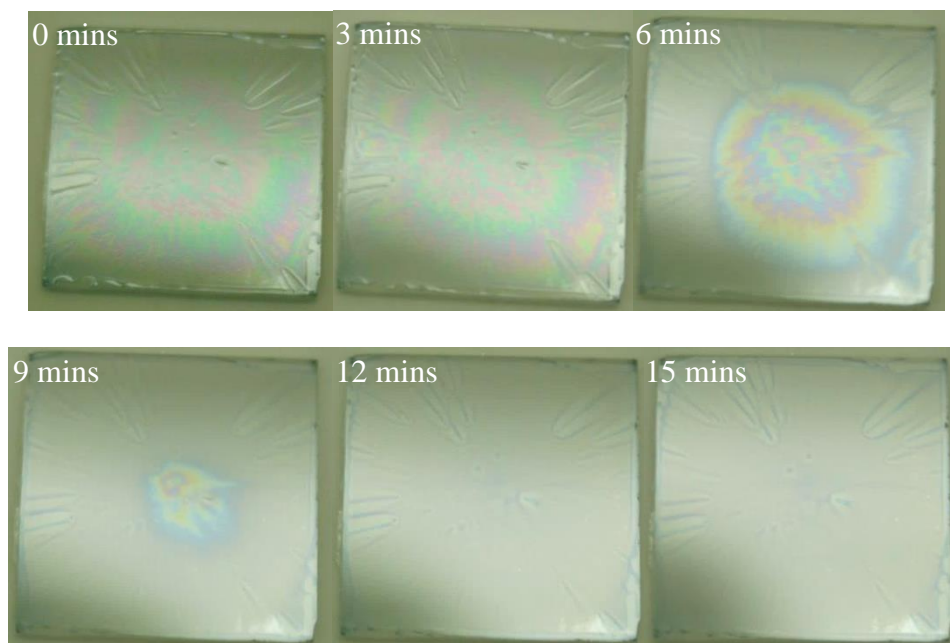


Figure 4.2. Time lapsed photos of the slow drying process for PEDOT:PSS film with 15 wt. % 1:1 DMSO:EG additive.

Figure 4.3 shows the sheet resistance for PEDOT:PSS films soaked in various solvents and solvent blends. The lowest average sheet resistance was found to be $326 \Omega/\square$ for 1:1:1 water:EG:ethanol blend. Various other blends with EG such as 1:1 water:EG, 1:1 EG:ethanol, and 1:1:1 DMSO:EG:ethanol also exhibited lower sheet resistance ranging from $350 - 387 \Omega/\square$. Intrinsic EG exhibited a high sheet resistance of $441 \Omega/\square$, which suggests that EG needs to be blended with a solvent such as water or ethanol to be more effective. Similar trends were observed by Xia. et al. who blended organic solvents with water [65]. They found water:ethanol blends gave the best enhancement in conductivity and attributed the ethanol to help solvate the PEDOT:PSS film and allow the water to penetrate and help rearrange the film. However, water can also be used to dissolve PEDOT:PSS, and the data from Figure 4.3 suggest that both the ethanol and water can be used to solvate the PEDOT:PSS where the EG polar groups will

help reorganize the film. It is curious that DMSO did not have the same enhancing effects as EG, and suggests there are different mechanisms behind how the two solvents influence PEDOT:PSS films.

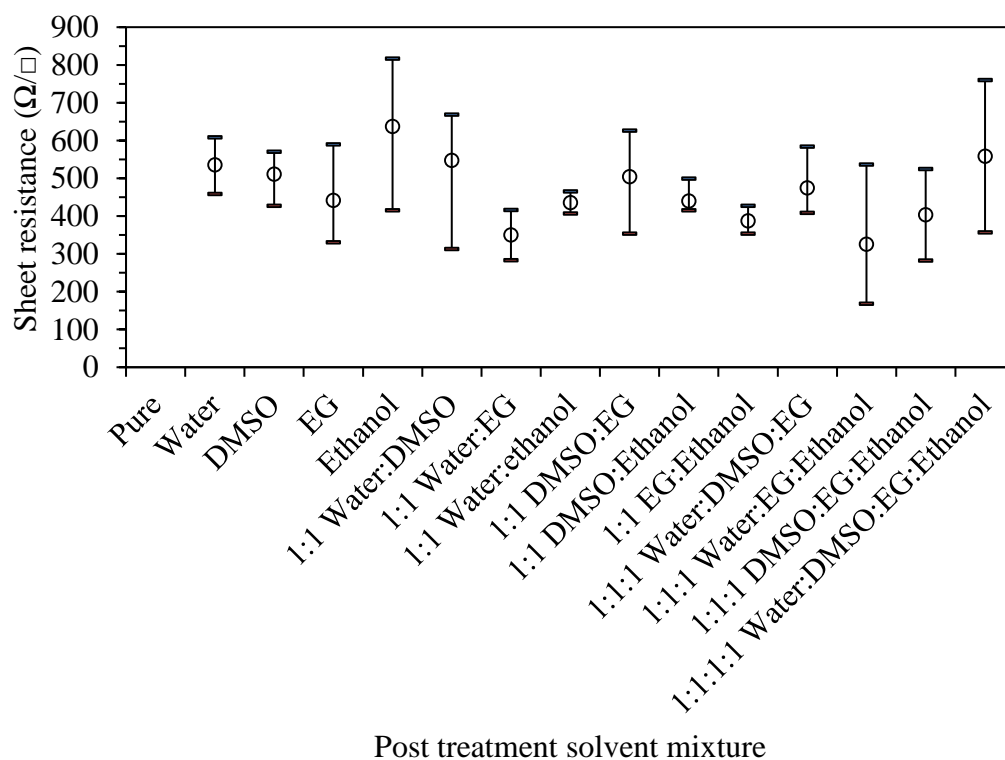


Figure 4.3. Sheet resistance for PEDOT:PSS films soaked in various solvents and solvent blends.

Figure 4.4 shows topography images of (a) pristine PEDOT:PSS and PEDOT:PSS with (b) 10 % wt. EG, (c) 15 % wt. DMSO, (d) 15 % wt. 1:1 DMSO:EG additives, and (e) 15 % wt. 1:1 DMSO:EG after being soaked in water:EG:ethanol (1:1:1). The pristine film had a rolling-hill like morphology. After adding 10 wt. % EG small circular grains are observed to appear in the film. In contrast, 15 wt. % DMSO exhibited smaller oblong grains in the film. The difference in morphology for EG and DMSO additives cases

suggests that each additive interact with the PEDOT:PSS differently. Consequently, it is not unreasonable to assume that the mechanism for conductivity enhancement is also different. The morphology for 15 wt. % 1:1 EG:DMSO also exhibits a fibrous morphology similar to films with only DMSO additive. After soaking the film in 1:1:1 water:EG:ethanol no significant morphology changes were observed.

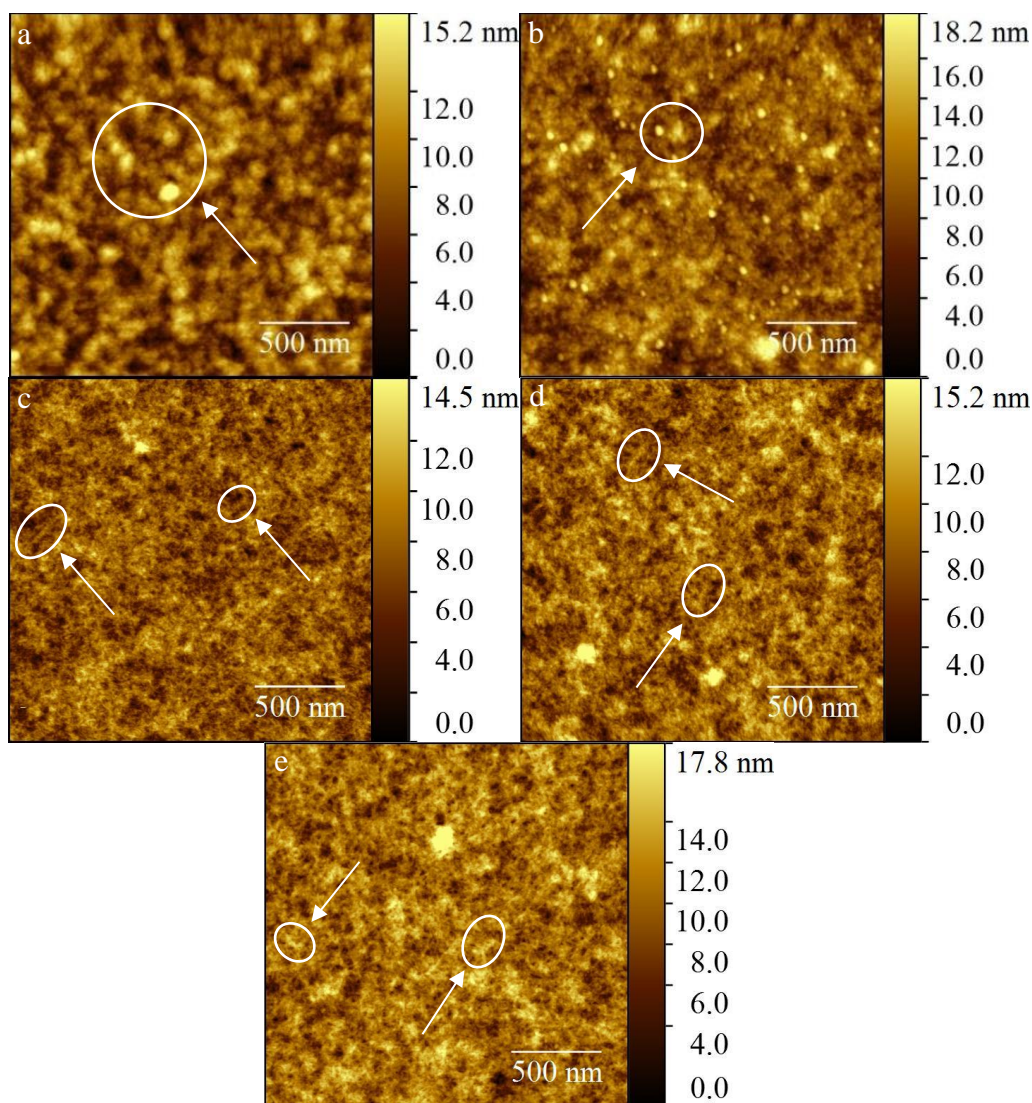


Figure 4.4. Topography images of (a) pristine PEDOT:PSS and PEDOT:PSS with (b) 10 % wt. EG, (c) 15 % wt. DMSO, (d) 15 % wt. 1:1 DMSO:EG additives, and (e) 15 % wt. 1:1 DMSO:EG after being soaked in water:EG:ethanol (1:1:1).

Small granular features are often reported for PEDOT:PSS samples with EG, which have been proposed to be composed of highly ordered PEDOT:PSS grains surrounded by a PSS shell [83, 120]. Current-sensing atomic force microscopy (CS-AFM) was used to understand the composition of these small granular features. Figure 4.5 shows the (a) topography, (b) CS-AFM performed at 0.1 V bias for PEDOT:PSS films with 10 wt. % EG, and (c) line scan from images (a) and (b) (indicated by white line). Figure 4.5 (a) shows the small granular features present and Figure 4.5 (b) shows small islands of higher current levels. The small islands of higher current observed in in Figure 4.5 (b) should correspond to the small grains in observed in Figure 4.5 (a) if the grains are composed of highly ordered PEDOT:PSS. From Figure 4.5 (d), the small islands of higher current in CS-AFM do correspond to peaks in the topography which suggests that the small grains are highly conductive and supports the notion that they are composed of highly ordered PEDOT:PSS domains. Moreover, the dark areas around the small islands of high current would correspond to the non-conducting PSS shell around the highly ordered PEDOT:PSS grains.

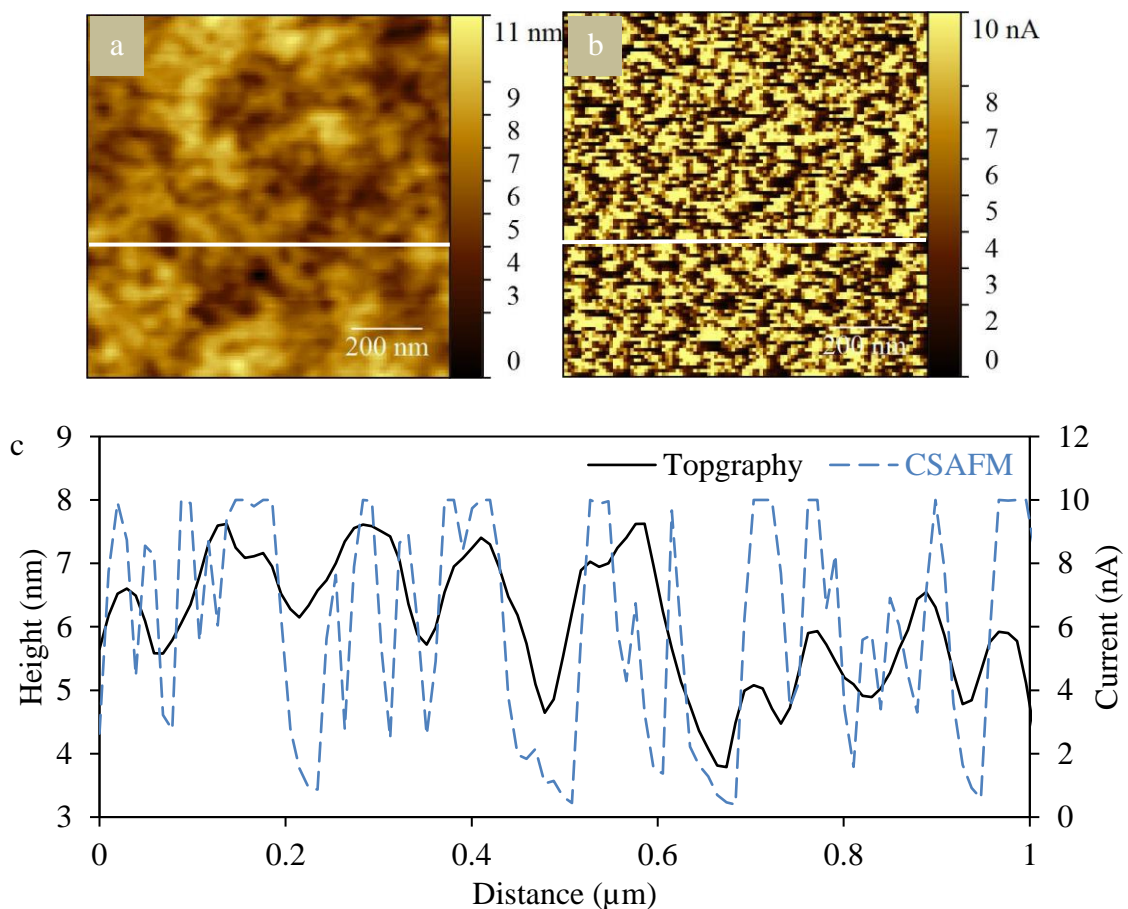


Figure 4.5. (a) Topography, (b) current-sensing atomic force microscopy performed at 0.1 V bias for PEDOT:PSS films with 10 wt. % EG, and (c) line scan from images (a) and (b) (indicated by white line).

Figure 4.6 show the (a) topography and (b) current-sensing atomic force microscopy performed at 0.3 V bias pristine PEDOT:PSS films. The pristine film is much less conductive compared to the film in Figure 4.5 (b). The higher voltage bias also strongly supports this as when the pristine sample was scanned with 0.1 V bias (as performed for Figure 4.5 (b)) no current was detected, which was attributed to a thick insulating PSS barrier and lack of conductive PEDOT networks within the film.

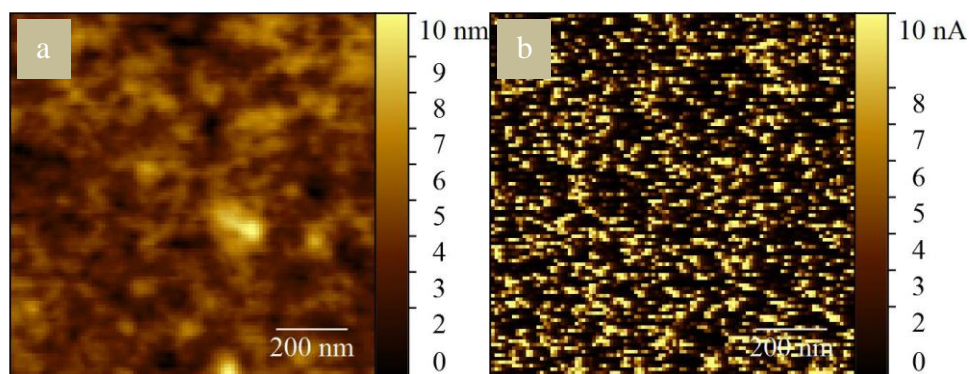


Figure 4.6. (a) Topography and (b) current-sensing atomic force microscopy performed at 0.3 V bias pristine PEDOT:PSS films.

Figure 4.7 shows the (a) topography of PEDOT:PSS film with 15 wt. % DMSO:EG (1:1) additive and corresponding CS-AFM images under 0.1 Volt bias after (a) first, (c) second, and (d) third consecutive scans. Figure 4.7 (b) shows a constant value of 10 nA and demonstrates superior electrical properties of 15 wt. % DMSO:EG over the 10 wt. % EG additive from Figure 4.5 (b); this is also consistent with sheet resistance values from Figure 4.1. After a second scan over the same area (Figure 4.7 (c)), the current begins to drop, attributed to the platinum\Chromium plating on the silicon AFM tip wearing off. After a third scan (Figure 4.7 (d)), the current has dramatically dropped and the current flow reversed, which was attributed to future removal of the platinum\Chromium plating and altering the work function of the AFM tip. Figure 4.7 (b) though (d) demonstrate how easily the CS-AFM tips can be damaged after only three scans.

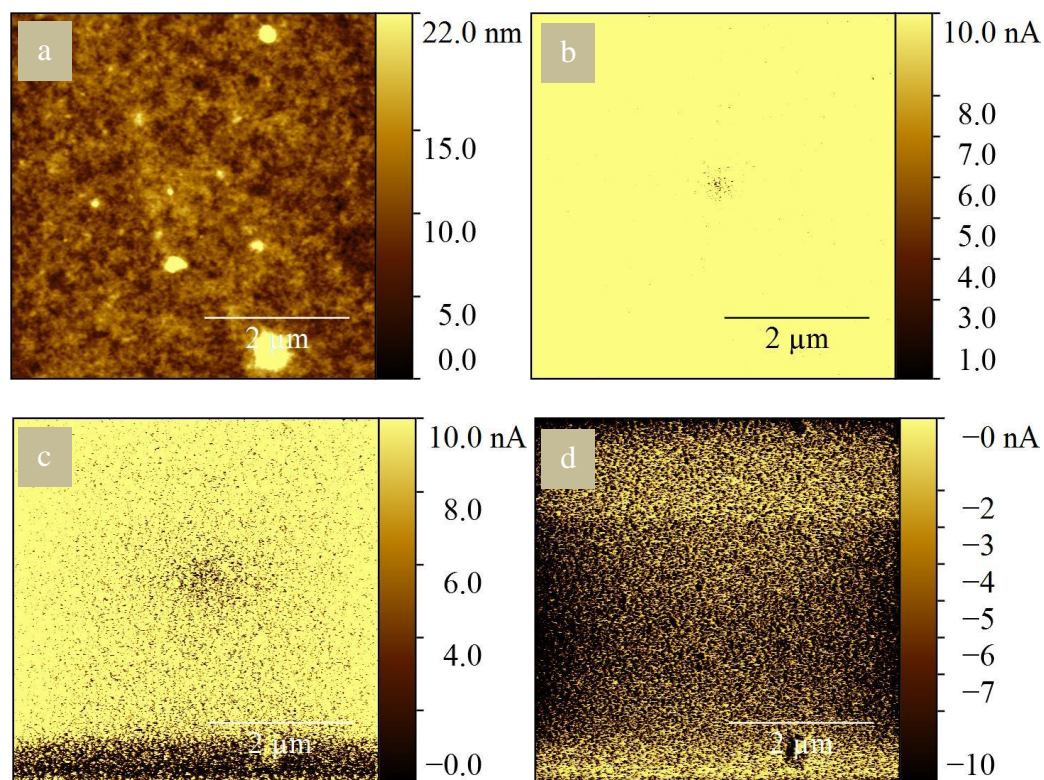


Figure 4.7. (a) Topography of PEDOT:PSS film with 15 wt. % DMSO:EG (1:1) additive and corresponding CS-AFM images under 0.1 Volt bias after (a) first, (c) second, and (d) third consecutive scans.

Figure 4.8 shows the ultraviolet-visible absorbance spectra of PEDOT:PSS films (a) with various EG wt. % additives and with 15 wt. % 1:1 EG:DMSO before and after post treatment and (b) PEDOT:PSS films with various wt. % DMSO additives. The two peaks observed at 193 nm and 225 nm are attributed to PSS absorption [74]. A decrease in peak intensity at 193 nm and 225 nm are observed with increasing wt. % of EG and a dramatic decrease in peak intensity is observed after solvent blend post treatment. The decrease in peak intensity was attributed to EG rearranging the PSS within the PEDOT:PSS film. It is possible that excess PSS was removed during the spin coating process, but Xia et al. showed that by rearranging the PSS morphology to an uneven

distribution across the film a decrease in absorption can be expected [65]. It is proposed here that the polar groups from the EG are interacting with the PSS species to rearing it in an uneven distribution during the film formation. The decrease in absorption from the post treatment can be attributed to excess PSS species being washed away from the film. Because the absorbance of the film from 310 nm to 1100 nm does not change, it can be infrared that the film thickness is not changing with increasing wt. % additives. Figure 4.8 b shows no change in PSS peak absorption with increasing DMSO wt. % additive, thus the DMSO does not seem to have a significant impact on the PSS species within the film.

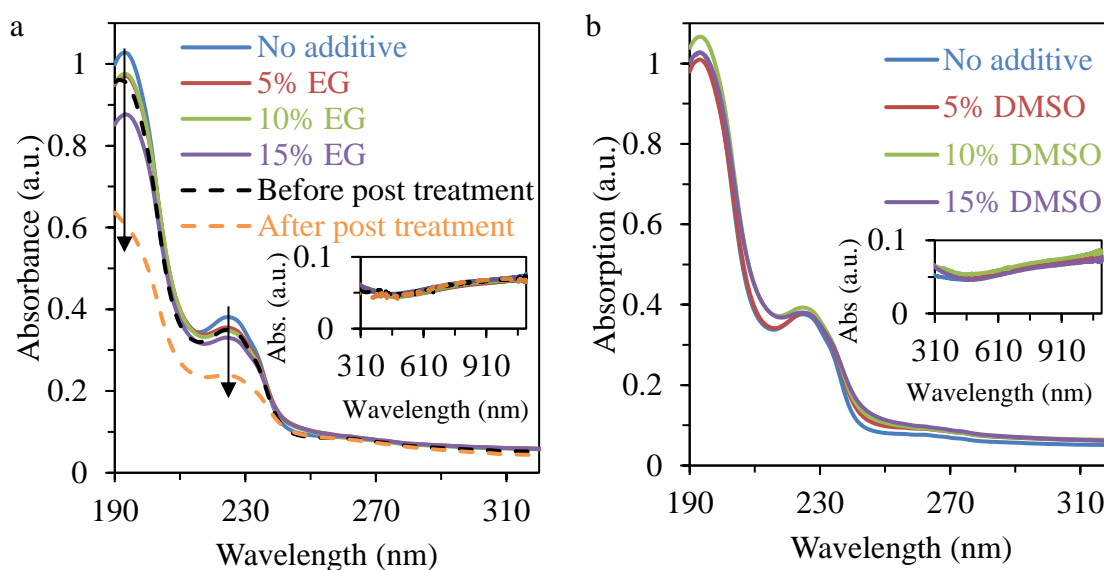


Figure 4.8. Ultraviolet-visible absorbance spectra of PEDOT:PSS films (a) with various EG wt. % additives and with 15 wt. % 1:1 EG:DMSO before and after post treatment and (b) with various wt. % DMSO additives.

Figure 4.9 shows the Raman spectra for PEDOT:PSS films for increasing % wt. of (a) EG and (b) DMSO additive. The peak occurring between $1350 - 1425 \text{ cm}^{-1}$ is attributed to $C_{\alpha}=C_{\beta}$ symmetric stretching within the PEDOT species [83, 106, 121].

Figure 4.9 (a) shows no change with increasing % wt. of EG additive, thus EG does not appear to affect the PEDOT species. A redshift is observed in Figure 4.9 (b) with increasing DMSO additive. The redshift can be attributed to the PEDOT changing from its less conductive benzoid structure to its more conductive quinoid structure. This change in chemical resonance structure is attributed to the DMSO additive. The strong dipole moment of DMSO may help separate PSS from PEDOT, enabling the PEDOT to take on a linear formation. Figure 4.9 b also shows that the DMSO:EG blend had the largest redshift, this suggests the solvent blend was more efficient at converting the PEDOT to its quinoid structure. APPENDIX B shows the Raman spectroscopy for all solvent blend additives, again 15 wt. % 1:1 DMSO:EG was observed to have the largest redshift. This is also in agreement that the films with 15 wt. % 1:1 DMSO:EG exhibited the lowest sheet resistance, as the quinoid PEDOT structure is more conductive than the benzoid structure.

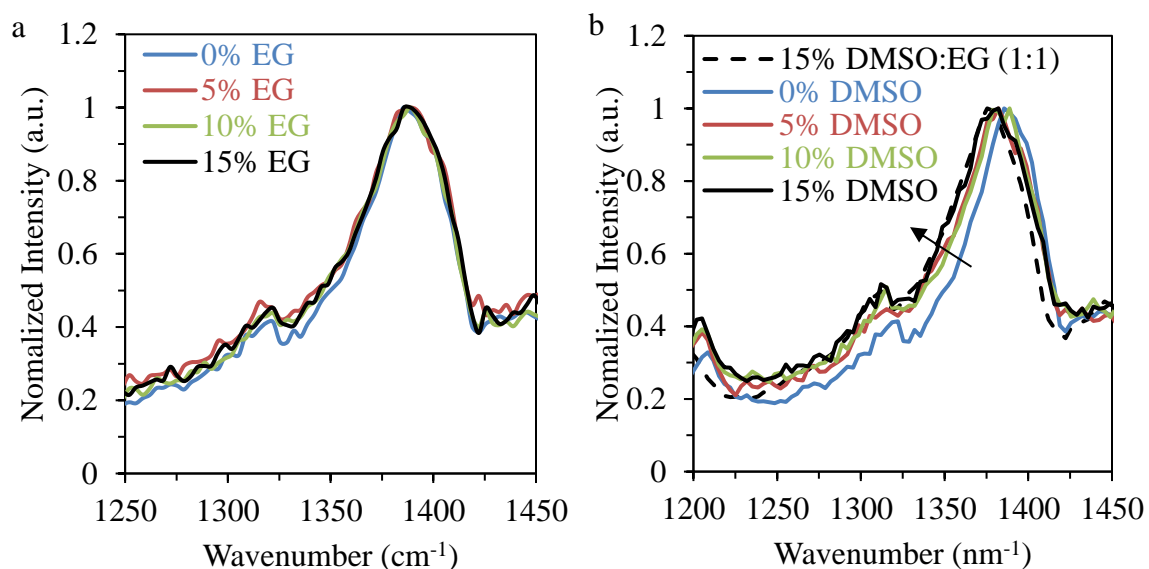


Figure 4.9. Raman spectra for PEDOT:PSS films for increasing % wt. of (a) EG and (b) DMSO and 1:1 DMSO:EG additive.

Figure 4.10 illustrates PEDOT:PSS morphology for (a) pristine, (b) 10 wt. % EG, (c) 15 wt. % DMSO, (d) 15 wt. % DMSO:EG 1:1, and (e) 15 wt. % DMSO:EG 1:1 additive after post treatments. Figure 4.10 (a) depicts the rolling hill morphology of the pristine film which is more disordered and has PSS blocking electron pathways. In Figure 4.10 (b), the small circular grains observed in Figure 4.4 (b) for 10 wt. % additive of EG being composed of a more ordered PEDOT and PSS species. Figure 4.10 (c) depicts more oblong grains observed for 15 wt. % DMSO additive in Figure 4.4 (c) and PEDOT taking its quinoid form. Figure 4.10 (d) depicts similar morphology to Figure 4.10 (c) but with fewer PSS barriers for 15 wt. % DMSO:EG (1:1) as observed from the absorption spectrum in Figure 4.8. The solvent additive blend provides a dual mechanism where the EG rearranges the PSS species to reduce insulating barriers and the DMSO enable PEDOT to convert to the quinoid structure. Figure 4.10 (e) depicts similar morphology to Figure 4.10 (d) but with fewer PSS species due to the post treatment washing them away also observed from the absorption spectrum in Figure 4.8 (a). The post treatment further reduces the PSS insulating barriers within the PEDOT:PSS film.

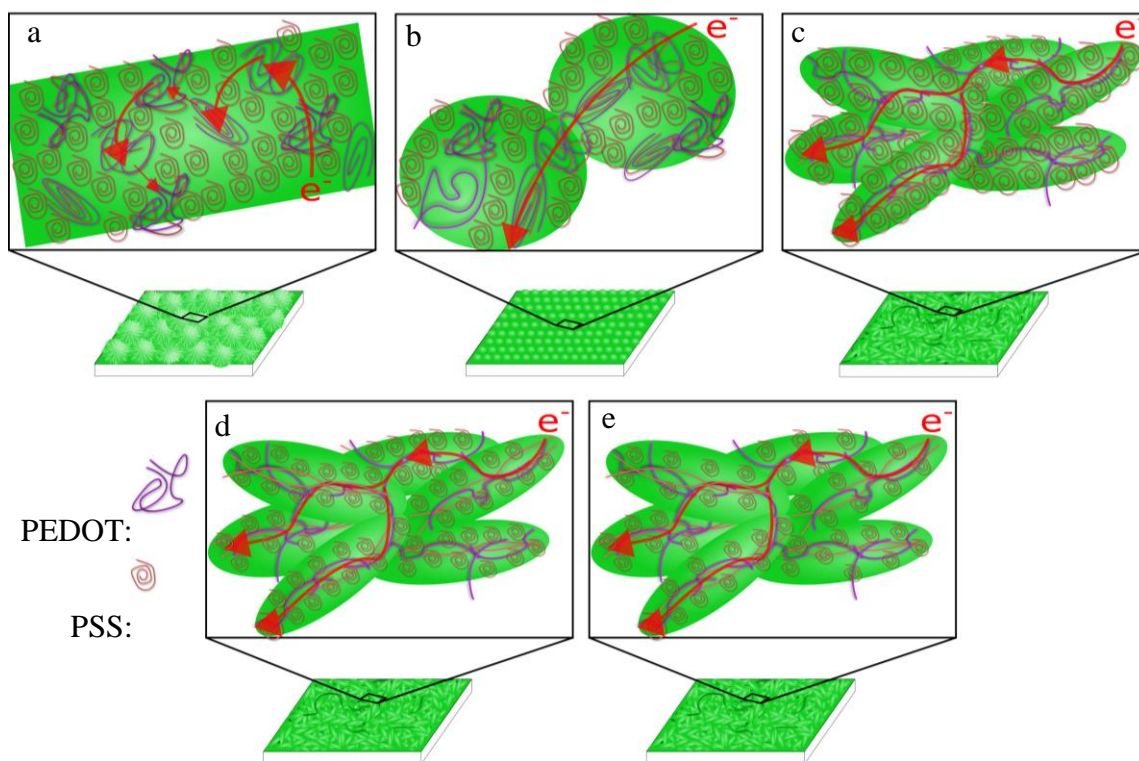


Figure 4.10. Morphology illustration of PEDOT:PSS for (a) pristine, (b) 10 wt. % ethylene glycol (EG), (c) 15 wt. % DMSO, (d) 15 wt. % DMSO:EG 1:1, and (e) 15 wt. % DMSO:EG 1:1 additive after post treatments.

4.1.2 PEROVSKITE SOLAR CELL FABRICATION USING PEDOT:PSS ELECTRODES

The PEDOT:PSS with 15 wt. % 1:1 DMSO:EG with a post treatment of soaking in 1:1:1 water:EG:ethanol was used to fabricate the perovskite solar cell. Four layers of these PEDOT:PSS films were deposited on top of one another, which exhibited a sheet resistance of $80 \Omega/\square$ and average transmittance over 350 nm - 900 nm of 73%. Due to the hydrophobic nature of the PEDOT:PSS films after the post treatment, the PEDOT:PSS ink was blended 2:1 with IPA to improve wetting for additional layers. The sheet resistance and transmittance were not able to meet the objectives listed in Chapter 1. A

three layer PEDOT:PSS electrode exhibited an average transmittance around 80% but had high sheet resistance above $100 \Omega/\square$. The four-layer electrode was considered the best tradeoff between sheet resistance and transmittance.

Figure 4.11 shows the (a) XRD spectra of perovskite on top of a four layer PEDOT:PSS electrode and ITO electrode and topography images of perovskite on top of (b) ITO and (c) PEDOT:PSS electrodes. From Figure 4.11 (a) the characteristic perovskite crystal peaks 14.1° and 28.5° confirm that the perovskite was able to form on top of the PEDOT:PSS electrode. The crystallite sizes for the perovskite film on the PEDOT:PSS and ITO electrode were calculated to be 216 \AA and 235 \AA , respectively by using the Scherrer equation. Figure 4.11 (b) and (c) show the average perovskite crystallite size on the ITO and PEDOT:PSS electrode is $\sim 250 \text{ nm}$ and $\sim 284 \text{ nm}$, respectively. The smaller perovskite crystallite and particle size on the PEDOT:PSS electrode could lead poorer photovoltaic device performance due to a higher number of defects, which would act as trap states to free flowing electrons and holes.

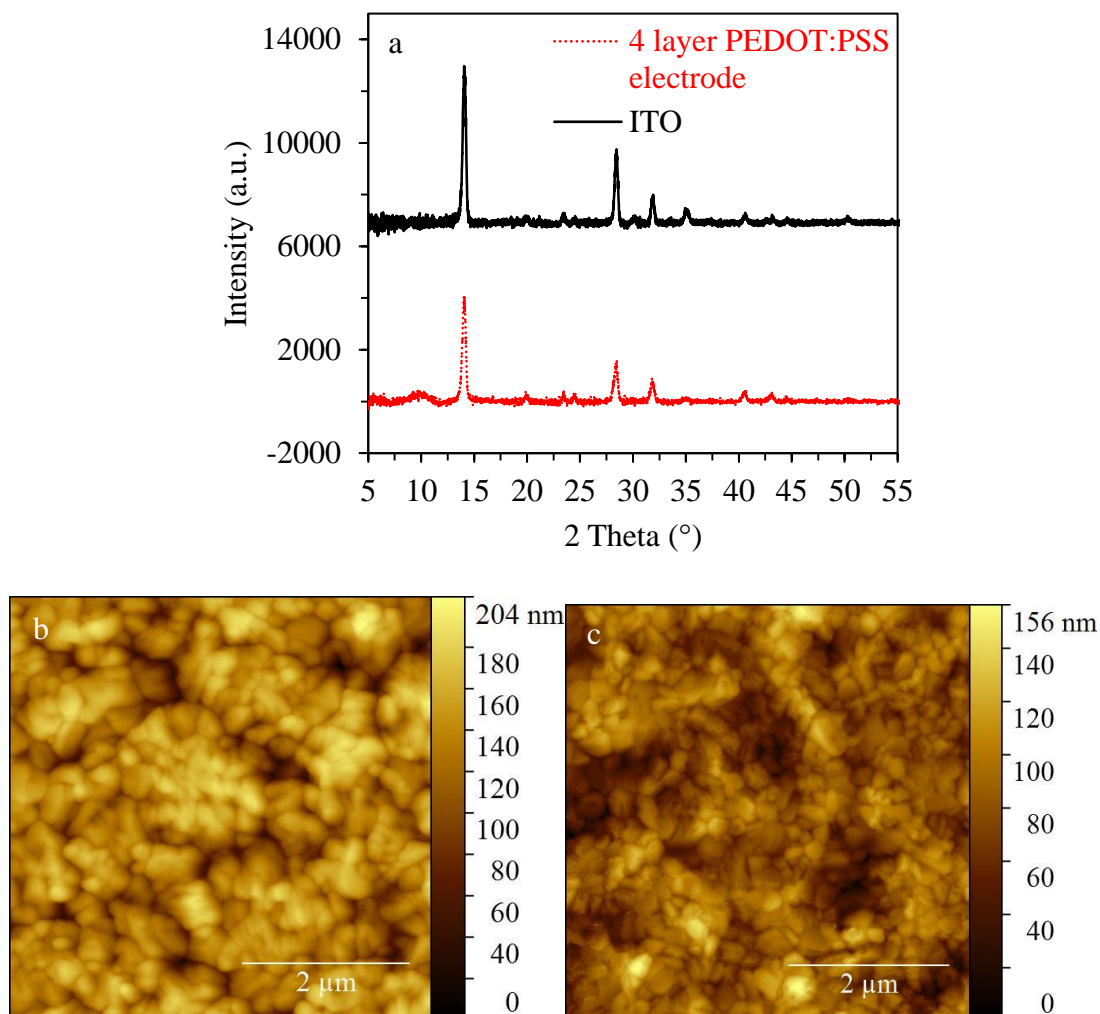


Figure 4.11. (a) XRD spectra of perovskite on top of a four layer PEDOT:PSS electrode and ITO electrode and topography images of perovskite on top of (b) ITO and (c) PEDOT:PSS electrodes.

Figure 4.12 shows (a) perovskite device structure and (b) I-V curves for perovskite solar cells. The PCE for the perovskite solar cell with PEDOT:PSS electrode was 5.3% vs 12.4% for the ITO electrode. The poorer performance from the PEDOT:PSS electrode was due to a low J_{sc} , V_{oc} , and FF compared to the ITO as shown in Table 4.1. The lower J_{sc} for the PEDOT:PSS based device was attributed to the PEDOT:PSS

electrode's average transmittance (over 350 nm - 900 nm) of 73% compared vs. ITO, which exhibited 84% transmittance. Lower transmittance results in lower light absorption and photocurrent. The lower V_{oc} for the PEDOT:PSS electrodes can be attributed to a higher defect density within the perovskite layer, which is also supported by smaller crystallite and particle size from the XRD and AFM data, respectively, in Figure 4.11 for perovskite films on top of PEDOT:PSS electrodes [55, 122]. The low FF for the PEDOT:PSS based device was attributed to the PEDOT:PSS electrode's high sheet resistance of $80 \Omega/\square$ vs. $16 \Omega/\square$ for the ITO electrode.

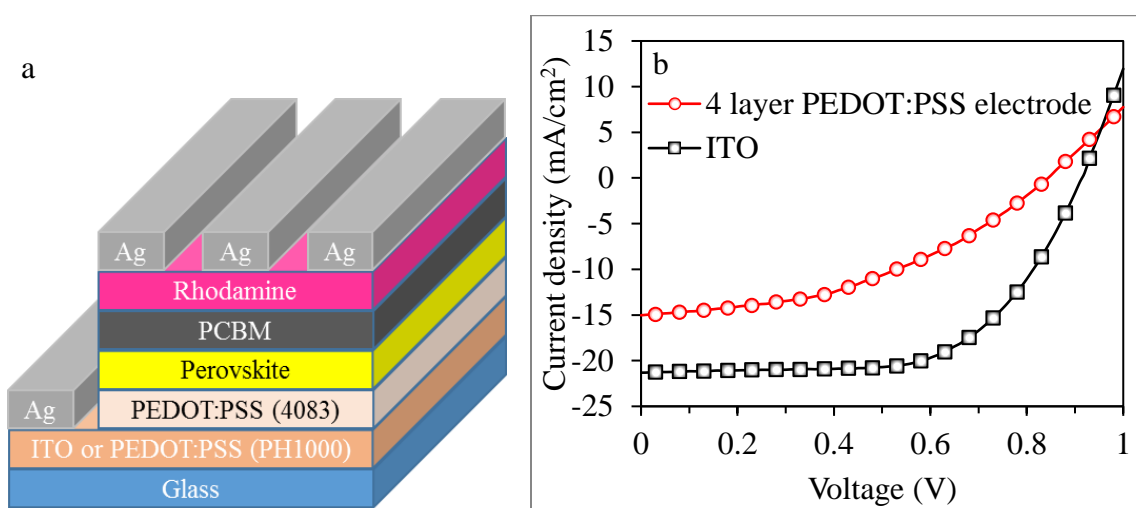


Figure 4.12. (a) Perovskite device structure and (b) I-V curves for perovskite solar cells.

Table 4.1. Device parameters for perovskite solar cells made using PEDOT:PSS and ITO as transparent electrode.

	J_{sc} (mA/cm ²)	V_{oc} (V)	FF	PCE (%)
PEDOT:PSS	15.0	0.84	0.42	5.3
ITO	21.1	0.9	0.65	12.4

Figure 4.13 shows the transient photocurrent for perovskite solar cells made with 4 layer PEDOT:PSS electrodes and ITO electrodes. A charge transport time of $0.9 \mu\text{s}$ and $1.1 \mu\text{s}$ was found for perovskite solar cells with ITO and PEDOT:PSS electrodes, respectively. The charge transport time for PEDOT:PSS electrodes was very similar to that of ITO, which suggests that charge transport within the solar cell is not significantly affected. If the transmittance and conductivity of the PEDOT:PSS electrode can be increased, without increasing surface roughness, it could easily replace ITO as a transparent electrode.

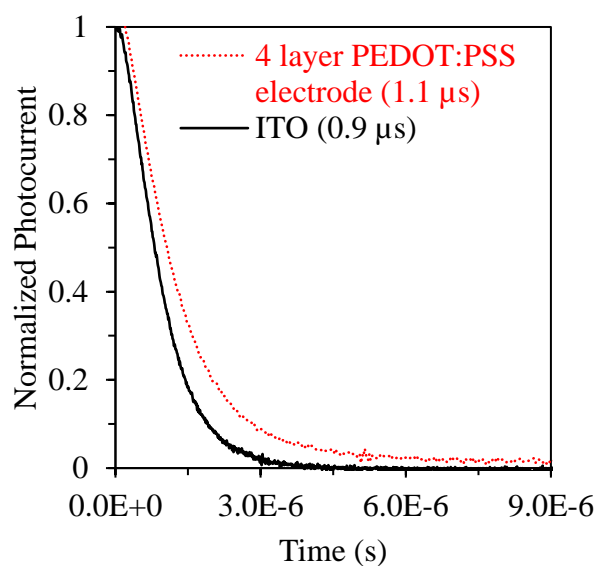


Figure 4.13. Transient photocurrent for perovskite solar cells made with 4 layers of PEDOT:PSS electrodes and ITO electrodes.

4.2 SILVER NANOWIRE TRANSPARENT ELECTRODES LIFETIME UNDER ELECTRICAL STRESS

4.2.1 EFFECT OF UV-OZONE ON SILVER NANOWIRE ELECTRODES

Figure 4.14 shows the dependence of sheet resistance and transmittance at 550 nm on annealing temperature with 30 minutes annealing time (highlighted in blue columns) and 10 minutes annealing time (no highlight). Samples annealed at 140 °C and 160 °C for 10 minutes were able to achieve transmittances above 80 % (above solid black line) and sheet resistances below 50 Ω/\square (below dotted red line). Thus, the objectives outlined chapter 1 were met using silver nanowire electrodes. Samples annealed at 200 °C were fabricated with silver nanowires synthesized at 160 °C; all other data was obtained using silver nanowires synthesized at 150 °C. Longer annealing times for silver nanowire electrodes fabricated with silver nanowires at 150 °C resulted in higher sheet resistance attributed to the nanowire melting and breaking apart. All silver nanowire electrodes made with silver nanowires synthesized at 160 °C and annealed at temperatures 180 °C or less resulted in sheet resistances greater than 100 Ω/\square . This was attributed silver nanowires synthesized at 160 °C having a higher heat resistance and the lower temperatures not being able to meld the nanowire junctions together.

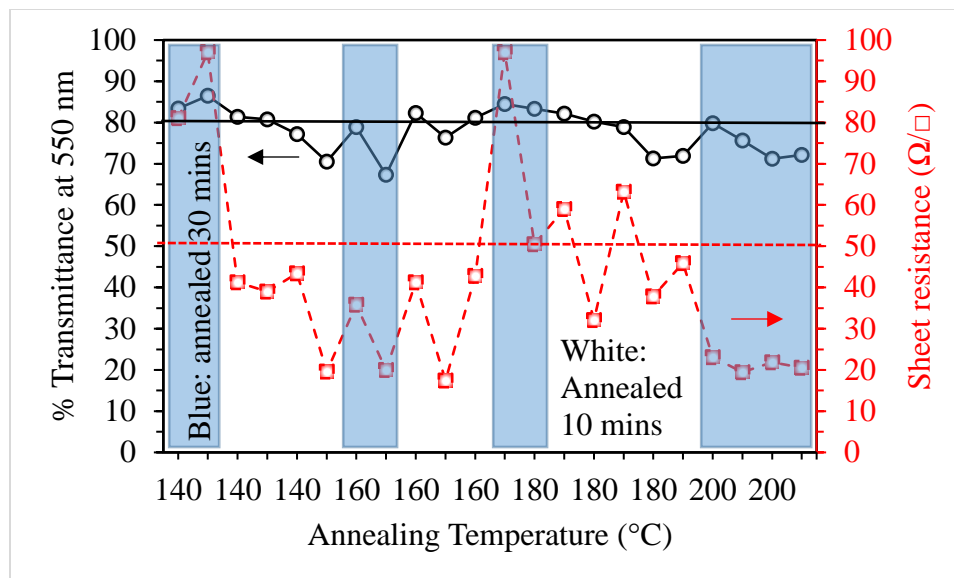


Figure 4.14. Dependence of sheet resistance and transmittance at 550 nm on annealing temperature with 30 minutes annealing time (highlighted data) and 10 minutes annealing time (no highlight).

Table 4.2 shows the dependence of sheet resistance on UV-ozone treatment time for silver nanowire electrodes. With increasing UV-ozone treatment time, the sheet resistance of the films increased. This was attributed to the ozone reacting with the silver to form a silver oxide layer on the outside of the nanowires. Silver oxide is not conductive and would ultimately reduce the sheet resistance of the films.

Table 4.2. Dependence of sheet resistance on UV-ozone treatment time on silver nanowire electrodes

Test Trial	Sheet Resistance with UV-Ozone Treatment Times				
	0 min	1 min	2 mins	5 mins	10 mins
1	15 Ω/□	17 Ω/□	19 Ω/□	20 Ω/□	22 Ω/□
2	36 Ω/□	59 Ω/□	60 Ω/□	68 Ω/□	97 Ω/□

Figure 4.15 shows the EDX spectra for silver nanowire (a) before and (b) after 1 minute of UV-ozone treatment with SEM image inset of the measurement location. The silver nanowires were deposited on gold coated silicon. The gold coating was 200 nm thick and used to prevent the EDX from detecting oxygen from silicon dioxide, which commonly forms on silicon wafers. Table 4.3 shows that no oxygen was detected from the silver nanowire/gold/silicon sample, attributed to the gold layer preventing detection of silicon dioxide. After the UV-ozone treatment a small wt.% of oxygen is detected, which was attributed to the silver forming silver oxide. Silver is able to form an oxide easier than gold, therefore the detection of oxygen is more likely due to the formation of silver oxide than gold oxide. This data are also consistent with Table 4.2 where a silver oxide layer would increase the sheet resistance of the silver nanowire electrodes.

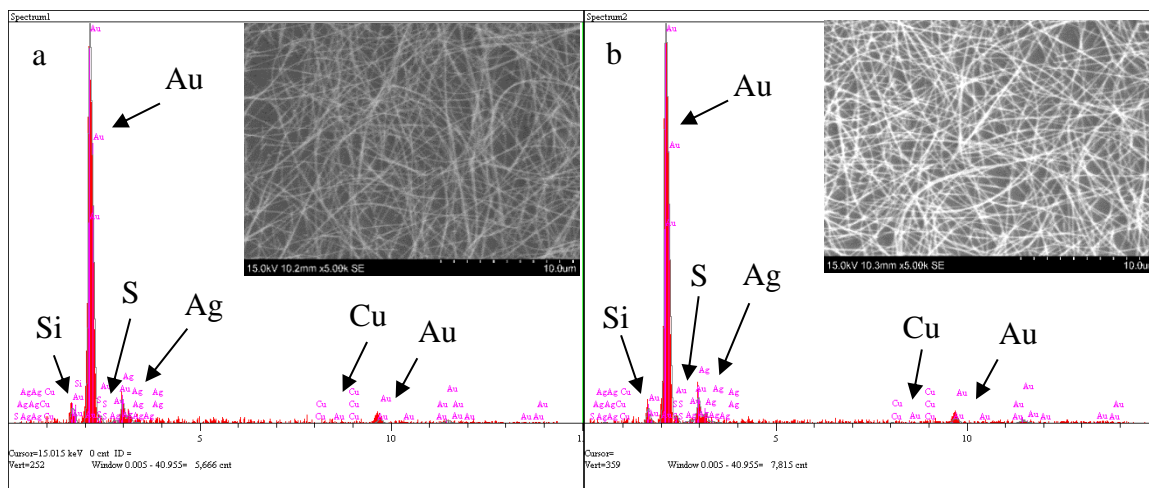


Figure 4.15. EDX spectrum for silver nanowire electrodes (a) before and (b) after 1 minute of UV-ozone treatment with SEM image inset of the measurement location.

Table 4.3. Wt.% of elements detected from silver nanowire electrodes before and after 1 minute UV-ozone treatment.

Element.	Line	Before UV-Ozone Treatment			After UV-Ozone Treatment		
		Intensity (c/s)	Error 2-sig	Concentration (wt.%)	Intensity (c/s)	Error 2-sig	Concentration (wt.%)
O	Ka	0.00	0.000	0.000	0.88	0.595	0.203
Si	Ka	4.04	1.271	0.402	2.11	0.918	0.144
S	Ka	0.00	0.000	0.000	0.00	0.000	0.000
Cu	Ka	0.19	0.274	0.115	1.52	0.780	0.638
Ag	La	17.97	2.681	9.816	28.52	3.377	10.596
Au	Ma	253.12	10.062	89.667	365.61	12.093	88.420

4.2.2 ELECTRODE FAILURE UNDER ELECTRICAL STRESS

Figure 4.16 shows the frequency of the silver nanowire (a) diameter and (b) length. The average nanowire diameter for silver nanowire synthesized at 150 °C and 160 °C was 72 nm and 88 nm, respectively. The average length for the silver nanowires synthesized in both cases was 16 μm . The dimensions of the nanowire in both batches was considered to be similar enough to not affect the outcome of the measurement and from here on will be collectively referred to by their overall average diameter of 80 nm.

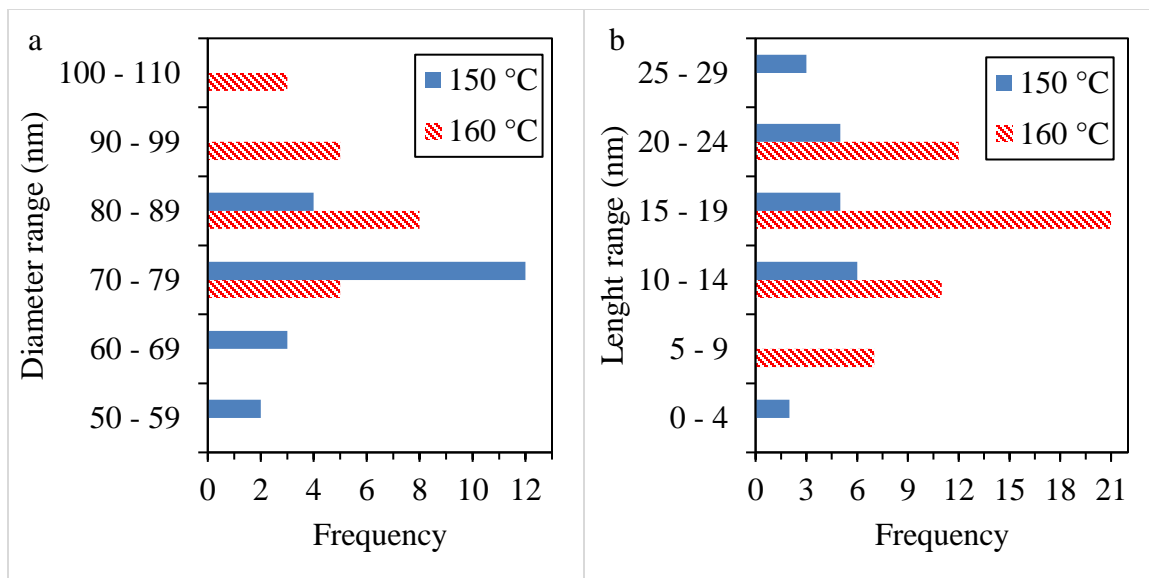


Figure 4.16. Distribution of silver nanowire (a) diameter and (b) length.

Figure 4.17 shows SEM images of silver nanowires, with magnified inset, synthesized at (a) 150 °C and (b) 160 °C. The silver nanowire morphology appears to be similar in both cases such that it was not considered to play an important role in the measurement outcome.

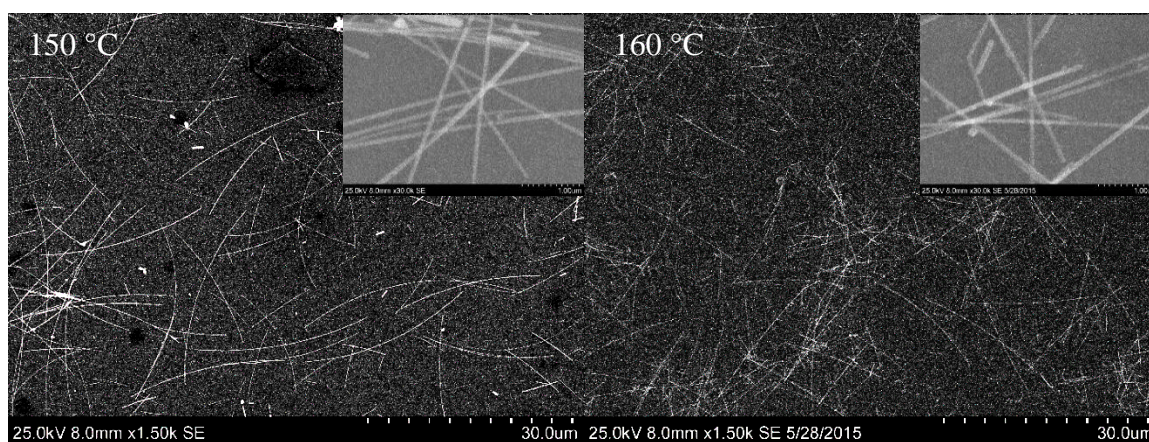


Figure 4.17. SEM images of silver nanowire, with zoomed inset, synthesized at (a) 150 °C and (b) 160 °C.

Figure 4.18 shows the dependence of silver nanowire formation time on silver nanowire synthesis temperature. The silver nanowire reaction time was found to be linearly related to synthesis temperature. Higher synthesis temperatures result in faster reaction times. In addition, the longer the nanowire reaction was carried out after the nanowires formed, the nanowire diameter would continue to grow (see APPENDIX C). Thus, at higher reaction temperatures nanowire diameter increased much more quickly. A longer reaction time is easier to control the nanowire dimensions because of their slower reaction time. At around 140 °C, however, the reaction results in poorly formed nanowires. The inset of Figure 4.18 shows an SEM image of silver nanowire synthesized at 140 °C, which exhibit large particles and rough surface morphology compared to those in Figure 4.17. The rough morphology was attributed to the lower temperatures inhibiting proper crystalline growth of the silver nanowires on the (111) plain. Hu et. al. reported that 140 °C was the lowest temperature silver nanowire reactions could be carried out at [123].

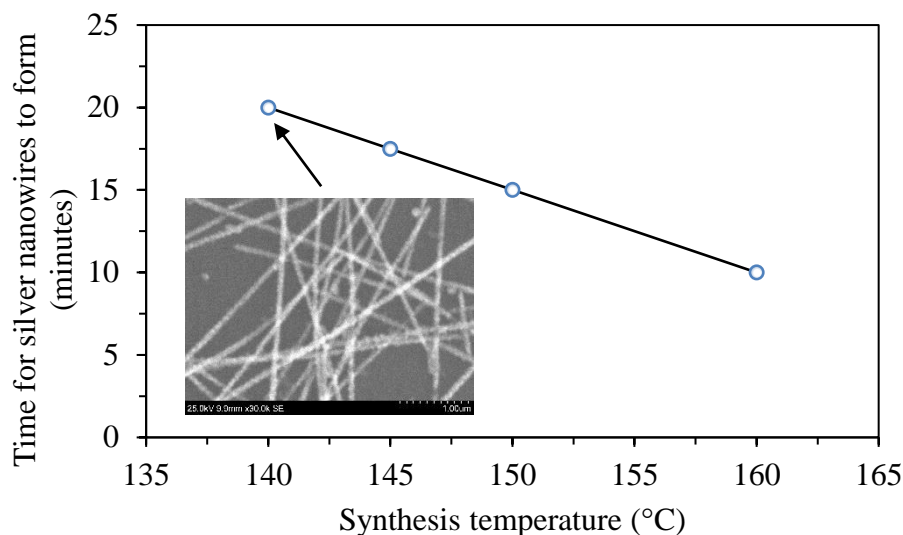


Figure 4.18. Dependence of silver nanowire formation time on synthesis temperature.

The inset is a SEM image of silver nanowire synthesized at 140 °C.

The silver nanowire average diameter, synthesis temperature, UV- treatment condition, electrode annealing temperature, and the resulting sheet resistance are shown in Table 3.4. The sheet resistance of the silver nanowire electrodes for each respective test was considered comparably close in value to not have a significant effect on the electrode lifetime. To achieve sheet resistance below $50 \Omega/\square$, electrodes used in test 1 and test 2 required a minimum of 140 °C and 200 °C annealing temperatures despite both having similar diameters. This discrepancy was attributed to the synthesis temperature of the silver nanowires. Silver nanowires formed at 160 °C were more heat resistant than nanowires formed at 150 °C and needed higher temperature to meld the nanowire junctions together. Typically, thinner nanowire requires less annealing temperature, but the difference in average nanowire diameters of 72 nm and 87 nm does not seem large enough to account a 60 °C difference in annealing temperature, therefore it may be related to how crystalline the silver nanowires are. Nanowires with higher degree of

crystallinity will be less likely to melt at lower temperature compared to those with a more amorphous nature [124]. The silver nanowires with average diameter of 233 nm required an annealing temperature of 300 °C to achieve sheet resistances below 50 Ω/\square . The higher annealing temperature for thicker nanowires was attributed to their larger diameter acting more like bulk silver. Bulk silver has a melting temperature of 962 °C, yet nanowires are able to melt at lower temperatures because the fraction of atoms on the surface to the total number of atoms becomes is large. As the nanowires become thicker in diameter, this fraction decreases in size and the nanowires becoming much more thermally stable. The major disadvantage of thick nanowires is that they are much less transparent due to the thick diameters interacting with visible light and they create a higher surface roughness.

Table 4.4. Relationship between silver nanowire average diameter, synthesis temperature, synthesis temperature, UV- treatment condition, electrode annealing temperature, and the resulting sheet resistance.

Test	Average Nanowire Diameter (synthesis temperature)	UV Treated	Sheet Resistance	Electrode Annealing Temperature
1	72 nm (150 °C)	Yes	39 Ω/\square	140 °C
1	72 nm (150 °C)	No	41 Ω/\square	140 °C
2	87 nm (160 °C)	Yes	23 Ω/\square	200 °C
2	87 nm (160 °C)	No	23 Ω/\square	200 °C
3	233 nm	Yes	20 Ω/\square	300 °C
3	233 nm	No	15 Ω/\square	300 °C

Figure 4.19 shows a voltage versus time plot for silver nanowire electrodes with different synthesis temperatures and nanowire diameters subject to 20 mA/cm^2 of constant current density. Interestingly, the UV-treated silver nanowires lasted two days longer in both cases for thinner nanowires. This was attributed to the oxide layer protecting the silver nanowires from corrosion due to sulfur compounds in the air. Silver nanowires, with average nanowire diameter of 80 nm, synthesized at 150°C and 160°C lasted for 54 and 32 days, respectively, which is a new record for nanowires of this size. The longer lifetime of silver nanowire synthesized at 150°C was attributed to the lower contact resistance at the nanowire junctions compared to nanowires synthesized at 160°C . Table 4.4 shows silver nanowires synthesized at 150°C required a lower annealing temperature, which suggests the nanowire junctions are easily melted together. UV-treated and non-UV-treated silver nanowires with thicker diameters, failed after 128 days and 263 days, respectively. The longer lifetime of thicker nanowires was attributed to their higher thermal stability and longer corrosion time. If the nanowires begin to corrode, a larger diameter will require more time to completely corrode than smaller diameters. The non-UV-treated nanowire electrodes with thicker diameters met the 6000 hour objective in Chapter 1.

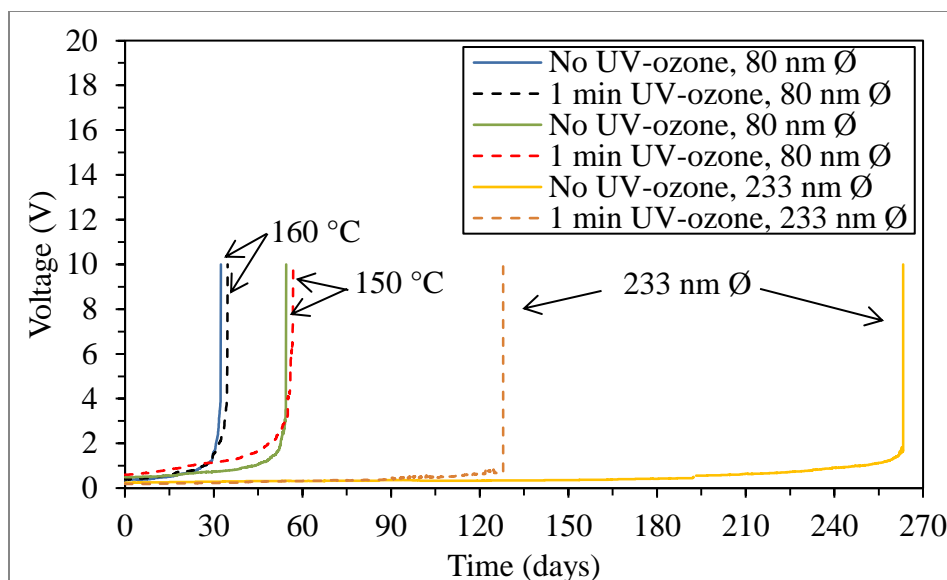


Figure 4.19. Voltage verse time plot for silver nanowire electrodes with different synthesis temperatrues and nanowire diameters subject to 20 mA/cm^2 of constant current density.

Figure 4.20 shows a photograph of silver nanowire electrodes with 233 nm average nanowire diameters after (a) freshly sprayed, (b) 9 month of air exposure, (c) 9 month of air exposure after failed from electrical, (d) failed from electrical stress, and silver nanowire electrodes with 80 nm average nanowire diameter (e) after failure and 15 months' exposure to air and (f) 15 months' exposure to air. The dark grey color in Figure 4.20 (b) was attributed to sulfur tarnishing the silver nanowires. However, the purple-red-brown and yellow colors in Figure 4.20 (c) and (d) could be attributed to chlorine or sulfur silver tarnish [125]. It is interesting to note that the yellow color was always present as long as the electrode was subject to electrical stress. Once the power was turned off, the yellow color would fade to a purple-red-brown. Figure 4.20 (e) and (f) do not exhibit much color attributed to the thinner nanowires diameters leading to a more transparent electrode.

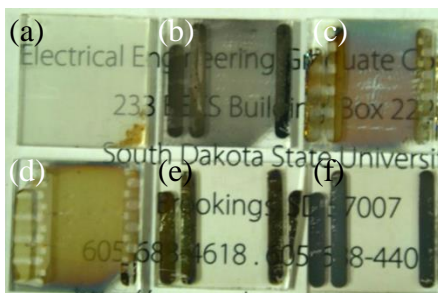


Figure 4.20. Photographs of silver nanowire electrodes with 233 nm average nanowire diameters after (a) freshly sprayed, (b) 5 month of air exposure, (c) 5 month of air exposure after failed from electrical, (d) failed from electrical stress, and Silver nanowire electrodes with 80 nm average nanowire diameter (e) after failure and 15 months' exposure to air and (f) 15 months' exposure to air.

Figure 4.21 shows the EDS spectra of silver nanowire electrodes with thicker nanowire diameters with SEM image inset of measurement location after (a) failure from electrical stress and (b) left in air for 9 months. From the corresponding Table 4.5, sulfur was detected and no chlorine was detected in both cases. This is consistent with previous reports that claim sulfur compounds in air are primarily responsible for the corrosion of silver nanowires [73, 93]. The presence of sulfur (and not chlorine) was attributed to the silver nanowires corroding.

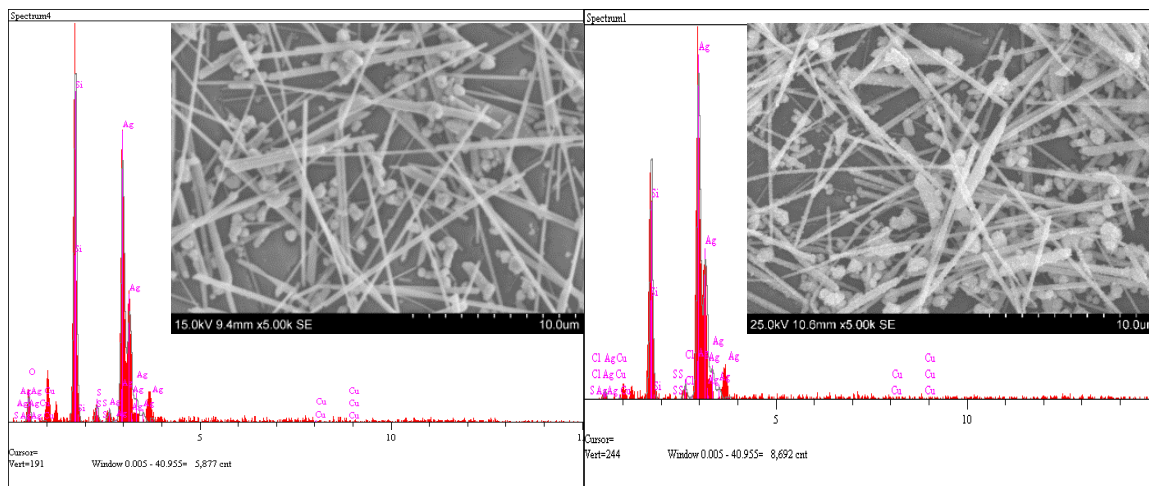


Figure 4.21. EDS spectrum of silver nanowire electrode with thicker nanowire diameters with SEM image inset of measurement location after (a) failure from electrical stress and (b) left in air for 9 months.

Table 4.5. Wt.% of elements detected from Figure 4.19 (a) and (b).

Element	Line	After failure from electrical stress			After 9 month air exposure		
		Intensity (c/s)	Error 2-sig	Concentration (wt.%)	Intensity (c/s)	Error 2-sig	Concentration (wt.%)
O	Ka	10.92	2.090	1.850	5.28	1.454	0.969
Si	Ka	175.58	8.380	20.575	166.49	8.161	17.756
S	Ka	8.70	1.865	1.091	0.48	0.437	0.046
Cl	Ka	0.00	0.000	0.000	0.00	0.000	0.000
Cu	Ka	1.21	0.695	0.920	0.92	0.608	0.185
Ag	La	150.28	7.753	75.563	255.76	10.114	81.044

Figure 4.22 shows (a) XRD spectra of silver nanowires with average diameters of 233 nm (b) zoomed in portion of (a). The two large peaks located at 38.2° and 44.4° in Figure 4.22 (a) and smaller peaks located at 64.5° and 77.5° in Figure 4.22 (b) can be attributed silver nanowires (111), (200), (220), and (311), respectively. These peaks were located using ICDD reference 01-087-0720 and also line up well with other reports [126]. Other smaller peaks from Figure 4.22 (b) located at 34.3° , 36.4° , 39.8° , and 42.4° , were attributed to Ag_8S , Ag_8S , AgS_2 , and Cu_2O , respectively. These peaks were identified using ICDD reference number 01-078-2076 for Cu_2O , 01-083-0674 for Ag_8S , and 01-083-0674 for AgS_2 . XRD future confirms the presents of sulfur bonding with the silver nanowires. The color changes observed in Figure 4.20 are likely due to sulfur tarnish on the silver nanowires.

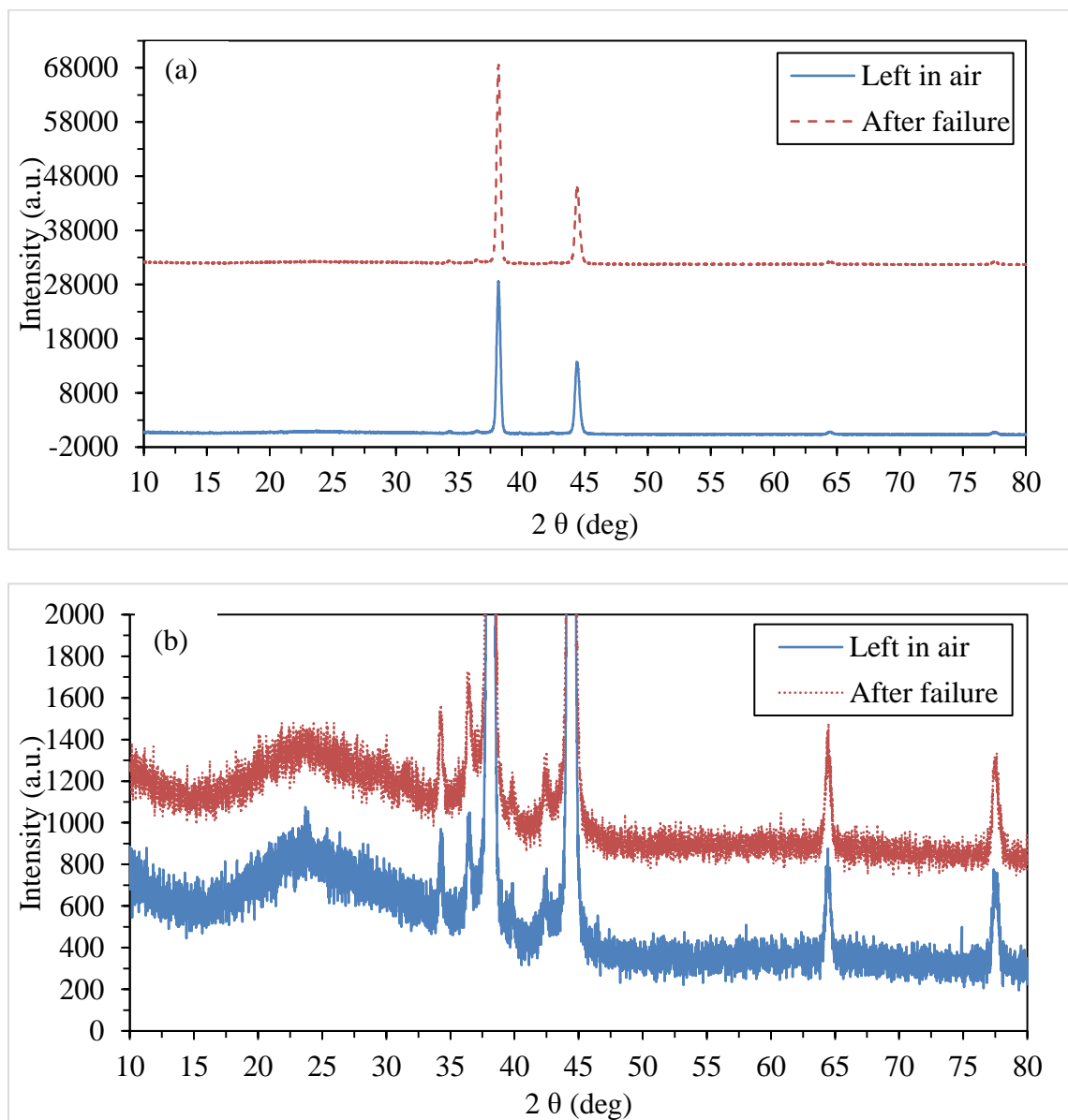


Figure 4.22. (a) XRD spectra of silver nanowires with average diameters of 233 nm (b) zoomed in portion of (a)

Figure 4.23 shows SEM images of failed silver nanowires electrodes with average diameters of (a) (b) 80 nm and (c) (d) 223 nm, where (a) and (c) are representative of the entire sample and (b) and (d) depict broken nanowires. From Figure 4.13 (a) and (c) no

broken nanowires or faulty connections are observed, and finding locations depicted in Figure 4.23 (b) and (d) proved difficult and time consuming. This suggests that the silver nanowire electrode failed due to a few key faults in the conductive percolating nanowire network. It is possible that the lifetime of the electrode could be enhanced if the conductive pathways within the nanowire mesh was more evenly distributed. Figure 4.23 (b) and (d) show that the failure points for thinner nanowire typically occurred at nanowire junctions where failure points for thicker nanowires occurred along the nanowires themselves. This was attributed to that the thinner nanowires failing due to Joule heating and corrosion while the thicker nanowires failed due to corrosion. The longer lifetime of UV-treated electrodes for thinner nanowires was attributed to the thin oxygen layer slowing the corrosion process from the sulfur compounds in the air. The corrosion of the nanowires would occur more rapidly at nanowire junction, due to the higher temperature from Joule heating. The corrosion reduces the conductive area of the nanowires, which accelerates failure due to Joule heating. The thicker nanowires, on the other hand, likely had lower resistance at nanowire junctions. However, thicker nanowires are still susceptible to corrosion especially at defect sites within the nanowire [93]. The failure of UV-treatment thicker nanowire electrodes was attributed to the UV-treatment reducing the conductive area of the nanowires, thus making defect sites more susceptible to Joule heating and corrosion [93, 95]. Figure 4.23 (d) also shows the two broken nanowires had a diameter of 121 nm and 167 nm, which is much thinner than the average nanowire diameter. It is likely that the thicker nanowires would last much longer if key percolating network connections were not dependent on thinner nanowires.

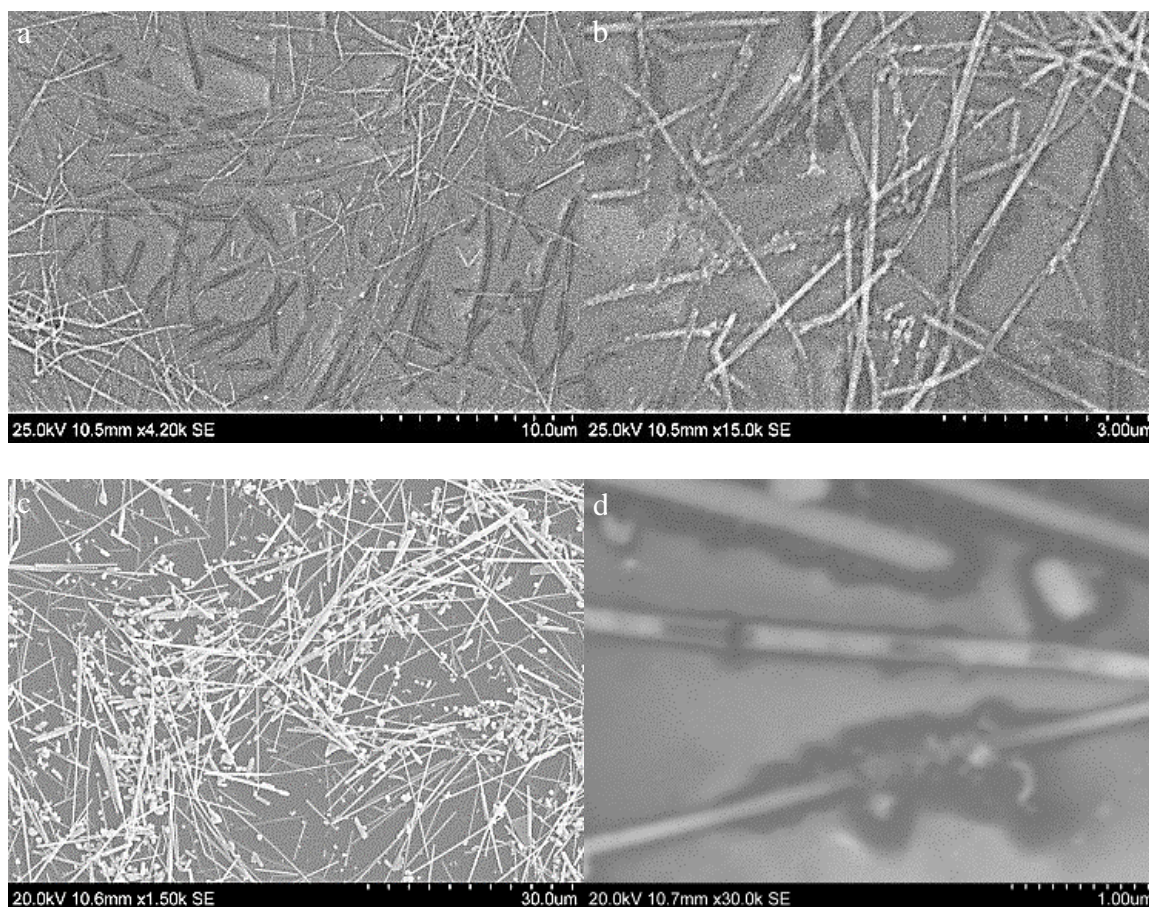


Figure 4.23. SEM images of failed silver nanowire electrodes with average diameters of (a) (b) 80 nm and (c) (d) 223 nm, where (a) and (c) are representative of the entire sample and (b) and (d) depict broken nanowires.

Figure 4.24 shows voltage vs time of silver nanowire electrodes subject to 20 mA of constant current. After two months of rest time, the failed silver nanowire electrode was able to exhibit low voltage levels for 3 more days. After a second failure and one-week rest time, the silver nanowire electrode exhibited low voltage levels for 3 hours. This self-healing could be very useful in light of stability concerns of silver nanowire electrodes. To date no tests have been made to study silver nanowire under electrical stress with intermittent rest times to simulate the operation of a solar cell at day and night

time. The self-healing was attributed to melted nanowires reforming together after cooling.

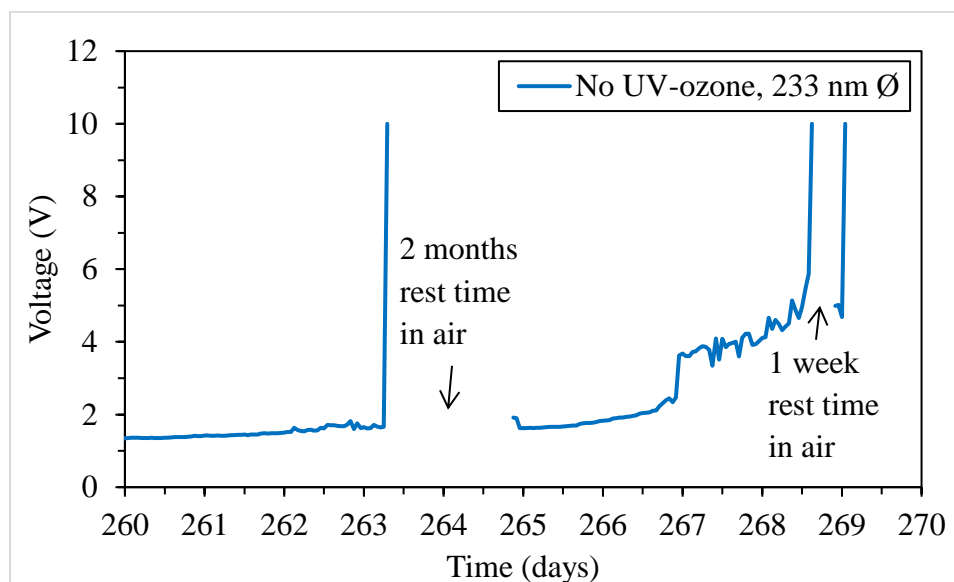


Figure 4.24. Voltage vs time of silver nanowire electrodes subject to 20 mA of constant current.

In summary, the PEDOT:PSS electrode exhibited a sheet resistance of $80 \Omega/\square$ and average transmittance of 73%, which fell short of the objectives of sheet resistance less than $50 \Omega/\square$ and average transmittance greater than 80%. The silver nanowire electrodes with nanowire diameters of 80 nm and 233 nm were able to last a maximum of 1,365 hours and 6,319 hours, respectively. The thicker nanowires were able to meet the 6000-hour objective but the thinner nanowires were not. UV-ozone treated thinner nanowires lasted for 2 days longer than non-treated electrodes, which was attributed to the oxide layer resisting nanowire tarnishing. Thicker nanowires failed sooner with UV-ozone treatment due to longer time for sulfur compounds to penetrate the protective oxide. Silver nanowires also exhibited a self-healing after being allowed to rest after failure. For

the first time a self-healing trait was observed in the silver nanowire electrodes. Given proper protection from tarnishing is provided, the self-healing of silver nanowire electrode would recover during the night and exhibit a long term stability.

CHAPTER 5 CONCLUSIONS

5.1 SUMMARY

The demand for energy continues to climb as the world's fossil fuel supply wanes. Fossil fuels cannot provide a sustainable future. Renewable energy is the best option ensure future energy security. It is clear that wind, hydro, nuclear, and solar all have a part to play in the needed energy paradigm shift. But of the aforementioned renewable energies, only solar has the potential to meet global energy demands, not pose an environmental threat, or suffer from negative sentiment. Building integrated photovoltaics and one way to make effective use of available space and generate power where it is needed. Semitransparent organic solar cells for power generating windows is one example of building integrated photovoltaics. In order to be cost effective, however, the entire device must be solution processed, not utilizing expensive vacuum deposited indium tin oxide (ITO) electrodes.

Indium tin oxide has been the dominate transparent electrode technology for organic solar cells. Silver nanowire electrodes and poly(3,4-ethylenedioxythiophene):poly(styrenesulfonate) (PEDOT:PSS) electrodes after strong acid treatments have shown much promise as a solution processed alternative to ITO. Strong acid treatments on PEDOT:PSS electrodes are not compatible with low cost role-to-role fabrication on flexible plastic substratights. PEDOT:PSS films with solvent additives or solvent post treatments have not enhanced the conductivity to compete with ITO. To solve this, solvent blend additives and post treatments could be used as an alternative. The lifetime of silver nanowires was shown to fail quickly under electrical stress, with the best results reporting up to 20 days [95]. Adding a silver oxide layer to

the silver nanowires or increasing the nanowire diameter could enhance corrosion resistance and heat tolerance of the silver nanowire electrodes.

There is a need for a fully solution processed-ITO free semi-transparent solar cell for power generating window applications. The objective of this work was to fabricate a fully solution processed semi-transparent solar cell without the use of ITO or vacuum deposition technology. To achieve this objective the following tasks were established: 1) Fabricate a transparent silver nanowire electrode (cathode) and PEDOT:PSS electrode (anode) with transparency greater than 80% and sheet resistance less than $50 \Omega/\square$, 2) improve silver nanowire lifetime to 6000 hours or greater under constant electrical stress, and 3) fabricate a semitransparent solar cell with average transmittance greater than 50% within the visible light region (450 - 750 nm) and PCE greater than 4% using PEDOT:PSS and silver nanowire semitransparent electrodes.

PEDOT:PSS is composed of an electrically conductive polymer PEDOT⁺ and made soluble through coulombic interactions with the electrically insulating PSS⁻. Acid treatments on PEDOT:PSS films effectively removed excess PSS⁻ and change PEDOT⁺ to its more conductive quinoid structure. Ethylene glycol (EG) or dimethyl sulfoxide (DMSO) solvent additives enhanced conductivity via morphology optimization and inducing quinoid PEDOT⁺ structure, respectively. Solvent post treatments wash away excess PSS⁻ species. Using both solvent additives and solvent post treatments could mimic acid treatment on PEDOT:PSS films.

Silver nanowires have been shown to fail under electrical stress due to Joule heating and sulfur corrosion. When electrical current passes through these junctions, heat is generated, which causes the nanowires to melt and break electrical contact. Structural

defects in the silver nanowires are more susceptible to corrosion especially at elevated temperatures. A silver oxide is more heat resistance and could help prevent sulfur from corroding the nanowires, moreover, thicker nanowires may be more heat tolerant.

The effect of solvent additives, solvent blend additives, solvent post treatments, and solvent blend post treatments on the sheet resistances of PEDOT:PSS electrodes was investigated and optimized. Using transfer length method, atomic force microscopy (AFM), current sensing AFM, UV-visible spectroscopy, and Raman spectroscopy. A perovskite solar cell was fabricated on top of a four layer PEDOT:PSS semi-transparent electrode and characterized with AFM, X-ray diffraction (XRD), I-V curves, and transient photocurrent.

The lifetime of silver nanowire electrodes was studied by subjecting them to 20 mA of constant current. The effects of different synthesis temperature, UV-ozone treatment, and nanowire diameter had on the lifetime was investigated. The electrodes were characterized using four-point-probe, UV-visible spectroscopy, scanning electron microscopy, energy dispersive X-ray spectroscopy, and XRD.

A four layer PEDOT:PSS electrode with 15 wt. % DMSO:EG (1:1) and post treatment by soaking in water:EG:ethanol (1:1:1) solution exhibited a sheet resistance of $80 \Omega/\square$ and average transmittance of 73%, which did not meet the task outlined in chapter 1. A perovskite solar cell fabricated on the PEDOT:PSS electrode exhibited a low power conversion efficiency (PCE) of 5.3%, which was attributed to defects within the perovskite layer, high sheet resistance of PEDOT:PSS electrode, and low transmittance of the PEDOT:PSS electrodes compared to the ITO reference device of 12.3% PCE.

Silver nanowires electrodes met the task outlined in chapter 1 with sheet resistance less than $50 \Omega/\square$ and transmittance greater than 80%. UV-ozone treated electrodes lasted for two days longer than non-treated silver nanowire electrodes (average diameter of 80 nm) and was attributed to the UV-ozone creating a protective silver oxide layer. Silver nanowires with thicker average nanowire diameters (233 nm) lasted for 128 days and 263 days for UV-ozone treated and non-UV-ozone treated electrodes, respectively, which met the 6000 hour lifetime goal outlined in chapter 1. The thicker nanowires were more heat tolerant and failure was attributed to sulfur corrosion. The reduction in lifetime from UV-ozone treatment was attributed making these defect sites more reactive. This is the first report of silver nanowire electrodes observed to have self-healing property after allowed to rest due to failure from electrical stress. The self-healing in silver nanowire electrodes could be monumental for solar cell applications as the electrodes would be able to self-repair at night time.

5.2 CONCLUSIONS

PEDOT:PSS semitransparent electrodes did not meet the goals outlined in Chapter 1. Solvent blend additives and post treatments were not able to reduce the sheet resistance below $50 \Omega/\square$ while maintaining a transmittance greater than 80%. Silver nanowire electrodes, on the other hand, were able to meet this goal. The lifetime of non-UV-ozone treated silver nanowires electrodes with average nanowire diameter of 233 nm was able to exceed 6000 hour lifetime goal from chapter 1. Silver nanowire electrodes with thinner average nanowire diameter of 80 nm and UV-ozone treated silver nanowire electrodes (233 nm average diameter) did not meet the 6000 hour lifetime goal. Due to

time constraints, semi-transparent solar cell was not fabricated and the objective of this work is not complete.

5.3 FUTURE WORK

PEDOT:PSS semitransparent electrodes sheet resistance can be further reduced by adding silver nanoparticles (less than 50 nm in diameter) into the PEDOT:PSS film. The silver nanoparticles would create a plasmonic effect and absorb UV light. A polymer active layer tuned to absorb infrared light in conjunction with the silver nanoparticles would enable a device to take advantage of all non-visible light regions of the solar spectrum. Silver nanowires embedded in a polydimethylsiloxane (PDMS) matrix should be explored as a bottom flexible electrode. Polymer active layers that absorbed in the infrared regions decompose at temperatures greater than 100 °C, thus having silver nanowire bottom electrode would be advantageous due higher annealing temperatures for the silver nanowires and electron transport layer. ZnO and AZO electron transport layers typically require annealing temperatures of 200 °C or greater and a top PEDOT:PSS would not need annealed. However, both inverted and regular semitransparent solar cell structure using silver nanowire and PEDOT:PSS electrodes should be explored.

APPENDIX A

VISA resource name
GPIB0::25::INSTR

Error Query (False)

error in (no error)
status: code: d0
source:

Channel A

Measurement delay (ms): 3600000
Time conversion factor: 3600000
Channel A Start: **START**
Channel A Stop: **STOP**

Source Function (Current): Current
Source Level: 0.02
Limit (opposit of source): 10

error out channel A
status: source:
code: d0

Channel B

Measurement delay (ms) 2: 3600000
Time conversion factor 2: 3600000
Channel B start: **START**
Channel B Stop: **STOP**

Source Function (Current) 2: Current
Source Level 2: 0.02
Limit (opposit of source) 2: 10

error out channel B
status: source:
code: d0

Figure A.1. Front Panel display from lab view program used for lifetime measurements on silver nanowire electrodes, where Source Level 1 and 2 are set to 0.02 A and the maximum limit is 10 volts.

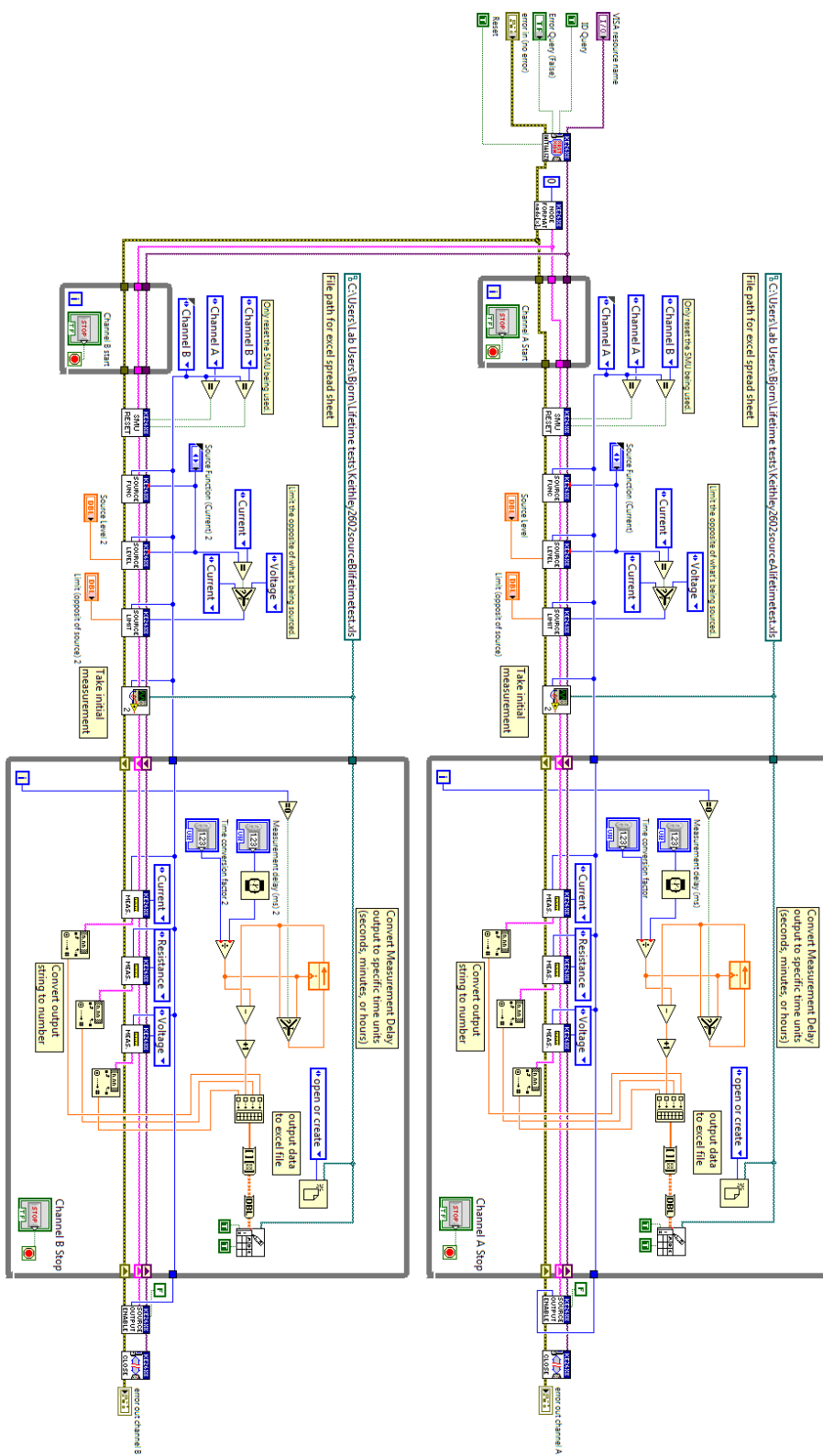


Figure A.2. Block diagram corresponding the Front Panel in Figure A.76.

APPENDIX B

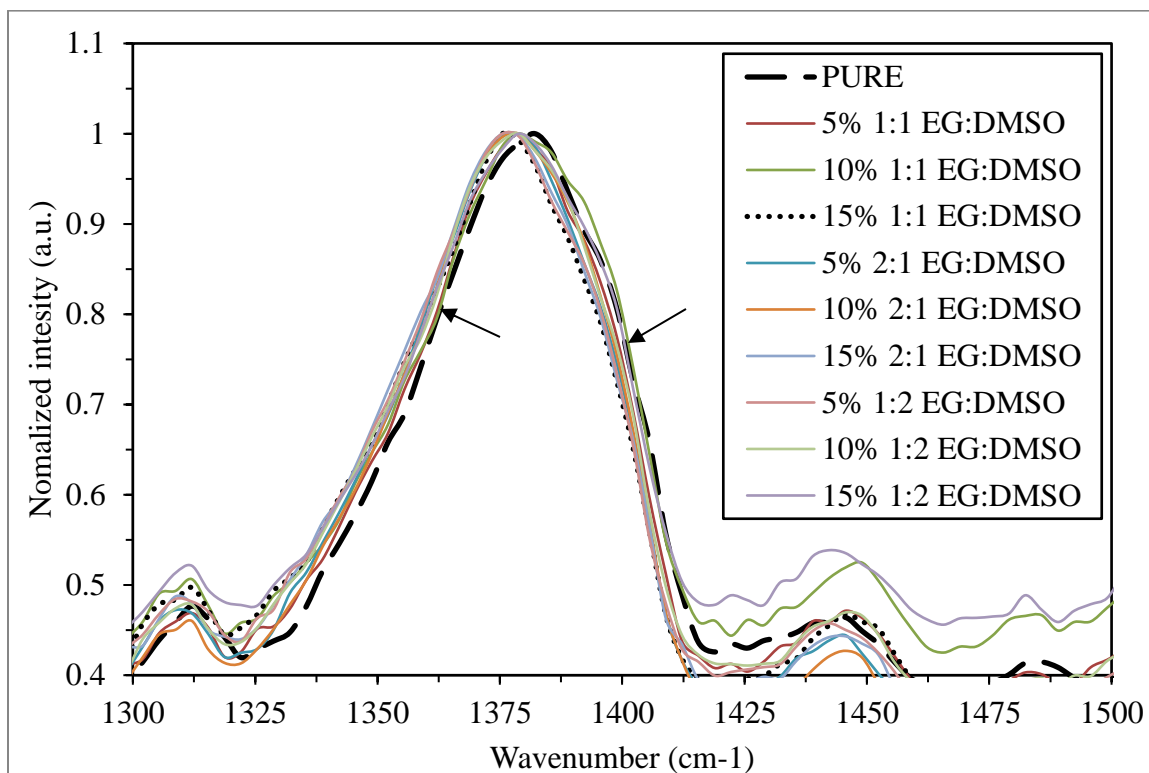


Figure B.1. Raman spectrum of PEDOT:PSS films with various % wt. of EG:DMSO 1:1, 1:2, and 2:1 v/v ratios

APPENDIX C

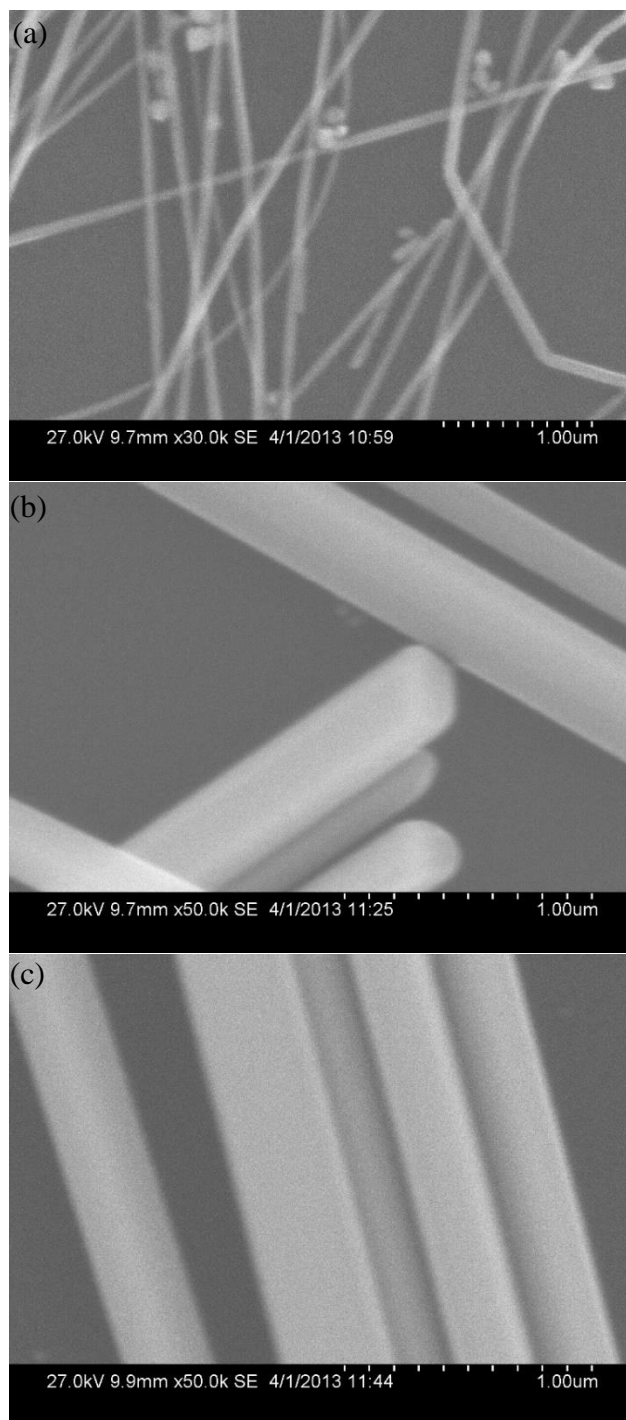


Figure C.1. Silver nanowires synthesized at 160 C after (a) 10, (b) 15, and (c) 20 minutes of reaction time with average nanowire diameter of 60 nm, 312 nm, and 350 nm, respectively.

REFERENCES

- [1] M. S. Alam, B. K. Bala, A. M. Z. Huq, and M. A. Matin, "A model for the quality of life as a function of electrical energy consumption," *Energy*, vol. 16, pp. 739-745, April 1, 1991.
- [2] M. S. Alam, A. Roychowdhury, K. K. Islam, and A. M. Z. Huq, "A revisited model for the physical quality of life (PQL) as a function of electrical energy consumption," *Energy*, vol. 23, pp. 791-801, Sept 1998.
- [3] R. A. Dias, C. R. Mattos, and J. A. P. Balestieri, "The limits of human development and the use of energy and natural resources," *Energy Policy*, vol. 34, pp. 1026-1031, June 2006.
- [4] S. Jahan, *2015 Human Development Report*. New York: United Nations Development Programme, 2015.
- [5] U. EIA, "International Energy Outlook 2013," *US Energy Information Administration (EIA)*, 2013.
- [6] B. Dudley, "BP statistical review of world energy. June 2012," *London, UK*, 2012.
- [7] B. Dudley, "BP Statistical Review of World Energy June 2015," *BP Statistical Review of World Energy*, 2015.
- [8] D. M. Rosenberg, P. McCully, and C. M. Pringle, "Global-scale environmental effects of hydrological alterations: introduction," *BioScience*, vol. 50, pp. 746-751, 2000.
- [9] M. I. Blanco, "The economics of wind energy," *Renewable and Sustainable Energy Reviews*, vol. 13, pp. 1372-1382, 2009.

- [10] P. Denholm and R. Sioshansi, "The value of compressed air energy storage with wind in transmission-constrained electric power systems," *Energy Policy*, vol. 37, pp. 3149-3158, Aug 2009.
- [11] F. Dincer, "The analysis on wind energy electricity generation status, potential and policies in the world," *Renewable and Sustainable Energy Reviews*, vol. 15, pp. 5135-5142, Dec 2011.
- [12] R. Saidur, N. A. Rahim, M. R. Islam, and K. H. Solangi, "Environmental impact of wind energy," *Renewable and Sustainable Energy Reviews*, vol. 15, pp. 2423-2430, June 2011.
- [13] J. M. Shuster, "Beyond Fossil Fools," *Edina, MN: Beaver Ponds Press, Inc*, 2008.
- [14] D. M. Fraser, A. Kouhestani, J. Parmentola, R. E. Prince, and R. S. Reynolds, *Commercial US Vendors Focus on Reducing the Cost of Fast Reactors*. International Atomic Energy Agency (IAEA): IAEA, 2015.
- [15] T. Lambert and X. H. Nghiem, "Review of the Deployment of and Research into Generation III & IV Nuclear Fission Reactors for Power Generation," *PAM Review: Energy Science & Technology*, vol. 1, pp. 90-108, 2015.
- [16] N. Iwai and K. Shishido, "The Impact of the Great East Japan Earthquake and Fukushima Daiichi Nuclear Accident on People's Perception of Disaster Risks and Attitudes Toward Nuclear Energy Policy," *Asian Journal for Public Opinion Research*, vol. 2, pp. 172-195, 2015.
- [17] N. Perrin, *Giving up the gun: Japan's reversion to the sword, 1543-1879*: David R. Godine Publisher, 1979.

- [18] Walmart. (May 1, 2016). *Walmart Builds on Leadership of Commercial Solar Deployment and Expands On-Site Solar Energy Projects* [web page]. Available: <http://corporate.walmart.com/news/news-archive/2014/11/20/walmart-builds-on-leadership-of-commercial-solar-deployment-and-expands-on-site-solar-energy-projects>
- [19] Apple. (May 1, 2016). *Climate Change* [web page]. Available: <http://www.apple.com/environment/climate-change/>
- [20] P. Eiffert and G. J. Kiss, *Building-integrated photovoltaic designs for commercial and institutional structures: a sourcebook for architects*: DIANE Publishing, 2000.
- [21] S. Kurtz, H. Atwater, A. Rockett, T. Buonassisi, C. Honsberg, and J. Benner, "Solar research not finished," *Nat Photon*, vol. 10, pp. 141-142, March 2016.
- [22] C. Tuchinda, S. Srivannaboon, and H. W. Lim, "Photoprotection by window glass, automobile glass, and sunglasses," *Journal of the American Academy of Dermatology*, vol. 54, pp. 845-854, 2006.
- [23] T. Miyazaki, A. Akisawa, and T. Kashiwagi, "Energy savings of office buildings by the use of semi-transparent solar cells for windows," *Renewable energy*, vol. 30, pp. 281-304, 2005.
- [24] NREL. (May 1, 2016). *Reference Solar Spectral Irradiance: ASTM G-173* [web page]. Available: <http://rredc.nrel.gov/solar/spectra/am1.5/ASTMG173/ASTMG173.html>

- [25] C. Denizot, S. Fay, J. Bailat, S. Jensen, A. Johansson, M. Lillemose, *et al.*, "Thin film silicon solar cells in a semi-transparent micro-structured metal substrate configuration," presented at the Proceeding of the 24th EU PVSEC, Hamburg, 2009.
- [26] A. Takeoka, S. Kouzuma, H. Tanaka, H. Inoue, K. Murata, M. Morizane, *et al.*, "Development and application of see-through a-Si solar cells," *Solar Energy Materials and Solar Cells*, vol. 29, pp. 243-252, April 1993.
- [27] R. Kuhn, A. Boueke, A. Kress, P. Fath, G. P. Willeke, and E. Bucher, "Characterization of novel mono- and bifacially active semi-transparent crystalline silicon solar cells," *Electron Devices, IEEE Transactions on*, vol. 46, pp. 2013-2017, 1999.
- [28] J. Yoon, A. J. Baca, S.-I. Park, P. Elvikis, J. B. Geddes, L. Li, *et al.*, "Ultrathin silicon solar microcells for semitransparent, mechanically flexible and microconcentrator module designs," *Nat Mater*, vol. 7, pp. 907-915, Nov 2008.
- [29] M. Biancardo, K. Taira, N. Kogo, H. Kikuchi, N. Kumagai, N. Kuratani, *et al.*, "Characterization of microspherical semi-transparent solar cells and modules," *Solar Energy*, vol. 81, pp. 711-716, June 2007.
- [30] C.-C. Chen, L. Dou, R. Zhu, C.-H. Chung, T.-B. Song, Y. B. Zheng, *et al.*, "Visibly Transparent Polymer Solar Cells Produced by Solution Processing," *ACS Nano*, vol. 6, pp. 7185-7190, Aug 28, 2012.
- [31] R. F. Bailey-Salzman, B. P. Rand, and S. R. Forrest, "Semitransparent organic photovoltaic cells," *Applied Physics Letters*, vol. 88, p. 233502, 2006.

- [32] K.-S. Chen, J.-F. Salinas, H.-L. Yip, L. Huo, J. Hou, and A. K. Y. Jen, "Semi-transparent polymer solar cells with 6% PCE, 25% average visible transmittance and a color rendering index close to 100 for power generating window applications," *Energy & Environmental Science*, vol. 5, pp. 9551-9557, 2012.
- [33] C. J. Mulligan, C. Bilen, X. Zhou, W. J. Belcher, and P. C. Dastoor, "Levelised cost of electricity for organic photovoltaics," *Solar Energy Materials and Solar Cells*, vol. 133, pp. 26-31, Feb 2015.
- [34] C. J. M. E. Brian Azzopardi, Antonio Urbina, Frederik C. Krebs, Joseph Mutalea and Jenny Nelson, "Economic assessment of solar electricity production from organic-based photovoltaic modules in a domestic environment," *Energy Environmental Science*, vol. 4, pp. 3741-3753, May 18, 2011.
- [35] D. M. Chapin, C. S. Fuller, and G. L. Pearson, "A New Silicon p-n Junction Photocell for Converting Solar Radiation into Electrical Power," *Journal of Applied Physics*, vol. 25, pp. 676-677, 1954.
- [36] J. Lindmayer and J. Allison, "The violet cell: an improved silicon solar cell," *Solar cells*, vol. 29, pp. 151-166, 1990.
- [37] A. Blakers and M. Green, "20% efficiency silicon solar cells," *Applied physics letters*, vol. 48, pp. 215-217, 1986.
- [38] J. Zhao, A. Wang, P. P. Altermatt, S. R. Wenham, and M. A. Green, "24% efficient per silicon solar cell: recent improvements in high efficiency silicon cell research," *Solar energy materials and solar cells*, vol. 41, pp. 87-99, 1996.

- [39] J. Zhao, A. Wang, and M. A. Green, "24.5% Efficiency silicon PERT cells on MCZ substrates and 24.7% efficiency PERL cells on FZ substrates," *Progress in Photovoltaics: Research and Applications*, vol. 7, pp. 471-474, 1999.
- [40] M. A. Green, K. Emery, Y. Hishikawa, W. Warta, and E. D. Dunlop, "Solar cell efficiency tables (Version 45)," *Progress in Photovoltaics: Research and Applications*, vol. 23, pp. 1-9, 2015.
- [41] D. E. Carlson and C. R. Wronski, "Amorphous silicon solar cell," *Applied Physics Letters*, vol. 28, pp. 671-673, 1976.
- [42] P. Torres, J. Meier, R. Flückiger, U. Kroll, J. A. Selvan, H. Keppner, *et al.*, "Device grade microcrystalline silicon owing to reduced oxygen contamination," *Applied Physics Letters*, vol. 69, pp. 1373-1375, 1996.
- [43] M. J. Keevers, T. L. Young, U. Schubert, and M. A. Green, "10% efficient CSG minimodules," in *22nd European Photovoltaic Solar Energy Conference*, 2007, pp. 1783-1790.
- [44] M. Singh, J. Jiu, T. Sugahara, and K. Suganuma, "Thin-Film Copper Indium Gallium Selenide Solar Cell Based on Low-Temperature All-Printing Process," *ACS Applied Materials & Interfaces*, vol. 6, pp. 16297-16303, Sept 24, 2014.
- [45] M. Pagliaro, R. Ciriminna, and G. Palmisano, "Flexible Solar Cells," *ChemSusChem*, vol. 1, pp. 880-891, 2008.
- [46] D. Kearns and M. Calvin, "Photovoltaic Effect and Photoconductivity in Laminated Organic Systems," *The Journal of Chemical Physics*, vol. 29, pp. 950-951, 1958.

- [47] D. Morel, A. Ghosh, T. Feng, E. Stogryn, P. Purwin, R. Shaw, *et al.*, "High-efficiency organic solar cells," *Applied Physics Letters*, vol. 32, pp. 495-497, 1978.
- [48] C. W. Tang, "Two-layer organic photovoltaic cell," *Applied Physics Letters*, vol. 48, pp. 183-185, 1986.
- [49] N. S. Sariciftci, L. Smilowitz, A. J. Heeger, and F. Wudl, "Photoinduced Electron Transfer from a Conducting Polymer to Buckminsterfullerene," *Science*, vol. 258, pp. 1474-1476, Nov 27, 1992.
- [50] G. Yu, J. Gao, J. C. Hummelen, F. Wudl, and A. J. Heeger, "Polymer Photovoltaic Cells: Enhanced Efficiencies via a Network of Internal Donor-Acceptor Heterojunctions," *Science*, vol. 270, pp. 1789-1791, December 15, 1995.
- [51] G. Li, V. Shrotriya, J. Huang, Y. Yao, T. Moriarty, K. Emery, *et al.*, "High-efficiency solution processable polymer photovoltaic cells by self-organization of polymer blends," *Nat Mater*, vol. 4, pp. 864-868, Nov 2005.
- [52] W. Zhao, D. Qian, S. Zhang, S. Li, O. Inganäs, F. Gao, *et al.*, "Fullerene-Free Polymer Solar Cells with over 11% Efficiency and Excellent Thermal Stability," *Advanced Materials*, 2016.
- [53] A. Kojima, K. Teshima, Y. Shirai, and T. Miyasaka, "Organometal Halide Perovskites as Visible-Light Sensitizers for Photovoltaic Cells," *Journal of the American Chemical Society*, vol. 131, pp. 6050-6051, May 6, 2009.

- [54] J. Burschka, N. Pellet, S.-J. Moon, R. Humphry-Baker, P. Gao, M. K. Nazeeruddin, *et al.*, "Sequential deposition as a route to high-performance perovskite-sensitized solar cells," *Nature*, vol. 499, pp. 316-319, July 18, 2013.
- [55] W. Nie, H. Tsai, R. Asadpour, J.-C. Blancon, A. J. Neukirch, G. Gupta, *et al.*, "High-efficiency solution-processed perovskite solar cells with millimeter-scale grains," *Science*, vol. 347, pp. 522-525, Jan 30, 2015.
- [56] W. S. Yang, J. H. Noh, N. J. Jeon, Y. C. Kim, S. Ryu, J. Seo, *et al.*, "High-performance photovoltaic perovskite layers fabricated through intramolecular exchange," *Science*, May 21, 2015.
- [57] NREL. (2016, June 22). *Best Research-Cell Efficiencies* [web page]. Available: http://www.nrel.gov/ncpv/images/efficiency_chart.jpg
- [58] A. Mei, X. Li, L. Liu, Z. Ku, T. Liu, Y. Rong, *et al.*, "A hole-conductor-free, fully printable mesoscopic perovskite solar cell with high stability," *Science*, vol. 345, pp. 295-298, July 18, 2014.
- [59] F. Hao, C. C. Stoumpos, D. H. Cao, R. P. H. Chang, and M. G. Kanatzidis, "Lead-free solid-state organic-inorganic halide perovskite solar cells," *Nat Photon*, vol. 8, pp. 489-494, June 2014.
- [60] M. Ohnishi, H. Shibuya, N. Okuda, H. Inoue, Y. Kishi, S. Kiyama, *et al.*, "New type structure of a-Si solar cell submodules fabricated by microscopic hole spacing technique," in *Photovoltaic Specialists Conference, 1990., Conference Record of the Twenty First IEEE*, 1990, pp. 1394-1399.
- [61] J. Y. Lee, S. T. Connor, Y. Cui, and P. Peumans, "Solution-processed metal nanowire mesh transparent electrodes," *Nano Lett*, vol. 8, pp. 689-92, Feb 2008.

- [62] P. Newswire. (2016, August 17). *Clevios(TM) PH1000 Material Breaks Conductivity Record* [web page]. Available: <http://www.prnewswire.com/news-releases/cleviostm-ph1000-material-breaks-conductivity-record-61890872.html>
- [63] Y. H. Kim, C. Sachse, M. L. Machala, C. May, L. Müller-Meskamp, and K. Leo, "Highly Conductive PEDOT:PSS Electrode with Optimized Solvent and Thermal Post-Treatment for ITO-Free Organic Solar Cells," *Advanced Functional Materials*, vol. 21, pp. 1076-1081, 2011.
- [64] L. B. Hu, H. S. Kim, J. Y. Lee, P. Peumans, and Y. Cui, "Scalable Coating and Properties of Transparent, Flexible, Silver Nanowire Electrodes," *Acs Nano*, vol. 4, pp. 2955-2963, May 2010.
- [65] Y. Xia and J. Ouyang, "PEDOT:PSS films with significantly enhanced conductivities induced by preferential solvation with cosolvents and their application in polymer photovoltaic cells," *Journal of Materials Chemistry*, vol. 21, pp. 4927-4936, 2011.
- [66] R. R. Lunt and V. Bulovic, "Transparent, near-infrared organic photovoltaic solar cells for window and energy-scavenging applications," *Applied Physics Letters*, vol. 98, p. 113305, 2011.
- [67] D.-S. Leem, A. Edwards, M. Faist, J. Nelson, D. D. C. Bradley, and J. C. de Mello, "Efficient Organic Solar Cells with Solution-Processed Silver Nanowire Electrodes," *Advanced Materials*, vol. 23, pp. 4371-4375, 2011.
- [68] W. Gaynor, G. F. Burkhard, M. D. McGehee, and P. Peumans, "Smooth Nanowire/Polymer Composite Transparent Electrodes," *Advanced Materials*, vol. 23, pp. 2905-2910, Jul 12, 2011.

- [69] T. Stubhan, J. Krantz, N. Li, F. Guo, I. Litzov, M. Steidl, *et al.*, "High fill factor polymer solar cells comprising a transparent, low temperature solution processed doped metal oxide/metal nanowire composite electrode," *Solar Energy Materials and Solar Cells*, vol. 107, pp. 248-251, Dec 2012.
- [70] D. Alemu, H.-Y. Wei, K.-C. Ho, and C.-W. Chu, "Highly conductive PEDOT:PSS electrode by simple film treatment with methanol for ITO-free polymer solar cells," *Energy & Environmental Science*, vol. 5, pp. 9662-9671, 2012.
- [71] M. Reinhard, R. Eckstein, A. Slobodskyy, U. Lemmer, and A. Colsmann, "Solution-processed polymer-silver nanowire top electrodes for inverted semi-transparent solar cells," *Organic Electronics*, vol. 14, pp. 273-277, Jan 2013.
- [72] F. Guo, X. Zhu, K. Forberich, J. Krantz, T. Stubhan, M. Salinas, *et al.*, "ITO-Free and Fully Solution-Processed Semitransparent Organic Solar Cells with High Fill Factors," *Advanced Energy Materials*, vol. 3, pp. 1062-1067, 2013.
- [73] H. H. Khaligh and I. A. Goldthorpe, "Failure of silver nanowire transparent electrodes under current flow," *Nanoscale Res Lett*, vol. 8, p. 235, 2013.
- [74] N. Kim, S. Kee, S. H. Lee, B. H. Lee, Y. H. Kahng, Y. R. Jo, *et al.*, "Highly Conductive PEDOT: PSS Nanofibrils Induced by Solution-Processed Crystallization," *Advanced Materials*, vol. 26, pp. 2268-2272, Apr 2014.
- [75] F. Guo, H. Azimi, Y. Hou, T. Przybilla, M. Hu, C. Bronnbauer, *et al.*, "High-performance semitransparent perovskite solar cells with solution-processed silver nanowires as top electrodes," *Nanoscale*, vol. 7, pp. 1642-1649, 2015.

- [76] P. Adhikary, S. Venkatesan, P. P. Maharjan, D. Galipeau, and Q. Qiao, "Enhanced Performance of PDPP3T/PC[60]BM Solar Cells Using High Boiling Solvent and UV - Ozone Treatment," *IEEE Transactions on Electron Devices*, vol. 60, pp. 1763-1768, 2013.
- [77] R. E. Hummel, *Electronic properties of materials*: Springer Science & Business Media, 2011.
- [78] L. Etgar, P. Gao, Z. Xue, Q. Peng, A. K. Chandiran, B. Liu, *et al.*, "Mesoscopic CH₃NH₃PbI₃/TiO₂ Heterojunction Solar Cells," *Journal of the American Chemical Society*, vol. 134, pp. 17396-17399, Oct 24, 2012.
- [79] G. Xing, N. Mathews, S. Sun, S. S. Lim, Y. M. Lam, M. Grätzel, *et al.*, "Long-Range Balanced Electron- and Hole-Transport Lengths in Organic-Inorganic CH₃NH₃PbI₃," *Science*, vol. 342, pp. 344-347, Oct 18, 2013.
- [80] S. D. Stranks, G. E. Eperon, G. Grancini, C. Menelaou, M. J. P. Alcocer, T. Leijtens, *et al.*, "Electron-Hole Diffusion Lengths Exceeding 1 Micrometer in an Organometal Trihalide Perovskite Absorber," *Science*, vol. 342, pp. 341-344, Oct 18, 2013.
- [81] R. Kuhn, A. Boueke, A. Kress, P. Fath, G. P. Willeke, and E. Bucher, "Characterization of novel mono- and bifacially active semi-transparent crystalline silicon solar cells," *IEEE Transactions on Electron Devices*, vol. 46, pp. 2013-2017, 1999.

- [82] S. K. M. Jönsson, J. Birgersson, X. Crispin, G. Greczynski, W. Osikowicz, A. W. Denier van der Gon, *et al.*, "The effects of solvents on the morphology and sheet resistance in poly(3,4-ethylenedioxythiophene)–polystyrenesulfonic acid (PEDOT–PSS) films," *Synthetic Metals*, vol. 139, pp. 1-10, Aug 8, 2003.
- [83] J. Ouyang, Q. Xu, C.-W. Chu, Y. Yang, G. Li, and J. Shinar, "On the mechanism of conductivity enhancement in poly(3,4-ethylenedioxythiophene):poly(styrene sulfonate) film through solvent treatment," *Polymer*, vol. 45, pp. 8443-8450, Nov 2004.
- [84] L. Groenendaal, F. Jonas, D. Freitag, H. Pielartzik, and J. R. Reynolds, "Poly(3,4-ethylenedioxythiophene) and Its Derivatives: Past, Present, and Future," *Advanced Materials*, vol. 12, pp. 481-494, 2000.
- [85] A. Elschner, S. Kirchmeyer, W. Lovenich, U. Merker, and K. Reuter, *PEDOT: principles and applications of an intrinsically conductive polymer*: CRC Press, 2010.
- [86] A. M. Nardes, *On the conductivity of PEDOT:PSS thin films*: Technische Universiteit Eindhoven, 2007.
- [87] T. Stöcker, A. Köhler, and R. Moos, "Why does the electrical conductivity in PEDOT:PSS decrease with PSS content? A study combining thermoelectric measurements with impedance spectroscopy," *Journal of Polymer Science Part B: Polymer Physics*, vol. 50, pp. 976-983, 2012.
- [88] J. Ouyang, "Solution-Processed PEDOT:PSS Films with Conductivities as Indium Tin Oxide through a Treatment with Mild and Weak Organic Acids," *ACS Applied Materials & Interfaces*, vol. 5, pp. 13082-13088, Dec 26, 2013.

- [89] Y. Xia, K. Sun, and J. Ouyang, "Solution-Processed Metallic Conducting Polymer Films as Transparent Electrode of Optoelectronic Devices," *Advanced Materials*, vol. 24, pp. 2436-2440, 2012.
- [90] M. Fabretto, C. Hall, T. Vaithianathan, P. C. Innis, J. Mazurkiewicz, G. G. Wallace, *et al.*, "The mechanism of conductivity enhancement in poly(3,4-ethylenedioxythiophene)-poly(styrenesulfonic) acid using linear-diol additives: Its effect on electrochromic performance," *Thin Solid Films*, vol. 516, pp. 7828-7835, Sept 1, 2008.
- [91] I. Cruz-Cruz, M. Reyes-Reyes, M. A. Aguilar-Frutis, A. G. Rodriguez, and R. López-Sandoval, "Study of the effect of DMSO concentration on the thickness of the PSS insulating barrier in PEDOT:PSS thin films," *Synthetic Metals*, vol. 160, pp. 1501-1506, July 2010.
- [92] J. Y. Kim, J. H. Jung, D. E. Lee, and J. Joo, "Enhancement of electrical conductivity of poly(3,4-ethylenedioxythiophene)/poly(4-styrenesulfonate) by a change of solvents," *Synthetic Metals*, vol. 126, pp. 311-316, Feb 14, 2002.
- [93] J. L. Elechiguerra, L. Larios-Lopez, C. Liu, D. Garcia-Gutierrez, A. Camacho-Bragado, and M. J. Yacaman, "Corrosion at the Nanoscale: The Case of Silver Nanowires and Nanoparticles," *Chemistry of Materials*, vol. 17, pp. 6042-6052, Nov 1, 2005.
- [94] T.-B. Song, Y. Chen, C.-H. Chung, Y. Yang, B. Bob, H.-S. Duan, *et al.*, "Nanoscale Joule Heating and Electromigration Enhanced Ripening of Silver Nanowire Contacts," *ACS Nano*, vol. 8, pp. 2804-2811, March 23, 2014.

- [95] C. Mayousse, C. Celle, A. Fraczkiewicz, and J.-P. Simonato, "Stability of silver nanowire based electrodes under environmental and electrical stresses," *Nanoscale*, vol. 7, pp. 2107-2115, 2015.
- [96] T.-B. Song, Y. S. Rim, F. Liu, B. Bob, S. Ye, Y.-T. Hsieh, *et al.*, "Highly Robust Silver Nanowire Network for Transparent Electrode," *ACS Applied Materials & Interfaces*, vol. 7, pp. 24601-24607, Nov 11, 2015.
- [97] A. Kim, Y. Won, K. Woo, C. H. Kim, and J. Moon, "Highly Transparent Low Resistance ZnO/Ag Nanowire/ZnO Composite Electrode for Thin Film Solar Cells," *Acs Nano*, vol. 7, pp. 1081-1091, Feb 2013.
- [98] S. Vunnam, "Drop-based Direct Write Techniques for Making Transparent Conducting Oxide Films," South Dakota School of Mines and Technology, Rapid City, 2014.
- [99] D. Petri, "Characterization of spin-coated polymer films," *Journal of the Brazilian Chemical Society*, vol. 13, pp. 695-699, 2002.
- [100] F. S. F. Morgenstern, D. Kabra, S. Massip, T. J. K. Brenner, P. E. Lyons, J. N. Coleman, *et al.*, "Ag-nanowire films coated with ZnO nanoparticles as a transparent electrode for solar cells," *Applied Physics Letters*, vol. 99, p. 183307, 2011.
- [101] C.-H. Chung, T.-B. Song, B. Bob, R. Zhu, and Y. Yang, "Solution-processed flexible transparent conductors composed of silver nanowire networks embedded in indium tin oxide nanoparticle matrices," *Nano Research*, vol. 5, pp. 805-814, 2012.

- [102] B. Worfolk, S. Andrews, S. Park, J. Reinspach, N. Liu, M. Toney, *et al.*, "Ultrahigh electrical conductivity in solution-sheared polymeric transparent films," *Proceedings of the National Academy of Sciences of the United States of America*, vol. 112, pp. 14138-14143, 2015.
- [103] Y. Xia, K. Sun, and J. Ouyang, "Highly conductive poly(3,4-ethylenedioxythiophene):poly(styrene sulfonate) films treated with an amphiphilic fluoro compound as the transparent electrode of polymer solar cells," *Energy & Environmental Science*, vol. 5, pp. 5325-5332, 2012.
- [104] J. Goldstein, *Practical scanning electron microscopy: electron and ion microprobe analysis*: Springer Science & Business Media, 2012.
- [105] M. Liu, M. B. Johnston, and H. J. Snaith, "Efficient planar heterojunction perovskite solar cells by vapour deposition," *Nature*, vol. 501, pp. 395-398, Sept 19, 2013.
- [106] S. Garreau, G. Louarn, J. P. Buisson, G. Froyer, and S. Lefrant, "In Situ Spectroelectrochemical Raman Studies of Poly(3,4-ethylenedioxythiophene) (PEDT)," *Macromolecules*, vol. 32, pp. 6807-6812, Oct 1, 1999.
- [107] I. M. Braun, "Operating Instructions - Supplement A," Revision 002 ed, 2007.
- [108] Hitachi-High-Tech-Science-Systems-Corporation, "Instruction Manual For Model S-3400N Scanning Electron Microscope ", 2006.

- [109] Cannon. (2016, July 24). *EOS Digital Rebel XTi EOS 400D digital*. Available:
http://www.cte.uw.edu/w/images/7/7e/Canon_Rebel_XTi.pdf
- [110] Keysight-Technologies. (2011, June 24). *Technical Support* [web page].
Available:
[http://www.keysight.com/main/facet.jsp?c=186092.i.1&to=80029.k.0&cc=US&l
c=eng](http://www.keysight.com/main/facet.jsp?c=186092.i.1&to=80029.k.0&cc=US&l
c=eng)
- [111] D. K. Nečas, Petr. (2016, June 24). *Gwyddion* [web page]. Available:
<http://gwyddion.net/>
- [112] Agilent-Technologies-Inc., "Agilent chemStation Security Pack for UV-visible Spectroscopy," 04/07 ed. U.S.A, 2007.
- [113] Horiba, "LabRAM HR Software and Hardware User Guid."
- [114] A. Dubey and Q. Qiquan, "RIGAKU SMARTLAB Operations Guide," 2014.
- [115] IXRF-Systems-Inc., "EDS 2004 Version 1.3 Software User's Guide," 2004.
- [116] A. Fowler, R. Micham, J. Sternhagen, and D. Galipeau, "Plasma Sciences System," in *Microelectronic Device Fabrication Laboratory Manual*, 7 ed. Brookings: Department of Electrical Engineering South Dakota State University, 2010, pp. 25-27.
- [117] S. Zhang, P. Kumar, A. S. Nouas, L. Fontaine, H. Tang, and F. Cicoira, "Solvent-induced changes in PEDOT:PSS films for organic electrochemical transistors," *APL Mater.*, vol. 3, p. 014911, 2015.

- [118] Z. Hu, J. Zhang, Z. Hao, and Y. Zhao, "Influence of doped PEDOT:PSS on the performance of polymer solar cells," *Solar Energy Materials and Solar Cells*, vol. 95, pp. 2763-2767, Oct 2011.
- [119] O. Dimitriev, D. Grinko, Y. V. Noskov, N. Ogurtsov, and A. Pud, "PEDOT: PSS films—Effect of organic solvent additives and annealing on the film conductivity," *Synthetic Metals*, vol. 159, pp. 2237-2239, 2009.
- [120] T. Takano, H. Masunaga, A. Fujiwara, H. Okuzaki, and T. Sasaki, "PEDOT Nanocrystal in Highly Conductive PEDOT:PSS Polymer Films," *Macromolecules*, vol. 45, pp. 3859-3865, May 8, 2012.
- [121] S. Garreau, J. L. Duvail, and G. Louarn, "Spectroelectrochemical studies of poly(3,4-ethylenedioxythiophene) in aqueous medium," *Synthetic Metals*, vol. 125, pp. 325-329, Dec 20, 2001.
- [122] S. R. Cowan, A. Roy, and A. J. Heeger, "Recombination in polymer-fullerene bulk heterojunction solar cells," *Physical Review B*, vol. 82, p. 245207, Dec 16, 2010.
- [123] M. Hu, J. Gao, Y. Dong, S. Yang, and R. K. Y. Li, "Rapid controllable high-concentration synthesis and mutual attachment of silver nanowires," *RSC Advances*, vol. 2, pp. 2055-2060, 2012.
- [124] S. Karim, M. E. Toimil-Molares, W. Ensinger, A. G. Balogh, T. W. Cornelius, E. U. Khan, *et al.*, "Influence of crystallinity on the Rayleigh instability of gold nanowires," *Journal of Physics D: Applied Physics*, vol. 40, p. 3767, 2007.
- [125] J. Novakovic, P. Vassiliou, and E. Georgiza, "Electrochemical cleaning of artificially tarnished silver," *Int J Electrochem Sci*, vol. 8, pp. 7223-7232, 2013.

- [126] Z. Cheng, L. Liu, S. Xu, M. Lu, and X. Wang, "Temperature Dependence of Electrical and Thermal Conduction in Single Silver Nanowire," *Scientific Reports*, vol. 5, p. 10718, June 2, 2015.